CLARKSON UNIVERSITY

Methods of Identification of Structural Damage

A Dissertation

By

Amila Sudu Ambegedara

Department of Mathematics

Submitted in partial fulfillment of the requirements

for the degree of

Doctor of Philosophy, Mathematics

August 2019

Accepted by the Graduate School

—————, ——————————————

Date,   Dean

Abstract

Early detection of structural damage is of special attention for civil and mechanical engineers. Construction designs of structural systems, such as turbines, bridges, aircraft, have become more complicated. Evaluating the load bearing capacity of such a complex structure can be performed using mechanical modeling methods [1]. However, the characterization of cracks or structural damage is a crucial task. Concurrently, assessment of anomalies soft soil/voids at geotechnical sites is important in the design, construction, and maintenance of all civil infrastructure system, as anomalies are the most significant cause of problems at the sites. Thus the development of non-destructive techniques has received increasing attention in recent years. The goal of this thesis is to develop noninvasive damage detection techniques for identifying and localizing damage in complex structures by minimizing the computational requirements. Two approaches are proposed for such a purpose.

In the first part of the thesis, an approach that uses information theoretical methods is introduced to study noninvasive damage detection techniques for structures, such as bridges. We introduce noninvasive damage detection methods for data acquired from spatially distributed sensors of accelerometry time series collected from a recent experiment on a local bridge in New York State. Several findings are in order. The time series data, measured accelerations across sensors, roughly follows a Laplace distribution, allowing us to develop parametric estimators for various information-theoretic measures such as entropy and mutual information, between the sensor sites. As damage is progressively introduced by the removal of structural bolts, of the first diaphragm connection, the interaction between spatially nearby sensors as measured by mutual information becomes weaker, confirming that the bridge is "loosened," and thereby suggesting a method that may be used in live field studies. Using a proposed optimal mutual information interaction procedure to prune away indirect interactions, we found that the primary direction of interaction or influence aligns

ii

with the traffic direction on the bridge even after damaging the bridge.

In the second part of the thesis, inverse problems for partial differential equations are introduced for the purpose of studying sinkholes developing in the Earth. Structural damage, or collapse, that can be caused by low-velocity anomalies such as soft soil, or voids, in subsurface structures can be identified by a full wave inversion of the 2-D elastic wave propagation. A full seismic waveform inversion method using the Gauss-Newton method is presented for the detection of embedded sinkholes. A technique, which we call "different cell size" is proposed to address the computational and memory requirements of the Gauss-Newton algorithm. To this end, a local time-space mesh refinement method for simulations of elastic propagation in media with small scale heterogeneities is adapted to solve the partial differential equations which model propagation of energetic waveforms introduced into the soil. Cubic smooth spline interpolation is used for the spatial mesh refinement step. We present the solution of the 2-D elastic wave equations using the local time-space grid refinement method, with further advancements for the full 3-D simulation in progress.

Acknowledgments

First and foremost, I would like to express my sincere gratitude to my advisor, Prof. Erik Bollt for the continuous support of my PhD study and research, for his patience, motivation and immense knowledge. His guidance helped me in all the time of research and writing of this thesis. I could not have imagined having a better advisor for my PhD. I appreciate the financial support received as a research assistantship from his info fragility grant.

I would like to thank my co-advisor Prof. Jie Sun. I extremely grateful for his advice, encouragement and support of the research. A special thank goes to Dr. Khiem Tran, University of Florida for his guidance and suggestions throughout the Full Wave Inversion project. I appreciate the financial support received as a research assistantship from his NSF grant. I would like to thank Prof. Kerop Janoyan for providing me experimental data for my research.

My special gratitude goes to the Department of Mathematics at Clarkson University for providing me a teaching assistantship.

I would like to thank the rest of my committee, Prof. Marko Budusic and Prof. Guanming Yao for their insightful comments and encouragements.
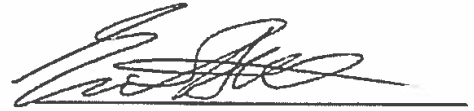
Special thank goes to Jeremy and Warren for reading my thesis and providing me valuable comments and suggestions. I appreciate the support from my lab mates, Sula, Abd, and Sudam.

I would also like to thank to my family. Words cannot express how grateful I am to my son Nithish, my mother, my father, my mother-in-law, my father-in-law, and my brothers for all the sacrifices that you all have made on my behalf. I would not have made it this far without them.

I truly thank my wife, Indika for everything she has done for me, sticking by my side, even when I was irritable and depressed. Indika's support and encouragement made me succeed in my graduate studies.

The undersigned have examined the thesis/dissertation entitled "Methods of Identification of Structural Damage" presented by Amila Sudu Ambegedara, a candidate for the degree of Doctor of Philosophy (Mathematics), and hereby certify that it is worthy of acceptance.

7/18/19
Date

Prof. Erik Bollt (Advisor)

Prof. Jie Sun (Co-advisor)

Prof. Kerop Janoyan

Prof. Marko Budisic

Guangming Yao

Prof. Guagming Yao

v

Contents

List of Tables

List of Figures

xiii

xiv

xvi

Chapter 1

Introduction

Engineered systems degrade, decline, corrode or are otherwise damaged naturally in time [26]. In some cases, damages can be detected from visual inspection. However, in most of the cases, the damage is not visible.

A few examples of such damages are shown in Fig 1.1, Fig 1.2, and Fig 1.3.

(a)   (b)
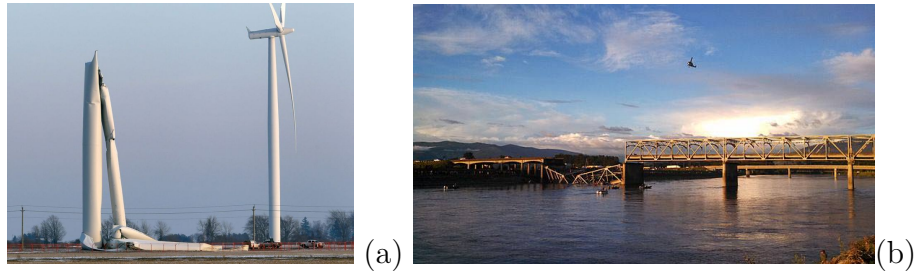
Figure 1.1: (a) A damaged wind turbine (photo credit: Ref. [2])(b) a collapsed bridge (photo credit: Ref.[3]).

Figure 1.1(a) shows an industrial wind turbine buckled over in South Chatham-Kent, Ontario. The whole tower failed due to a civil engineering problem. Figure 1.1(b) shows the collapse of the I-5 Skagit River Bridge, which failed in 2013. The bridge collapsed after passing an oversized load truck. The engineers found that the failure was due to infrastructure-related problems.

(a)

(b)

Figure 1.2: Two sinkholes in Chicago and Hudson (photo credit: Ref. [4, 5]).

Figure 1.2(a) shows a sinkhole that opened up in a street in Chicago's South Side. This is a 20-40 foot-wide sinkhole, which was large enough to engulf three cars and send one driver to the hospital. A sinkhole that happened in 2012 at Shoal drive, Hudson is shown in Fig 1.2(b). This 40 foot wide and 20 foot deep sinkhole swallowed the back of a home.

The failure of the Tacoma Narrows bridge that was built to cross the Puget Sound in Washington state in 1940 is another example of invisible damage. Four months after opening to the public, it collapsed into the water as a result of aeroelastic flutter caused by a 42 mph (68 km/h) wind. Figure 1.3(a) and (b) show the Tacoma Narrows Bridge before and after the damage. The best way to avoid such failures is to identify or predict such damage ahead of time in order to protect the public from injuries, loss of life, and property damage. Thus the study of nondestructive damage detection methods plays an important role in science and engineering fields [27–30].
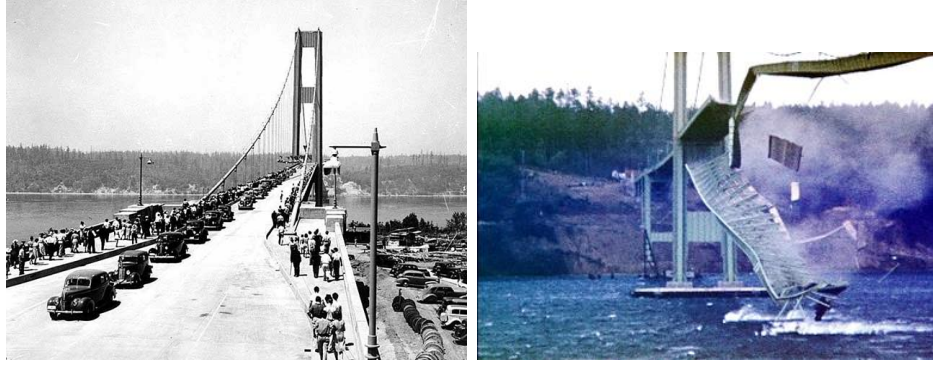
Figure 1.3: The failure of the Tacoma-Narrows Bridge (photo credit: Ref. [3]).

In the literature, several nondestructive methods such as vibration-based methods, ultrasonic methods, and frequency-based methods have been developed to monitor the structural damages of systems using various experimental and theoretical techniques [6, 26, 29, 31–35] (More details of these methods are presented in Chapter 2). Some methods, such as vibration-based damage detection methods, are found to be promising in locating and quantifying the damage [7, 26]. However, some limitations of these methods are reported [7, 26]. One of the drawbacks is the effectiveness of the methods. The complexity of civil structures reduces the efficacy of these methods. In addition, the results of these methods are associated with measurement errors, processing errors, and high computational costs.

The goal of this thesis is to develop damage detection techniques for identifying and localizing damages in complex structures by considering computational efficiency. This thesis basically presents two approaches. The first approach uses the information theoretical measures based techniques for damage detection in complex dynamical systems.

For initial analysis, one can use mutual information (MI), which is an information measure that can be used to identify the causal effect of a network system. The dynamical properties of two status of structures (e.g., a baseline structure and a damaged structure) are different, thus the MI also differs in the two status of structures.

Therefore, MI flow difference of structures can be successfully used to identify damage and location.

The information flow of a structure or system between sensors can be described using networks. Thus a directed graph is used to model processes and relations in information systems. A network graph $G = (V, E)$ consists of a set of nodes $V = \{1, 2, ..., n\}$ and a set of edges E, where $E \subset V \times V$. The adjacency matrix can be used for data processing. The adjacency matrix $A = [A_{ij}]_{n \times n}$ corresponding to the weighted network is

$$A_{ij} = \begin{cases} \text{weight of the link } j \to i & \text{if } j \to i \text{ in the network} \\ 0 & \text{otherwise} \end{cases}$$

and the corresponding unweighted adjacency matrix $\chi(A)$ is

$$\chi(A)_{ij} = \begin{cases} 1 & \text{iff } A_{ij} \neq 0 \\ 0 & \text{iff } A_{ij} = 0 \end{cases}$$

In network theory, the sensors represent nodes and the edges represent the connection between nodes. One of the biggest challenges here is to identify the connections or edges. Thus, we develop MI-based mathematical techniques that can be applied to complex structures.

The second approach is based on full wave inversion for sinkhole detection in subsurfaces. There are many nondestructive testing methods available for health monitoring in subsurfaces. Gravity methods [18, 36, 37], electric resistivity methods [38, 39], and seismic methods are some exciting new methods in locating sinkholes (more details of these methods are presented in Chapter 5). However, the full-waveform inversion (FWI) approach [40, 41] is another approach that offers the potential to produce higher resolution imaging of the subsurface by extracting infor-

mation contained in the complete waveforms [42]. This approach seeks to minimize residuals between the model responses obtained by forward simulation of wave equations and observed seismic data.

The forward simulation of an FWI technique consists of generating synthetic wave fields by solving wave equations. One of the goals here is to develop a numerical scheme to solve 2D/3D wave equations with small-scale heterogeneities. FWI technique uses a model updating scheme to invert full seismic wave-fields. Recently, an FWI technique based on the Gauss-Newton inversion method is developed in Ref. [21]. One of the drawbacks of the Gauss-Newton method is a large memory requirement to store the Jacobian matrix. Our goal here is to improve the computational efficiency and the memory requirements of the developed technique in Ref. [21].

1.1 Organization

This thesis is arranged in the following way. Chapter 2 presents a literature review on existing nondestructive damage identification methods. These methods are described with mathematical details and examples. The advantages and limitations of the existing methods are also presented in Chapter 2.

Some basic concepts, definitions, and important theorems of information theory are presented in Chapter 3. This chapter first starts with an introduction to causality and information theory. The basic concepts, such as entropy and mutual information, are also included in the discussion. Then an MI-based damage detection technique is developed. For the illustration of the technique, a benchmark problem is discussed. The results from the benchmark problem show that the proposed technique works efficiently when identifying the connections between nodes.

Chapter 4 presents a novel application of the developed techniques in Chapter 3 for damage detection in bridge structures. In this study, the Waddington bridge,

which is located along New York State Route 345 over Big Sucker Brook in the town Waddington, NY is considered. The bridge span was instrumented in a rectangular grid array at 30 locations with dual-axis accelerometers. The damage to the bridge was introduced by removing bolts from the first diaphragm of the bridge and three status of the bridge. Two damage scenarios were compared with the baseline structures. Much of the details is taken from Ref. [43].

Chapter 5 presents a full wave inversion method for sinkhole detection in the subsurface. At the beginning of the chapter, some exciting new methods in locating sinkholes are presented with advantages and disadvantages. Then the FWI technique is introduced. The computational efficiency and the memory requirements of this approach are addressed by developing a different cell size method. The efficiency of the different cell size method is discussed with the results obtained for a synthetic model.

A non-uniform mesh refinement method for simulation of wave equations with small scale heterogeneities using staggered grid scheme is presented in Chapter 6. Cubic smoothing spline interpolation is used for spatial mesh refinement. To this end, the results of the wave propagation with and without cubic spline interpolation are presented.

Chapter 7 presents the conclusions and future work. One of the ongoing project is based on application to earthquake predictions using information theoretic measures. The oMII method introduced in Chapter 3 shows great promise for damage detection in complex structures. With some modification to the algorithm and using machine learning techniques, we plan to apply this technique for the prediction of earthquakes. Furthermore, Chapter 7 presents a description, data classification, and some basic results of the ongoing work of this project. Another ongoing project is to develop the FWI technique for 3D seismic wave propagation. We plan to test the techniques used in Chapter 5 and Chapter 6 for real-time experimental data. The necessary back-

ground in probability theory is covered in Appendix A. Appendix B and Appendix C include some featured articles published on SIAM news and American Institute of Physics news.

Chapter 2

Nondestructive Damage Identification Methods: A Literature Survey

As a result of many normal operations and natural disasters, such as earthquakes, corrosion, and sinkholes, structural systems can be changed. Some of these changes often result in permanent changes to human societies and the environment. The changes that are introduced to the system harmfully can be defined as a damage [26].

Early prediction of damage can help in increasing the lifetime of a civil structure and prevent unexpected modes of failure. Therefore, health monitoring of civil engineering structures by means of damage detection methods is important. Among techniques, the methods that are not involving the destruction of structures during testing are called non-destructive testing.

In the literature, several non-destructive methods have been developed to monitor the structural damages of systems [6, 26, 29, 34, 35, 44, 45]. Based on the features of the methods, nondestructive damage identification methods can be categorized as either local or global [29, 35]. In the following, we describe these two methods

with examples and mathematical details. The advantages and disadvantages of these methods are also presented.

2.1 Local Non-destructive Damage Identification Methods

Non-destructive testings methods that can only be applied to small-scale (simple) structures and a portion of a large-scale (complex) structures are called "local" non-destructive damage identification methods [46]. Some examples of the popular localized damage identification techniques are ultrasonic methods or acoustic methods [44], magnetic field methods [6], radiography [6], eddy-current methods or thermal field methods [6], and liquid penetrant testing methods [29].

Ultrasonic methods, which are based on sound wave propagation, are used for many health monitoring applications [3]. Ultrasonic waves such as Rayleigh and Lamb waves, can propagate long distances and reveal damages. Lamb-waves based techniques are able to characterize many frames of damage in composite materials. Figure 2.1 shows the principle of ultrasonic testing for detection of the depth of a defect. The left-hand side and the right-hand side figure show the sound wave propagation through a non-defective test material and a defective test material, respectively. A probe sends a sound wave into the test materials. There are two indications in the non-defective test material and three indications in the defective test material. The depth of the defect can be determined by the ratio D/E_p, where E_p is the distance between the initial pulse of the probe and back wall pulse. D is the distance between the initial pulse and the pulse from the defect.
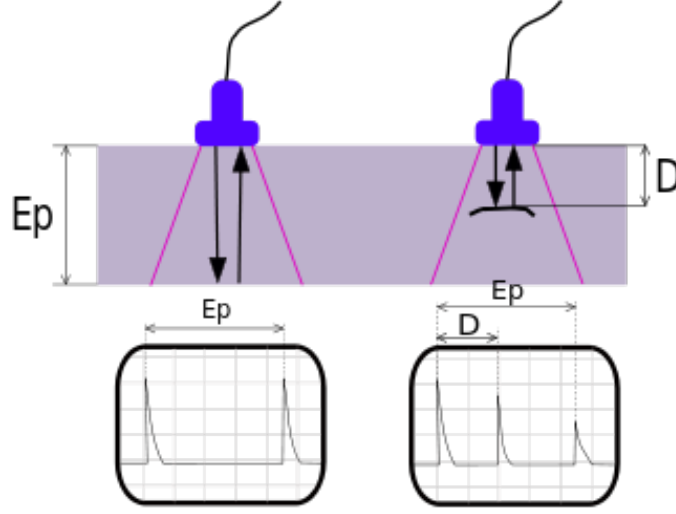
Figure 2.1: The principle of ultrasonic testing for detection of the depth of a defect (photo credit: Ref. [3]).

Guided wave techniques is another type of ultrasonic method. Ultrasonic-guided wave analysis techniques provide greater sensitivity for damage detection even when using low frequencies [45]. This technique allows the inspection of hidden structures, structures under water, and coated structures running under the soil. Ref. [45] pointed out that conventional ultrasonic methods are only sensitive to gross defects, but much less sensitive to minor-damage. To overcome this issue, nonlinear ultrasonic techniques are also developed [45].

Magnetic field methods use magnetic fields to locate damage of a surface in ferromagnetic materials[1] [6]. There are many ways to apply the magnetic field to the surface. Examples of such types are applying an electromagnet to the surface (magnetic flow), passing a large current through the specimen or locally by means of current prods (current flow), and putting the specimen inside a current-carrying coil or forming a coil around the specimen. When a surface has a crack or damage, the magnetic field produces a flux leakage area since the magnetic flux lines do not travel well in the air or void. Thus, by applying magnetic particles, which are colored with

[1]The ferromagnetic materials are those substances which exhibit strong magnetism in the same direction of the field when a magnetic field is applied to it [47].

a visible dye or a fluorescent dye, on to the top of the surface, the crack area can be identified. Figure 2.2 illustrates the behavior of magnetic flux near a crack on a surface. This method can be applied to all strongly magnetized metals, such as ferritic steels and irons [6].
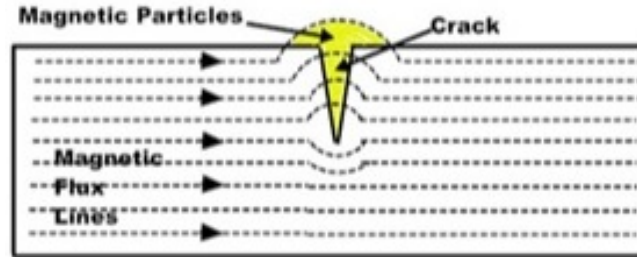
Figure 2.2: The magnetic flux lines near a crack on a surface (photo credit: Ref. [6]).

Radiography testing uses the idea of attenuation of material density and thickness [6]. A test material (with damage) is placed between a radiation source and a detector. The radioactive sources that are used for radiography testing are X-ray and Gamma-ray. These sources emit radiation and penetrate radiation through the test material. Then the differences in absorption, which are recorded in the detector, are used to identify the damage [6]. Figure 2.3 illustrates the penetration of radiation through the test material. In testing, X-ray is used for thin or less dense materials such as aluminum. Gamma-ray is used for thicker or dense materials. For example, computed tomography (CT) is one of the non-destructive radiography testing methods used in industry. CT uses a computer to reconstruct both the cross-sectional plane and 3D volume images of the testing object. Thus CT is able to identify the internal discontinuities using every point in the plane and viewed from different directions.
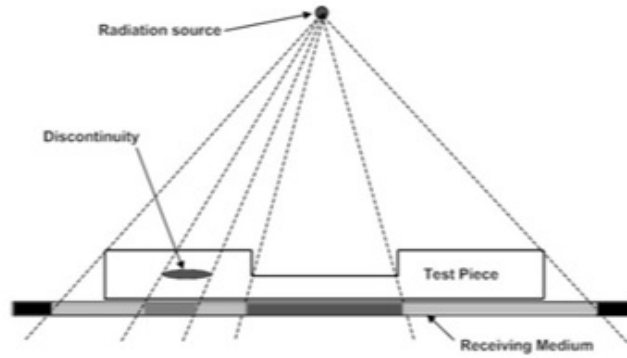
Figure 2.3: Radiation penetration through a test material (photo credit: Ref. [6]).

The eddy current technique is an electromagnetic testing method, which uses an alternating current coil to induce an electromagnetic field into a conductive test piece [6]. After applying the electromagnetic field, a small current is created around the magnetic flux field (See the Fig. 2.4). The flow pattern of the created current is known as "eddy current" and changes in the eddy current density are used to identify the discontinuities of the test material [6].
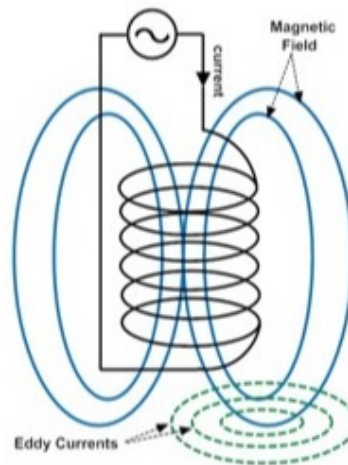
Figure 2.4: The flow pattern of the created current after introducing the magnetic field (photo credit: Ref. [6]).

In liquid penetrant testing, a very low viscosity liquid is used as the penetrant. The liquid is applied to a part of a surface and allows to penetrate into the voids in the

surface (see Fig. 2.5). After the excess liquid on the surface is removed, the penetrant in the voids will flow back out. Thus the voids on the surface can be identified [6].
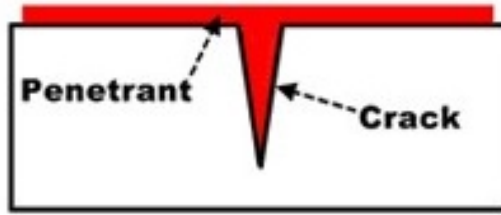
Figure 2.5: The penetrant flowing back out to indicate the void (photo credit: Ref. [6]).

These local experimental techniques require that the location of damage is known a priori and readily accessible for testing. This means damage can only be detected if the damage is on the surface of the structure [29, 35]. However, these requirements cannot be guaranteed in most cases in civil or aerospace engineering settings. Global damage detection techniques are developed to overcome these difficulties.

2.2 Global Nondestructive Damage Identification Methods

The damage detection techniques that can be used to identify damages in complex structures are called "global" techniques [46]. The vibration-based methods play an important role among global damage detection methods. The vibration-based techniques are based on the changes in physical properties such as mass, damping, and stiffness. Changes in these properties will cause detectable changes in modal properties such as natural frequencies, modal damping, and mode shapes when the damage is induced to the system.

According to the review in Ref. [26], most of the developments in vibration-based damage detection began during the 1970s and 1980s by the offshore oil industry. The

major area that they studied is detecting subsurface structural failure. They use the changes in the natural frequencies of the structure for their study. Subsequently, aerospace researchers used vibration-based damage detection techniques to study the development of the space shuttle in the late 1970s and early 1980s. In the early 1980s, the civil engineers studied vibration-based damage detection techniques for bridge structures.

Based on vibration features, the damage identification methods are classified into three major categories: natural frequency-based methods, mode shape-based methods, and curvature mode shape-based methods [35]. In the following, we discuss these three types of methods with examples.

2.2.1   Frequency-based Damage Detection Methods

The frequency-based methods observe the changes in structural properties that cause changes in vibration frequencies. There is extensive literature about frequency-related damage detection methods [7, 26, 31, 32, 34, 48]. A detailed review of the detection of structural damage through changes in frequency can be found in [26, 31, 32]. The presence of damage, such as cracking, fatigue, corrosion, and loosening of bolted joints in a structure, causes a reduction of stiffness. Due to stiffness reduction, natural frequencies in a structure will change [31]. Damage at different locations have different natural frequency patterns. By measuring the frequency changes in a structure, the damage can be identified. This is the most useful damage detection method, since frequencies can be quickly measured.

For instance, based on the knowledge of the damage-induced shifts in a pair of natural frequencies, a crack in a rod is identified [48]. Ref. [48] assumes the spatial vibration of the free vibration of an undamaged straight rod of length L is governed

by the differential equation

$$(a\left(x\right)u'\left(x\right))' + \omega^2\rho\left(x\right)u\left(x\right) = 0, \ x \in (0, L),$$

where $u\left(x\right)$ describes the mode and ω is associated with the natural frequency. The quantities $a\left(x\right)$ and $\rho\left(x\right)$ denote the axial stiffness and the linear-mass density of the rod. If a crack appears at the cross-section $s \in (0, L)$, the eigenvalue problem for a damaged rod is

$$(a\left(x\right)w'\left(x\right))' + \omega_d^2\rho\left(x\right)w\left(x\right) = 0, \ x \in (0, s) \cup (s, L),$$

where $w\left(x\right)$ describes the mode and ω_d is associated with the natural frequency. With specific boundary conditions, the solution of the boundary value problem that leads to crack detection of a rod is presented. It is found that there are certain situations concerning uniform rods in which the non-uniqueness of the solution may be considerably reduced by means of a careful choice of the data [48].

Frequency-based methods can be viewed as two problems: the forward problem and the inverse problem. In general, the forward problem can be defined as the problem of calculating or observing data for a particular model. For example, in frequency based damage detection methods, directly calculating frequency changes can be defined as the forward problem. The inverse problem is the problem of calculating parameters from the observed data. In frequency-based techniques, identifying the parameters, such as crack size and location, can be defined as the inverse problem. Some examples of such developed techniques and mathematical details for these two problems from the literature are presented below.

15

Forward Problem

The forward problem determines the natural frequency changes of a given occurrence of structure-based damage. Frequencies are predicted using a mathematical model and compared with the measured frequency [26].

For example, Ref. [33] developed a damage detection method based on a natural frequency mode and analyzes via finite element method. In that method, the author of the Ref. [33] modeled the changes in the natural frequency of a mode i of a damaged structure as a function of the position vector r and the reduction in stiffness caused by the damage, δK. Similar arguments are made for the undamaged case with $\delta K = 0$. By considering that there is no frequency change without damage, the authors show that the ratio of the frequency changes in two modes is only a function of damage location. Further, a perturbation analysis is presented to compute the changes in the natural frequencies due to localized damage.

Another example for the forward problem can be found in Ref. [34]. The authors of the Ref. [34] suggested a statistical method of identification using the generalized least squares criterion. Using the ratio of natural frequencies from both measured and analytical data, the damage was localized for a range of damage levels. The major assumption of the proposed method is that the relationship between the observed and theoretical frequency changes are in the form

$$
\left[\frac{\delta \Omega_r}{\delta \Omega_s} \right] = \alpha \left(\frac{\delta \omega_r \left(\rho \right)}{\delta \omega_s \left(\rho \right)} \right)^{\beta_1},
$$

where Ω_r and Ω_s are the actual frequency changes at modes r and s, ρ denotes the damage mechanism as well as the damage location, $\omega_r \left(\rho \right)$ and $\omega_s \left(\rho \right)$ are the natural frequencies of mode r and s, and α and β_1 are constants. Further, using the relation, the authors fit the measured data to a straight line using the generalized least squares criterion. Other solving techniques for the forward problem can be found

in [34, 49, 50].

Inverse Problem

The inverse problem based on frequency changes involves identifying the damage parameters, such as crack length, location [26]. Ref. [7] discussed a vibration method of non-destructively evaluating the integrity of structures. The authors of the Ref. [7] formulated a relationship between the possible damage sites and the stiffness of the damage. According to their derivation, the value of the stiffness of the damage K_x at the axial position of the unknown damage location x, is given by

$$\frac{1}{K_x} = -\left(\beta_{xx} + \gamma_{xx}\right)_{\omega=\omega_p-\Delta\omega_p} = -\left(\beta_{xx} + \gamma_{xx}\right)_{\omega=\omega_p-\Delta\omega_p},$$

where β_{xx} and γ_{xx} are the direct receptance [2] of a structure at the position x, $(\omega - \Delta\omega_p)$ is the reduced natural frequency of the pth and q^{th} modes due to the damage at x. To find the possible damage sites and the associated value of K_x, a graph superposing $-\left(\beta_{xx} + \gamma_{xx}\right)_{\omega=\omega_p-\Delta\omega_p}$ and $-\left(\beta_{xx} + \gamma_{xx}\right)_{\omega=\omega_p-\Delta\omega_p}$ are plotted against x.
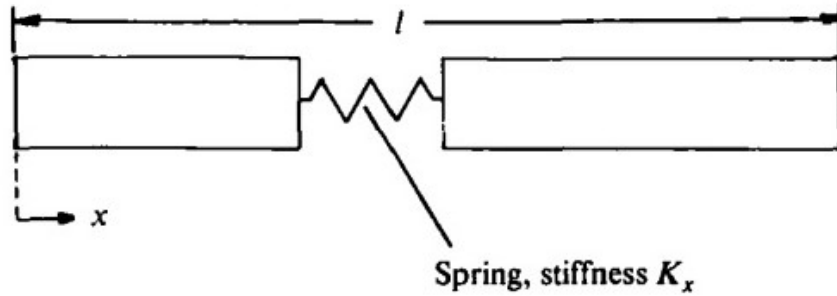
Figure 2.6: A cross section of a straight bar (photo credit: Ref. [7]).

For example, the stiffness of a straight bar of the constant cross-section (see

[2]The ratio of the resulting displacement to the exciting force in an oscillation or vibration.

Fig.2.6) can be obtained as

$$\frac{1}{K} = \frac{\cos\lambda x}{AE\lambda\sin\lambda x} + \frac{\cos\{\lambda\,(l-x)\}}{AE\lambda\sin\{\lambda\,(I-x)\}}$$

or

$$\frac{EA}{K} = \frac{1}{\lambda}\left(\cot\lambda x + \cot\{\lambda\,(l-x)\}\right),$$

where l is the total length of the bar, A is the cross-section area, E is Young's modulus, and F is the force amplitude. $\lambda = \omega\sqrt{\rho/E}$, where ρ is the density. Figure 2.7 shows the right-hand side of the above equation plotted against position x in a particular experimental situation for the first three modes of the bar. The intersections of the curves give the possible damage sites. Moreover, the authors validated the technique for one-dimensional structures, such as an aluminum bar with a saw cut.
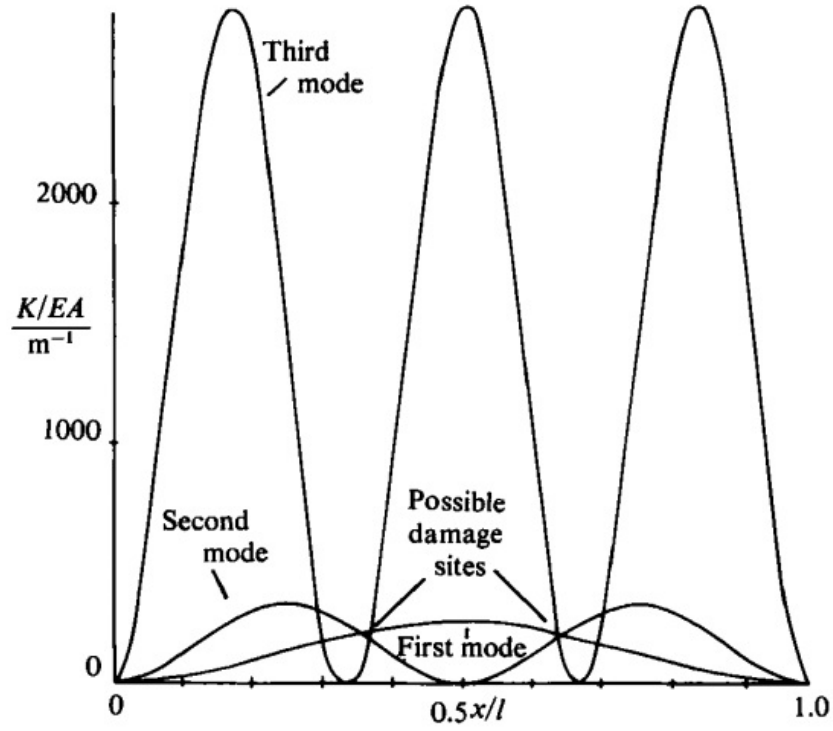
Figure 2.7: Damage location in a straight bar. (photo credit: Ref. [7]).

18

Another example of the inverse problem is presented in Ref. [51]. These authors developed a sensitivity and statistical based technique using frequency changes. They defined damage location assurance criterion (DLAC) for location (j) using a correlation approach.

$$\text{DLAC}\,(j) = \frac{|\{\Delta f\}^T \cdot \{\delta f_j\}|^2}{(\{\Delta f\}^T \cdot \{\Delta f\}) \cdot (\{\delta f_j\}^T \cdot \{\delta f_j\})},$$

where $\{\Delta f\}$ is the measured frequency vector for a structure with a single defect of unknown size or location, and $\{\delta f_j\}$ is the theoretical frequency change vector for damage of a known size at location j. DLAC takes the values between 0 and 1 where 0 indicates no correlation and 1 indicates an exact match between the patterns of frequency changes. The predicted damage site can be identified as the location j, which corresponds to the highest DLAC value. Further, the authors developed the DLAC formulations in such a way that multiple sites can be identified. For any combination of size and location of damage at one or more sites, the multiple damage location assurance criterion (MDLAC) is given by

$$\text{MDLAC}\,(j) = \frac{|\{\Delta f\}^T \cdot \{\delta f\,(\{\delta D\})\}|^2}{(\{\Delta f\}^T \cdot \{\Delta f\}) \cdot (\{\delta f\,(\{\delta D\})\}^T \cdot \{\delta f\,(\{\delta D\})\})},$$

where $\{\delta D\}$ is the stiffness reduction factor, which is introduced such that $D_j = 1$ for no damage and $D_j = 0$ for $100\,\%$ damage. The method is validated experimentally and numerically.

A method to nondestructively locate and estimate the size of a crack is presented [8]. These authors used the changes in natural frequencies of a structure by limiting the discussion to the systems which can be modeled by Euler-Bernoulli beams. They obtained a relationship between the crack depth and the fractional changes in the ith eigenvalue as

$$\frac{\delta \lambda_i}{\lambda_i} = \eta S_{ik} \left(\frac{a_k}{H}\right)_i^2,$$

where $\left(\frac{a_k}{H}\right)_i$ is the dimensionless crack size at the kth location defined in the ith mode, and η is a constant value on beam dimensioning, crack types, and Poisson's ratio. S_{ik} represents the sensitivity of the kth location in the ith modal strain energy, which is given by

$$S_{ik} = \frac{\int_k \{\phi_i''\}^2 dx}{\int_0^L \{\phi_i''\}^2 dx}$$

with mode shape ϕ_i and the beam span length L. If the quantities $\frac{\delta\lambda_i}{\lambda_i}$ and S_{ik} can be determined numerically or experimentally, then the crack size can also be determined using the above relationship. Further, a method to determine the crack location is developed by linearly relating the structural system's sensitivity of modal characteristics to the eigenfrequency changes due to geometrical changes [8]. The authors in Ref. [8] considered the case where the system is ill-conditioned when the number of damage parameters is greater than the number of modes. Ref. [8] used the prediction formula suggested in Ref. [52] to determine the damage inflicted at a predefined location. For an MDOF [3] structural system where the number of damage parameters is close to the number of modes, the damage inflicted at the predefined location may be predicted using

$$\sum_{j=1}^{NE} F_{ij} \alpha_j = Z_i.$$

Here NE is the elements, F_{ij} is the modal sensitivity of the ith modal stiffness with respective to the jth element, α_j is the measure of damage at the jth location, and Z_i is the fractional change in the ith eigenvalue. In their work, with a measured set of NM vibrational modes, a single damage indicator(DI) is defined for the qth location as

$$DI_q = \left[\sum_{i=1}^{NM} \left(\frac{Z_m}{\sum_{k=1}^{NM} Z_k} - \frac{F_{mq}}{\sum_{k=1}^{NM} F_{kq}}\right)^2\right]^{-1/2}.$$

The term in the parenthesis represents the localization error for the ith mode and the

---

[3]Multiple Degree of Freedom Systems

q^{th} location. DI takes the value in the range between 0 and ∞ and as the element q if DI_q approaches a local maximum, then the damage is located. For example, DI values calculated for a uniform beam with a crack is shown in Fig 2.8. The location corresponding to the maximum peak value of DI gives the crack location. With the experimental results, the authors of Ref. [8] concluded that cracks can be confidently located with a relatively small localization error.
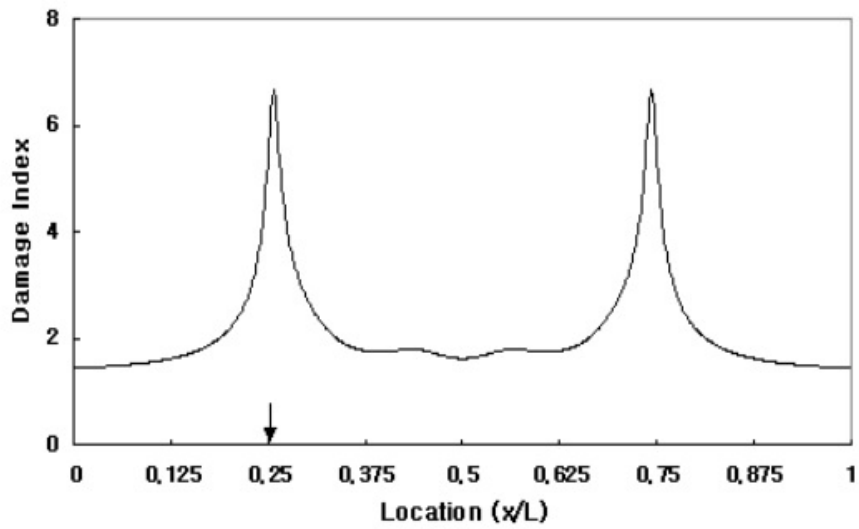
Figure 2.8: A crack localization in a beam. (photo credit: Ref. [8])

More examples of the inverse problems can be found in [53–56]. In conclusion, frequency change-based damage detection methods can be applied to simple structures with small cracks. Even though many researchers have developed natural frequency changes-based techniques for damage detection, these methods have some limitations. One limitation is that the natural frequency of some structures changes due to ambient conditions as well. Therefore, one cannot say significant frequency changes alone imply the existence of damage in a structure. Also, these frequency-based methods can be applied to localize and quantify damage in simple structures only with a small damage. Therefore, it is not trustworthy to use these methods for damage detection

methods in complex structures [35].

2.2.2   Mode Shape-based Damage Detection Techniques

A mode shape-based method is a technique that can be used to overcome the above limitations. Mode shapes are the shape of structures associated with different natural frequencies of a system. A Mode shape-based method is based on the behavior of the mode shapes. These methods use changes in the mode shapes in the damaged structure and healthy structure for damage identification. Mode shapes are less sensitive to other ambient conditions, such as temperature, than the natural frequency [35]. Thus, the mode shape-based method is the most popular method used in damage identification. In the literature, many damage detection methods are developed based on mode shapes [9, 10, 57, 58]. Here we present a few examples from such developed techniques.

An error localization technique based on damage detection using mode shapes is developed in Ref. [57]. By calculating mode shape differences, the physical location on the structure where stiffness differences exist between the two models is identified [57]. This technique is based on the Structural Translation and Rotation Error Checking (STRECH) concept. For example, the translation STRECH ratio for a system with only one displacement coordinate is

$$S_t = \frac{u_{12}^c}{u_{12}^d},$$

where $u_{12} = u_2 - u_1$ is the difference of the displacement of two grid points u_1, and u_2, superscripts c and d represent the desired modal and the comparison modal, respectively [57]. Further, the authors of Ref. [57] defined the ratio for the three-dimensional cartesian coordinates system by considering rotational displacement. The authors calculated the STRECH ratio for a list of adjacent grids of two models of a structure.

The largest numerical STRECH ratio will locate the link where comparison modal is stretching more than the desired modal. The method is validated in application to a two-link robot arm.

Another example of mode shape-based methods can be found in Ref. [9], where a sensitivity-based and statistical-based method to detect structural damage using incomplete mode shapes is presented. Without reconstruction of the unmeasured information, the damage sites are localized in Ref. [9]. The authors of the Ref. [9] modified the natural frequency method, MDLAC introduced by Ref. [51]. They combined incomplete mode shapes to localize the damage. The correlation parameter is given by

$$\text{MDLAC}\left(\{\delta D_j\}\right) = \frac{|\{\Delta\Phi\}^T \cdot \{\delta\Phi\left(\{\delta D_j\}\right)\}|^2}{\left(\{\Delta\Phi\}^T \cdot \{\Delta\Phi\}\right) \cdot \left(\{\delta\Phi\left(\{\delta D_j\}\right)\}^T \cdot \{\delta\Phi\left(\{\delta D_j\}\right)\}\right)},$$

where $\{\Delta\Phi\}$ is the measured mode shape change vector with a dimension equal to the product of the number of measured modes and the number of sensor locations and $\{\delta\Phi\}$ is the analytical mode shape change at the same degree of freedoms for damage of a known size $\{\delta D_j\}$ at different location j. Using the formula, the sites with the greatest MDLAC values can be approximately localized as the damage sites. For example, Fig 2.9 shows the normalized MDLAC values obtained for a two-dimensional truss structure, which consists of 31 elements. The element corresponding to the highest MDLAC value was identified as the true damage site. Notice that the actual damage is at the 16th element and the results also show the damage site is at the same element.
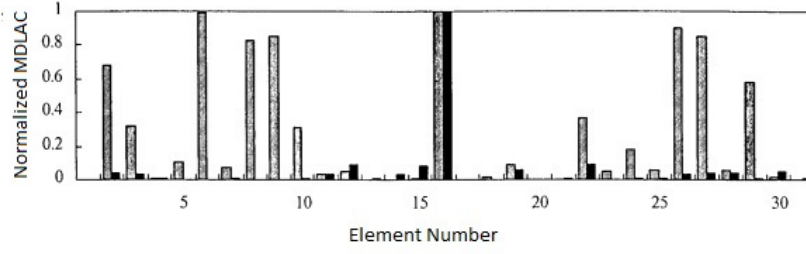
Figure 2.9: Normalized MDLAC values at the 31 elements bar truss structure. (Photo credit: Ref. [9])

Moreover, the authors of Ref. [9] defined the sensitivity of the kth mode shape to damage at element j as

$$\frac{\partial \{\phi_k\}}{\partial D_j} = \sum_{r=1}^{n^*} \frac{-\{\phi_r\}^T \cdot [K_j]\{\phi_k\}}{\lambda_r - \lambda_k} \{\phi_r\} \text{ for } r \neq k,$$

where $\{\phi_k\}$ is the kth analytical mode shape, λ_k is the kth eigenvalue, and n^* is the number of analytical modes, which is the total degree of freedom (DOF) in the system. Also, the mode shape vector for m modes from several sites is expressed as

$$\{\delta \Phi\} = \begin{bmatrix} \delta \Phi_1 \\ \dots \\ \delta \Phi_m \end{bmatrix} = \begin{bmatrix} \frac{\partial \{\Phi_1\}}{\partial D_1}\} & \dots & \frac{\partial \{\Phi_1\}}{\partial D_L} \\ \dots & \dots & \dots \\ \frac{\partial \{\Phi_m\}}{\partial D_1}\} & \dots & \frac{\partial \{\Phi_m\}}{\partial D_L} \end{bmatrix} \{\delta D\}$$

Using numerical simulations with a finite element model, Ref. [9] showed that this strategy is effective and attractive for practical use.

A method using fractal dimension (FD) analysis was developed to identify the cracks in beam structures and plates [10, 58]. This method also uses vibration signal analysis. The proposed technique used an FD-based crack detector and adopts Katz's

24

estimation [59] of the FD. The FD estimate of a curve defined by a sequence $\{n\}$ is

$$\text{FD} = \frac{\log_{10}(n)}{\log_{10}(d/L) + \log_{10}(n)},$$

wherere $d = \max\{dist(1, i)\}$ and i is the ith point of the sequence. L is the total length of the curve and $n = (L/\text{average step size})$ is the number of steps in the curve [59]. Then, the authors of Ref. [10, 58] developed 1D-FD-based crack detector (FDCD) technique as follows:

1. First, a sliding window of $[M = 0.4/dx]$ sample length was employed, where dx is the distance resolution in the acquisition of the vibration signal.

2. Next, the M-sample window was shifted along the N-sample section of the vibration signal, with a 99 % percentage of overlap.

3. Then, FD is computed over each vibration signal segment obtained from the sliding window.

4. Mid-point of the window was set as the estimated FD value.

Moreover, they improved the scheme to a 2-D-FDCD scheme for the analysis of two-dimensional structures, such as plates [10]. To estimate the crack depth, FD energy based formula was used

$$E_{FD} = \frac{1}{N_c^2} \sum_i \sum_j FD\,[i, j]^2,$$

where $(i, j) = 1, 2, ..., N_c$. Here N_c denotes the number of samples corresponding to the crack length $2c$. Figure 2.10 shows the estimated FD of a beam for small cracks at a specific crack location. The beam structure was analyzed and both the location and size of the crack are estimated. The authors in the Ref. [10] showed that crack predictions can be made accurately. Moreover, the technique is able to

efficiently track changes of all crack characteristics, such as location, length, and depth. Further, they showed that the method is computationally inexpensive and suitable to use in experimental data analysis.
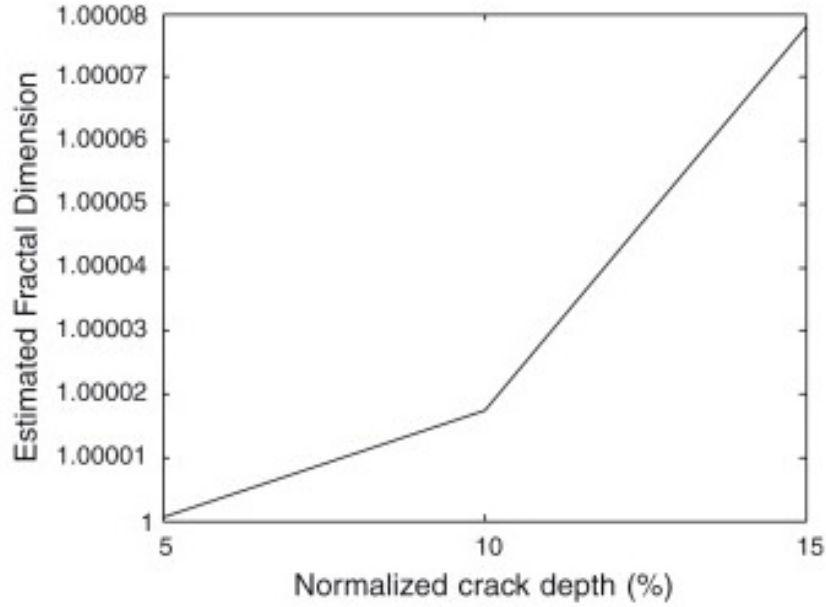
Figure 2.10: FD values as a function of crack depth.(photo credit: Ref. [10])

A method that uses a combination of Modal Assurance Criterion (MAC), Coordinate Modal Assurance Criterion (COMAC), and sensitivity analysis to detect damage in steel framed structures is presented in Ref. [11]. MAC evaluates the correlation between two sets of vectors. By checking the correlation between the experimental modal vectors at different stages, the occurrence of damages in structures can be found [11]. The MAC is not able to locate the position of damage. However, COMAC, which is developed from the MAC concept, is able to indicate at which coordinates the two sets of modal vectors deviate from each other. The COMAC method can be used to locate the damage only if the data used in the analysis consist of the vibrational response of the DOF that reflect the damage [11]. The proposed method in Ref. [11] can be described in three stages:

1. First, the sensitivities of the analytically-derived mode shapes to particular

26

damage conditions are computed to determine which DOFs are most relevant. The sensitivity of the modal vectors is given by

$$\frac{\partial \phi_{ij}}{\partial k_R} = \sum_{q=1}^{n} \alpha_{jq} \phi_{iq},$$

where

$$\alpha_{jq} = \begin{cases} \frac{-1}{(\omega_q^2 - \omega_j^2)} \left(\{\Phi\}_q \frac{\partial [K]}{\partial k_R} \{\Phi\}_j \right) & \text{for} j \neq q \\ 0 & \text{j=q}, \end{cases}$$

ϕ_{ij} is the modal vector, k_R is the rotational stiffness at a node, ω_q and ω_j are the natural frequencies of mode q and j, respectively. Here $[K]$ is the system stiffness matrix, $\{\Phi\}_q$ and $\{\Phi\}_j$ are the full modal vectors of mode q and j, respectively, and n is the total number of DOFs of the mathematical model [11].

2. Then, the MAC between the measured modes from the undamaged structure and the measured modes from the damaged structure is analyzed to select the correlated mode pairs. The MAC value between the ith mode of undamaged mode vector, $\{\Phi_U\}_i$, and the jth mode of damage modal vector, $\{\Phi_D\}_j$ is defined as

$$\text{MAC}\left(\{\Phi_U\}_i, \Phi_D\}_j\right) = \frac{|\{\Phi_U\}_i^T \cdot \{\Phi_U\}_i|^2}{\{\Phi_U\}_i^T \cdot \{\Phi_U\}_i \cdot \{\Phi_U\}_i^T \cdot \{\Phi_U\}_i},$$

where n is the DOF [11].

3. Using the modes and the DOFs selected in the step 2, the COMAC is computed using the following formula and the damage is localized:

$$\text{COMAC}(i) = \frac{\left(\sum_{L=1}^{L_{max}} | \left(\phi_{i,L}^U\right) \cdot \left(\phi_{i,L}^D\right) |\right)^2}{\sum_{L=1}^{L_{max}} \left(\phi_{i,L}^U\right)^2 \cdot \sum_{L=1}^{L_{max}} \left(\phi_{i,L}^D\right)^2},$$

where i the DOFs in the modal vector, L_{max} is the highest correlated mode pair number, L is the incremental counter of the mode pair number, and U, D stand for the undamaged and damaged case.

The calculated COMAC values by the authors of Ref. [11] for a steel structure is shown in Fig. 2.11. The results shows the damage is at node 9 (the node at the maximum COMAC value). Moreover, the authors demonstrated that the effectiveness of the proposed method is in locating the damage in the steel portal frame for both rigid and pinned joint conditions.
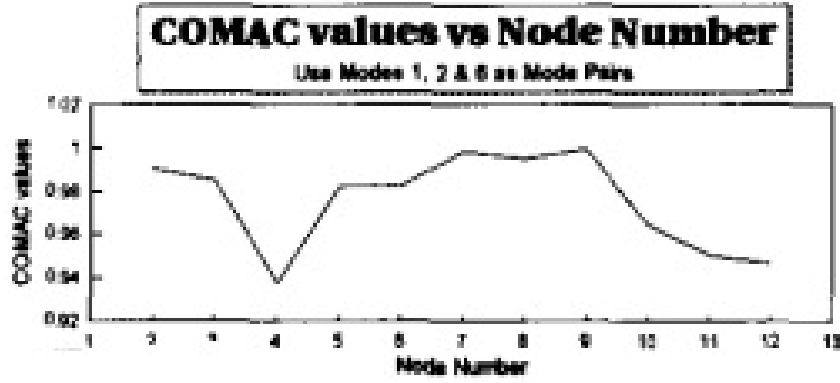
Figure 2.11: COMAC values for a steel structure. (photo credit: Ref. [11])

Even though these modal shape-based methods work well in identification and localization of damage in structures, these methods have some drawbacks. One of the drawbacks is these methods require measurements from a great number of locations. Another one is that the displacement mode shape itself is not very sensitive to small damage, even with the high-density mode shape measurements. To address the second issue, researchers introduce techniques based on mode shape curvature. The damage detection techniques based on mode curvature assume mode shape curvatures are highly localized to the damaged region.

2.2.3 Curvature Mode Shape based Damage Detection Techniques

Curvature mode shape is another parameter that is associated with natural frequency. The damage detection methods based on the mode curvature are called curvature mode shape damage detection techniques. These techniques assume mode shape curvatures are highly localized to the damaged region.

For instance, Ref. [12] presented a curvature mode shape method for identifying and locating damage in a structure. The curvature, ν'' at a point is given by

$$\nu'' = \frac{M}{(EI)},$$

where M is the bending moment at a section, E is the modulus of elasticity, and I is the second moment of cross-sectional area. When damage is introduced to a structure, the quantity EI is reduced and therefore the curvature increases. Thus the mode shape curvature changes can identify and locate the damage in a structure. The amount of the damage can be identified with the magnitude change in curvature [12].

The authors of Ref.[12] obtained curvature mode shape numerically from finite element analysis by using a central difference approximation as

$$\nu_i'' = \frac{\nu_{i+1} - 2v_i + v_{i-1}}{h^2},$$

where h is the length of the elements. They compared the results with natural frequency changes and mode shape changes. Figure 2.12 shows the absolute difference between the curvature mode shapes for an intact and a damaged cantilever. The maximum difference for each curvature mode shape occurs in the damaged region. For this case, the damaged region is between point 13 and 14 [12].
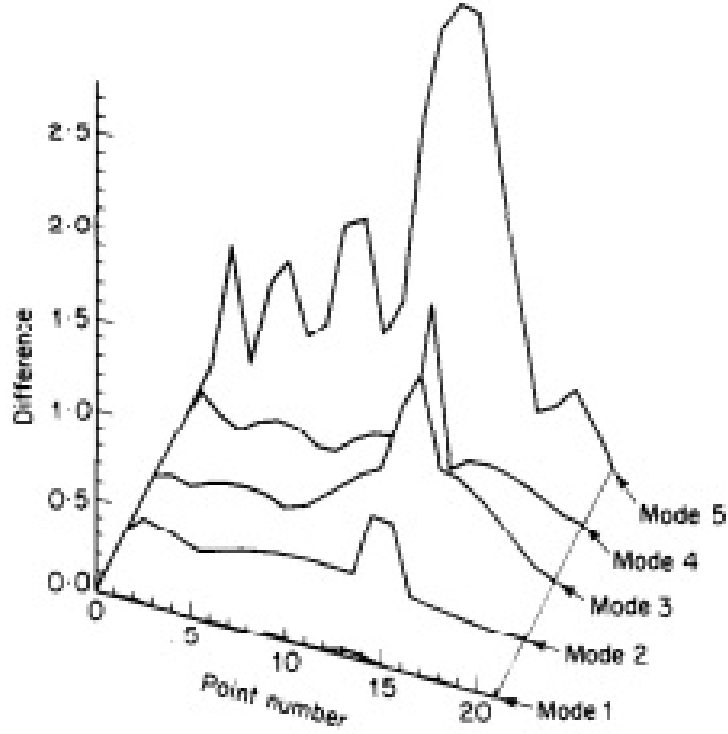
Figure 2.12: Differences between curvature modes. (photo credit: Ref. [12])

They showed that changes in the curvature mode shapes can be localized successfully for the simple supported beam and the cantilever beam model. Moreover, the authors showed that the MAC and COMAC methods are not able to detect the damage in the cantilever.

The application of the change in modal curvature to detect damage in a presented concrete bridge is presented in Ref.[13]. The authors of the Ref.[13] introduced a damage indicator called "curvature damage factor (CDF)" by considering the difference in curvature mode shapes for all modes:

$$\text{CDF} = \frac{1}{N} \sum_{i=1}^{N} |\nu_{0i}'' - \nu_{di}''|,$$

where N is the total number of modes and ν_0'', ν_d'' are the curvature mode shapes of the undamaged and damaged structures, respectively. For instance, CFD values for a

30

simple supported beam model are shown in Fig.2.13. The damage position is clearly identified at the peak node.
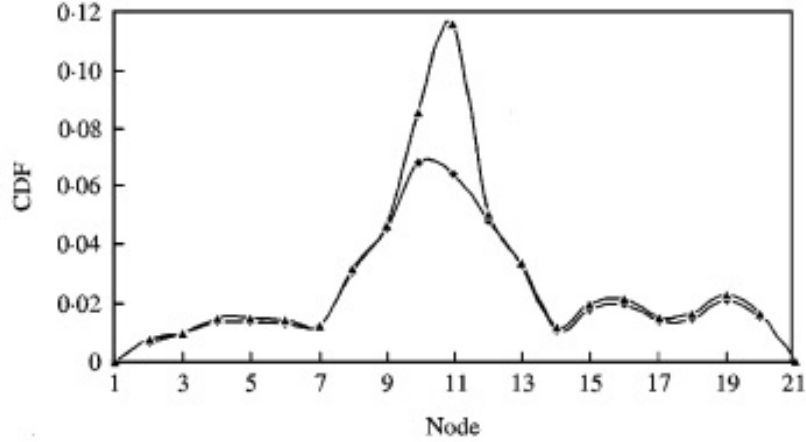
Figure 2.13: CDF values for a simple beam model. (photo credit: Ref. [13])

The authors in Ref. [13] showed that when the structure contains several damage locations, the CDF gives a clear identification of damage locations. Moreover, they showed that the technique is promising for identification of damage in civil engineering structures.

2.2.4   Other Methods

Overall, mode shape-based and curvature-based methods can be used for damage localization. However, these methods may be not be reliable in highly complex structures due to the time required for their development. Researchers have developed several other methods for structural health monitoring [14, 15, 60–62]. These include comparison of dynamically measured flexibility changes [60], modal updating-based methods [61] , neural network methods [14], and statistical methods [15, 62].

Dynamically Measured Flexibility Matrix Method

The changes in the static behavior of structures are used in the dynamically measured flexibility matrix method. The flexibility matrix is defined as the inverse of the static stiffness matrix. Therefore, the flexibility matrix relates the applied static force and then to the resulting structural displacement. Thus the structural damage can be identified using the stiffness of the structure. One example of this approach is presented in Ref. [60] in which the authors used a flexible approach for damage identification of cantilever-type structures with bending and shear deformation. They modeled the arbitrary cantilever-type structure as a lumped mass system and the structural damage is identified. The authors obtained structural eigenvalue equation as

$$[K]\{\phi\} - \omega_i^2 [M]\{\phi\}_i = 0,$$

where $[K]$ and $[M]$ are stiffness and mass matrix of the structure. ω_i and $\{\phi\}_i$ are the structural circular and modal shape vector of the ith mode. They showed that the approach only requires a small number of modes and it is convenient for practical applications. Other examples for the dynamically measured flexibility matrix method can be found in [63, 64].

Modal Updating Methods

Modal updating methods are based on an algorithm and update model parameters in an initial model to detect and localize damage. These methods use a modification of structural model matrices such as mass, stiffness, and damping solving an optimization problem. One of the classes of matrix update methods is sensitivity-based methods. Ref. [61] used the concept of inverse sensitivity equations. A linear or sequentially linearized relation that expresses the effect of parameter changes due to

the changes in the measurement data is formed as

$$[S]\{\Delta a\} = \{r\},$$

where $[S]$ is the sensitivity matrix calculated from the partial derivatives of the residuals r_j's with respect to the dimensionless parameters a_k in the model. Thus, the elements of the sensitivity matrix are given by

$$S_{jk} = -\frac{\partial r_j}{\partial a_k}.$$

This relation yields an ill-posed problem. Therefore, the authors of Ref. [61] used a regularization method to solve the problem. Using QR decomposition, the number of possible damage candidates is reduced to a minimum number and numerically stable, accurate solutions are obtained. Mathematically, the sensitivity matrix $[S]$ is decomposed into a product of an orthogonal matrix $[Q]$ and an upper triangular matrix $[R]$ as

$$[S][\Pi] = [Q][R],$$

where $[\Pi]$ is a permutation matrix that stores a column interchange [61]. Moreover, the authors presented other solution methods such as singular value decomposition and the iterative method of conjugate gradients. The authors illustrated the method for several examples.

Neural Network Methods

Alternative approaches through neural network methods were recently developed to monitor the structural health of a system [14, 65]. These methods are capable of extracting features in the data. Machine learning algorithms for damage detection under operational and environmental variability is presented in Ref. [14]. In applications,

operational and environmental variations can highly impact to the damage related features and damage level. Thus the authors of the Ref. [14] used intelligent features extraction procedure to overcome the issue. The proposed technique consists of three steps. In the first step, damage-sensitive features from the time-series measured from an array of accelerometers are extracted using an autoregressive model. Next, the effect of the operational and environmental variability on the extracted features is defined using four machine learning algorithms, auto-associated neural network (AANN), factor analysis (FA), Mahalanobis squared distance (MSD), and singular value decomposition (SVD). Then, a damage indicator is found with these machine learning algorithms. The damage indicator (DI) for AANN, FA, SVD algorithms are defined as the square root of the sum-of-square errors:

$$DI\left(i\right) = ||e_i||,$$

where $i = 1, 2, ..., k$ is a feature vector. In the undamaged condition, $DI \approx 0$ for the feature vector i . For the MSD algorithm,

$$DI\left(i\right) = \left(z_j - \bar{x}\right)^T \Sigma^{-1} \left(z_j - \bar{x}\right),$$

where $\bar{x}$ and Σ are the multivariate mean vector and the covariance matrix for the training matrix X and z_i is a new feature vector z_i. DI values calculated using these four algorithms are shown in Fig. 2.14. The black color shows the undamaged and the gray color shows the damaged state conditions.
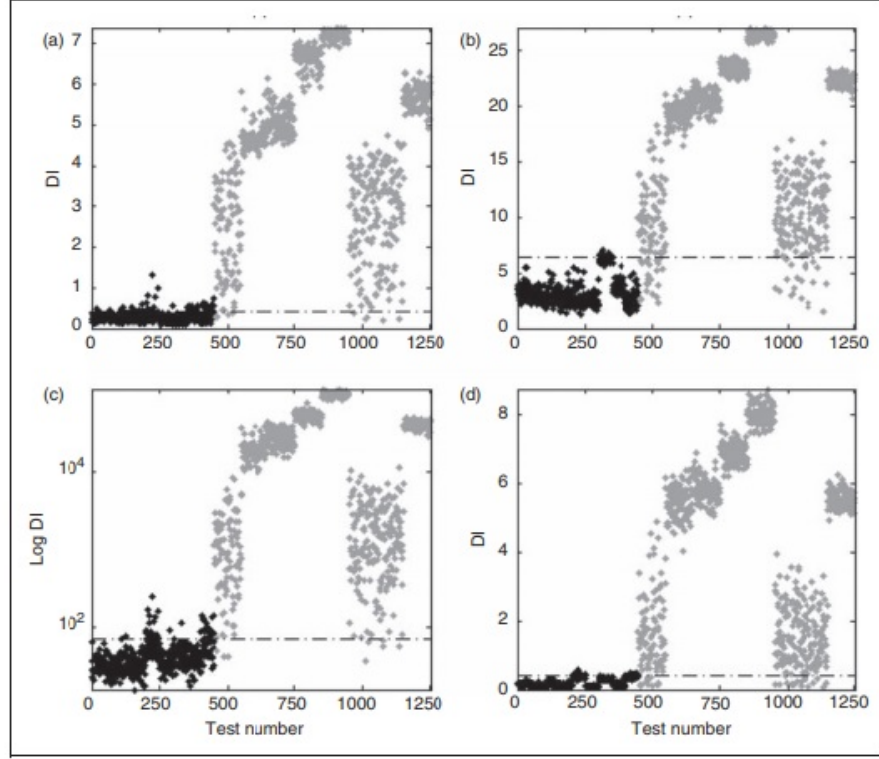
Figure 2.14: DI values calculated using the four algorithms. (photo credit: Ref. [14])

Even though these algorithms work effectively, they have some limitations. If the training data are only characteristic of a limited range of operational and environmental variability, one cannot guarantee that algorithms work efficiently when applied to a new data set [14].

Statistical Approaches

Many researchers have worked in the statistical approaches based damage detection techniques. Principal component analysis (PCA)-based health monitoring methods are presented in Ref. [15, 62]. These methods are based on pattern recognition to detect the damage of structures.

Ref. [15] presented a vibrational-based damage detection in an aircraft wing scaled model using PCA and pattern recognition. The authors of the Ref. [15] used the frequency response functions of the healthy and damaged structure as initial data.

PCA transforms the original n dimensional data into a lower dimensional data set and identifies the damage features. The authors developed the methodology for a scaled model of an aircraft wing. Distribution of the new feature vectors for an undamaged and a cracked wing is shown in Fig 2.15. These two categories are clearly detectable with the developed methodology.
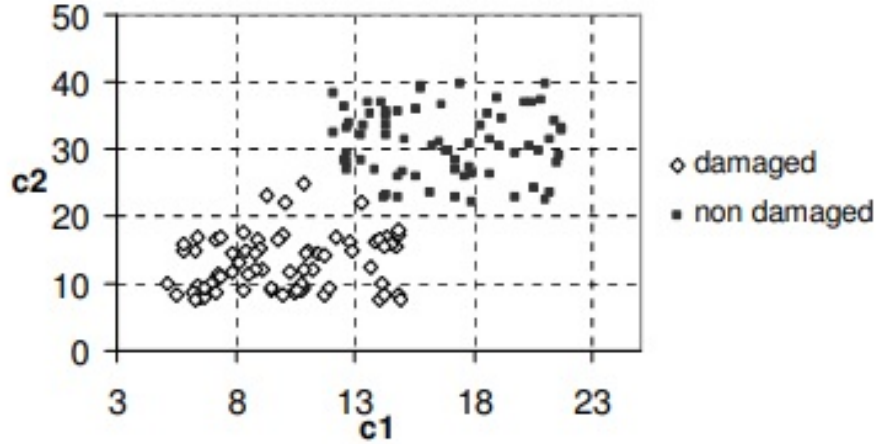
Figure 2.15: Distribution of the feature vectors for damaged and undamaged cases. (photo credit: Ref. [15])

The authors showed that the PCA and the pattern recognition procedure provide a better methodology for structural damage detection. However, PCA-based methods only perform linear transformations through the orthogonal components [15].

Chapter 3

Information-Theoretic Measures

3.1 Causality and Information Theory

Many researchers have been working on finding cause-effect relationships among variables or objects. Changes in one variable are systematically related to changes in other variables. Such a relationship that occurs between variables or objects can be defined as a causal relationship. However, some of the observed relationship may be a coincidence. Also, correlation does not necessarily guarantee causation. Thus a relationship between variables does not necessarily imply that a causal relationship exists[66–70]. Finding causal relationships is important in many processes and operations. For example, finding statistical evidence that money is "exogenous" in some sense in the money-income relationship [71] is important in Economics. Finding human influence on climate from hemispheric temperature relations [72] is important in Environmental studies. Finding such causal relationships becomes a challenging problem in a large-scale complex system because of the vast number of connections between different parts in the system [73].

The causation relationships of data observed as time series was first analyzed by Clive W.J. Granger [74]. He proposed that causality in economics could be tested by

measuring the ability to predict the future values of a time series using prior values of another time series. The two assumptions defined by Granger about the causal relationships are

1. The cause happens prior to its effect and

2. the cause has unique information about the future values of its effect.

Definition 3.1.1. *Granger-Causality Given stochastic processes* [1] *X and Y, X is said to Granger-cause Y if predictions of the value of Y based on its own past values and on the past values of X are better than predictions of Y based only on its own past values [74].*

Granger proposed a statistical hypothesis test, which he calls the Granger causality test, for determining whether one time series is useful in forecasting another. This test is based on a linear regression model and given by

$$Y_t = a_0 + \sum_{k=1}^{m} b_{1k} Y_{t-k} + \sum_{k=1}^{m} b_{2k} X_{t-k} + \epsilon_t, \tag{3.1}$$

where m is the specified number of time lags, $t = m+1, ..., N$, and ϵ_t are Gaussian noise with zero mean and variance σ^2 [77].

This linear model has been widely applied in many fields such as economics, finance, and natural sciences. To overcome the difficulties of applying this framework to nonlinear dynamical systems, many researchers proposed non-linear extensions of the Granger causality concept [73, 78, 79].

In conclusion, Granger causality can be treated as a theoretical framework. It can be used to assess directional dependencies between time series [80]. In addition, an information theoretic approach to the Granger causality plays an important role

---

[1]A stochastic process is defined as a collection of time-indexed random variables on a common probability space [75, 76]. In other words, the stochastic process has a system for which there are observations at certain times, and that observation at each time is a random variable. At each observation at a certain time, there is a probability associated with the outcome. This probability associated with the outcome depends on the previous observations.

in finding causal relationships in non-linear systems. Information theory is devoted to the analysis of dependencies through the definition of quantities that measure the uncertainty of variables using probabilistic concepts [80]. Therefore, in the following, we focus on the review of information theoretic measures. The rest of this chapter is organized as follows: Section 3.2 introduces some of the basic concepts, definitions, and theorems from information theory. The definitions are taken from Ref. [81]. With the aid of the basic concepts from information theory, we developed the optimal mutual information interaction (oMII) algorithm, which can be used to infer the direct and indirect influences of variables. We introduced the oMII algorithm in Sec. 3.3 and demonstrates the oMII to a simple benchmark problem in Sec. 3.4. The basic definitions of probability theory can be found in Appendix A.

3.2 Basic Measures from Information Theory

Information theory was first introduced by C. E. Shannon by means of communication in his paper titled "A mathematical theory of communication " in 1948 [82]. He defined modern digital communication and illustrated transmitting a message from a transmitter to a receiver using a model "Shannon paradigm." He determined how much information can be transmitted over a telephone line and the measures need to get a perfect signal on the other end. One of the most important things in a communication system is noise and how well the system deals with it. Shannon determined the effect of the noise to signal ratio in a communication system.

He represented a discrete information source as a Markov process (a special case of stochastic processes).[2] Shannon discussed the questions such as "how much infor-

---

[2]A Markov process is a process where all information that is used for predictions about the outcome at some time is given by most recent observation [75, 83]. Mathematically, a Markov process $\{X_t\}_{t=1,2,...}$ satisfies

$$P\left(X_{t+1} = x_{t+1} | X_t = x_t, ..., X_1 = x_1\right) = P\left(X_{t+1} = x_{t+1} | X_t = x_t\right)$$

mation is produced by a Markov process?" and "How to measure the information?."
To answer these questions, he introduced quantity entropy, which is based on the
probabilities of occurrences of events, as measures of information.

To understand the idea that Shannon introduced in Ref. [82], let's consider a
primary information source used for reporting m different number of messages. The
information source generates a sequence of m symbols. The total information carried
by all of the m symbols is associated with probability of occurrence of the messages.
Thus the average information over a symbol

$$H = -\sum_j p_j \log p_j, \tag{3.2}$$

where p_i is probability of occurrence of the ith elementary message i. The classical
researchers in statistical mechanics, such as Maxwell, Boltzmann, and Gibbsused,
used the summation in eq. (3.2) as H and it is proportional to the thermodynamic
quantity entropy [84]. Thus Shannon introduced H for this summation as "entropy"
or "average language information" in his investigation of information theory.

3.2.1 Entropy

Definition 3.2.1. *For a set of possible events with probabilities $p_1, p_2, ..., p_n$, the
entropy measures the expected uncertainty of the events, which is defined by*

$$H = \sum_{i=1}^{n} p_i \log(1/p_i) = \mathbb{E}_p(-\log p) \tag{3.3}$$

This can be interpreted as the negative of the expected value of $\log p$. This
quantity can be used to measure the information, choice, and uncertainty of a discrete
random variable X.

A simple example of this is the Bernoulli process. Entropy is measured in bits.
A random variable X takes values 0 and 1 with the probabilities $p(0) = p, p(1) =$

$1 - p = q$. The entropy of the random variable with logarithm base 2 is

$$H = -p \log_2 p - (1 - p) \log_2 (1 - p).$$

The entropy has the following properties:

1. $H \geq 0$

2. $H = 0$ if and only if all the p_i but one are zero, this one having the value unity.

3. For a given n and when all the p_i are equal, the H is a maximum and equal to $\log n$.

4. If X and Y are two random variables, then the joint occurrence of two random variables X and Y is $p(x, y)$. Thus the joint entropy is

$$H(X,Y) = -\sum_x \sum_y p(x, y) \log p(x, y) \leq H(X) + H(Y), \qquad (3.4)$$

where

$$H(X) = -\sum_x p(x) \log \sum_x p(x)$$

$$H(Y) = -\sum_y p(y) \log \sum_y p(y)$$

If the events are independent, then $p(x, y) = p(x) p(y)$ and equality holds in eq. (3.4).

5. For a random variable X and some deterministic function of X,

$$H(X) \geq H(g(X)). \qquad (3.5)$$

This property is called non increasing under functions. The equality occurs if and only if g is invertible.

41

3.2.2 Conditional Entropy

The joint entropy measures how much uncertainty there is jointly in the two random variables X and Y. The entropy is useful when determining the uncertainty in a single variable, but it does not measure the uncertainty in one variable given knowledge of another. The conditional entropy measures how much uncertainty remains on the random variable X when the value of Y is known. The conditional entropy of X given Y is

$$H\left(X|Y\right) = -\sum_{x,y} P\left(x,y\right) \log P\left(x|y\right) = -\mathbb{E}\left(\log\left(P\left(x|y\right)\right)\right). \tag{3.6}$$

3.2.3 Differential Entropy of Continuous Distributions

The above definitions and properties can be extended for a continuous random variable X with continuous probability distribution $f\left(x\right)$. One can attempt to prove that taking the limiting case of the above-defined entropy of a discrete distribution. The summation in the definition of entropy can be treated as a Riemann summation. For example, one can define the entropy of a $\mathbb{R}$-valued random variable X that takes the values in [0,1] by considering the probabilities of partition elements $\left[\frac{i-1}{N}, \frac{i}{N}\right]$ as $N \to \infty$.

$$H\left(X\right) = -\lim_{N \to \infty} \sum_{i=1}^{N} P\left(X \in \left[\frac{i-1}{N}, \frac{i}{N}\right]\right) \log P\left(X \in \left[\frac{i-1}{N}, \frac{i}{N}\right]\right) \tag{3.7}$$

One can further show that

$$H\left(X\right) = -\lim_{N \to \infty} \sum_{i=1}^{N} \frac{f\left(x_i\right)}{N} \log \frac{f\left(x_i\right)}{N} \tag{3.8}$$

$$= -\lim_{N \to \infty} \sum_{i=1}^{N} \frac{f\left(x_i\right)}{N} \log f\left(x_i\right) + \sum_{i=1}^{N} \frac{f\left(x_i\right)}{N} \log N, \tag{3.9}$$

by assuming X has a probability density function f and $P\left(X \in \left[\frac{i-1}{N}, \frac{i}{N}\right]\right) \approx \frac{1}{N} f(x_i)$, where $x_i \in \left[\frac{i-1}{N}, \frac{i}{N}\right]$. If the first term has a finite limit, one can prove $H(X)$ is not likely to converge.

$$H(X) = -\int_0^1 f(x) \log f(x)\, dx + \lim_{N \to \infty} \sum \frac{f(x_i)}{N} \log N \tag{3.10}$$

$$\approx -\int_0^1 f(x) \log f(x)\, dx + \lim_{N \to \infty} \log N \tag{3.11}$$

$$= \infty \tag{3.12}$$

Thus this cannot be used as a definition of entropy for continuous case.

Shannon introduced another approach by considering the left hand side integral in Eq.3.10. That integral looks a continuous version of Shannon entropy and he defined entropy for an $\mathbb{R}$-valued random variable.

Definition 3.2.2. *The differential entropy of a continuous random variable X is*

$$h(X) = \int f(x) \log (1/f(x))\, dx = -\mathbb{E}(\log(f(x))). \tag{3.13}$$

The conditional entropy of the random variable X given Y is given by

$$h(X|Y) = \int \int f(x,y) \log (1/f(x|y))\, dxdy, \tag{3.14}$$

where the joint entropy of a pair of continuos random variable (X, Y) with the joint probability distribution $f(x, y)$ is given by

$$h(X, Y) = \int \int f(x,y) \log (1/f(x,y))\, dxdy. \tag{3.15}$$

Some of the properties of the discrete random variables carry over to the continuous case, but some do not. For example, the non-negativity does not hold for the entropy of continuous random variables. So, $h(X)$ can be negative. For instance,

consider the random variable X uniformly distributed on the interval [a, b]. The entropy is given by

$$h\left(X\right) = -\int_a^b \frac{1}{b-a} \log \frac{1}{b-a} dx = \log(b-a)$$

This can be a negative quantity if $b - a$ is less than 1. Also, the non increasing under functions property does not necessarily hold.

3.2.4 Mutual Information

The joint and conditional entropies can be used to construct measures that detect the statistical dependence or independence between random variables as the case may be. Based on that, mutual information, which is another important measure in information theory, can be introduced. The mutual information (MI) between two random variables is the reduction of the uncertainty in one variable given another variable. Thus the MI between discrete or jointly continuous random variable X and Y can be defined as

$$I\left(X;Y\right) = h\left(X\right) - h\left(X|Y\right) = h\left(Y\right) - h\left(Y|X\right) = h\left(X\right) + h\left(Y\right) - h\left(X,Y\right). \quad (3.16)$$

One should notice that

$$I\left(X;Y\right) = I\left(Y;X\right).$$

In the case where the variables X and Y are independent, they have zero mutual information. MI is nonnegative $[I(X;Y) \geq 0]$ and equals zero if and only if $f(x,y) = f(x)f(y)$, that is, if X and Y are independent. It is often convenient to visualize the relationship among various entropies and mutual information in an information Venn diagram as shown in Fig. 3.1(a). The left circle represents the entropy of X and the right circle represents the entropy of Y. Then the intersection represents the mutual

information of X and Y. The joint entropy of X and Y is the union of two circles. Notice that the entropies can take negative values and thus the areas in the Venn diagram could be negative. When there is a third variable involved, the conditional mutual information (CMI) between X and Y given Z is defined as follows [85, 86],

$$I(X;Y|Z) = h(X|Z) + h(Y|Z) - h(X,Y|Z). \tag{3.17}$$

Like MI, the conditional MI obeys an analogous inequality, $I(X;Y|Z) \geq 0$, with equality if and only if X and Y are independent given Z. The relation between various entropies, mutual information, and conditional mutual information are visualized as an information Venn diagram in Fig. 3.1(b). If the upper left circle represents the entropy of X, the upper right circle represents the entropy of Y, and the lower circle represents the entropy of Z, then the conditional mutual information $h(X|Z)$ is the area of $X \setminus Z$. $h(Y|Z)$ is the area of $Y \setminus Z$ and $h(X,Y|Z)$ is the $X \cup Y \setminus Z$. The conditional mutual information, $I(X;Y|Z)$ is the area that shown in 3.1(b) shaded in black color.
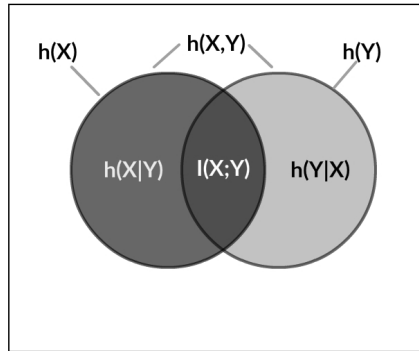
(a) Venn diagram for two variables   (b) Venn diagram for three variables
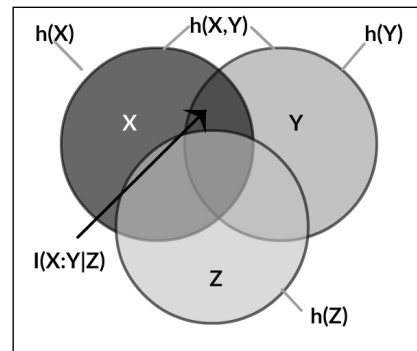
Figure 3.1: Information Venn diagram for two (a) and three (b) variables, respectively.

3.3 Optimal Mutual Information Interaction

In some applications, such as the studying of gene interactions [87], human brain [88], and power grid infrastructures [89], a large number of nodes and causal relationships are involved. It is challenging to differentiate these direct relationships without producing indirect and erroneous links. For example, Fig. 3.2 illustrates the direct and indirect causal links to the node i in a simple network. The direct nodes to the node i are j_1, j_2, j_3, j_4 and the indirect links to the node i are j_5, j_6, j_7. Our goal here is to identify these direct links by removing indirect links in the network.
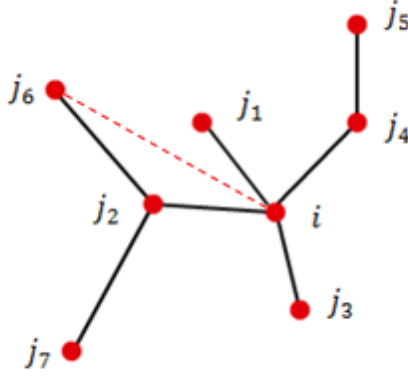
Figure 3.2: A simple network with direct and indirect causal nodes. The direct causal links to node i are j_1, j_2, j_3, j_4 and the indirect links to the node i are j_5, j_6, j_7.

A direct change or damage site may subsequently affect many further sites downstream. Thus, we develop a method called optimal mutual information interactions (oMII) as a technique of uncovering direct interactions.

The concept behind oMII is to select, based on conditional maximization of MI, the smallest number of channels that yield the largest MI, analogous to the oCSE principle that previously developed for causality inference [90]. The oCSE iterative discovery process has been previously developed to identify causal networks from time series [90].

One of the properties of the oCSE is the use of the time-shifted states of the variables. (See Definition 3.3.1). The number of samples required for the desired accuracy depends on the average rate at which information transfers through links between variables. If the transfer frequency is greater than the sampling frequency then the signal is quickly traveling between sensors. Thus the time shift between the states of the variables cannot be considered. Therefore, the oCSE algorithm cannot be applied to the problems with high signal transfer frequency compared to sample frequency. Notice that oMII is developed by considering the time shift to zero.

The application we consider in Chapter 4 is damage detection in bridge structures. The length of the bridge that we considered is 41.16 m and the distance between the two accelerometers is 2.14 m. A vibration signal travels across the bridge approximately at a speed of 3200 m/s. Then it takes 0.0126 s to travel one side of the bridge to the other side of the bridge. However, for the experiment, the number of samples per second (or sample rate) was 128 Hz. At this rate, the signal travels slower across the bridge and limited to reconstruct the signal.

To apply the oCSE method, one needs to measure the vertical acceleration at two states. If $a_i(t) = t$ m/s^2 is the acceleration at state i then the acceleration at state j is $a_j(t) = $ t $+ \tau$. Here $\tau = \frac{2.14}{3200} = 0.00067$ m/s^2 is the time that vibration takes to travel through the material. On the other hand, at the sample rate 128 Hz/s, if the acceleration at state j is t $+$ s, where s $= 1/128 = 0.0078$ s. With this time shift, oCSE is limited to reconstruct the signal. Thus the time shift between the states of the variables cannot be considered. Therefore, oMII is developed by considering the time shift to zero.

This phenomenon reminds us of the Nyquist Theorem or Sampling Theorem [91, 92], which also is fundamentally addressing the issue of sampling fast enough relative to the process being observed.

Theorem 3.3.1. *Nyquist-Shannon Sampling Theorem [92]. The Nyquist Theorem*

states that to reconstruct a signal, the sampling rate must be at least twice the highest frequency component of a signal f_{max} (or bandwidth of that signal). If the sampling rate is less than $2f_{max}$, then some of the frequency components in the signal will not be correctly reconstructed.

If the message signal has a bandwidth of B and a carrier frequency f_c, the upper frequency or the highest frequency of the modulated signal is $f_c + B$. Then the required sampling rate be larger than $2\left(f_c + B\right)$.

3.3.1 oCSE Algorithm

To distinguish between direct and indirect causality of networks, the oCSE uses the information measure "causation entropy." Causation entropy measures pairwise relationships of many variables in a network [90].

Definition 3.3.2. *Causation entropy [93]. The causation entropy from the set of nodes J to the set of nodes I conditioning on the set of nodes K is defined as*

$$C_{J \to I|K} = h\left(X_{t+1}^{(I)}|X_t^{(K)}\right) - h\left(X_{t+1}^{(I)}|X_t^{(K)}, X_t^{(J)}\right), \tag{3.18}$$

where I, J, K are all subsets of $\mathcal{V} = \{1, 2, ..., n\}$.

The problem of causal network inference can be thought of as the problem of estimating causation entropy among nodes [90]. For a set of nodes $I \subset \mathcal{V}$, this problem can be viewed as checking each node j independently to determine whether or not it is a causal parent of I. Mathematically,

Node $j \in N_I$ if and only if there is a set $K \supset N_I$, such that $C_{j \to I|(K-\{j\})} > 0$.

oCSE uses two algorithms to infer causal networks efficiently both computationally and using fewest data samples. Algorithm 1, which is called the Aggregative Discovery

of Causal Nodes, identifies nodes relevant to causal parents. Then Algorithm 2, which is called Progressive Removal of Non-Causal Nodes prunes away non-causal nodes or indirect nodes selecting only the causal parents.

Let $I \subset \mathcal{V}$ be a set of nodes and N_I be its causal parents. Then the sequence of numbers $\{x_1, x_2, ...\}$, nodes $\{p_1, p_2, ...\}$, and nested sets $\{K_0, K_1, K_2, ...\}$ can be defined as

$$x_i = \max_{x \in (\mathcal{V} - K_{i-1})} C_{x \to I | K_{i-1}} \tag{3.19}$$

$$p_i = \operatorname{argmax}_{x \in (\mathcal{V} - K_{i-1})} C_{x \to I | K_{i-1}}$$

$$K_i = \{p_1, p_2, ..., p_k\},$$

where $K_0 = \emptyset$. Then the Algorithm 1 and Algorithm 2 can be presented as follows [90]:

Algorithm 1 Aggregative Discovery of Causal Nodes [90]

    Input: Set of nodes $I \subset \mathcal{V}$
    Output: K (which will include N_I as its subset)
1: Initialize: $K \leftarrow \emptyset$, $x \leftarrow \infty$, $p \leftarrow \emptyset$
2: **while** $x > 0$ **do**
3:     $K_i \leftarrow K_i \subset \{p\}$
4:     **for** every $j \in (\mathcal{V} - K)$ **do**
5:         $x \leftarrow C_{j \to I | K}$
6:     **end for**
7:     $x \leftarrow \max_{j \in (\mathcal{V} - K)} x_j$, $p \leftarrow \operatorname{argmax}_{j \in (\mathcal{V} - K)} x_j$
8: **end while**

Algorithm 2 Progressive Removal of Non-Causal Nodes[90]

    Input: Set of nodes $I \subset \mathcal{V}$ and $K \subset \mathcal{V}$
    Output: $\hat{N}_I$ (inferred set of causal parents of I)
1: **for** every $j \in K$ **do**
2:     **if** $C_{j \to I | (K - \{j\})} = 0$ **then**
3:         $K \leftarrow K - \{j\}$
4:     **end if**
5: **end for**
6: $\hat{N}_I \leftarrow K$

In a similar manner, we introduce oMII algorithm by setting time lag to 0 and using conditional maximization of MI.

3.3.2 oMII Algorithm

Consider a multivariate time series $\{x_t^{(i)}\}$ that encodes the temporal variation of N components in a system, $i = 1, 2, ...N$.

For a given component i, the oMII approach infers a set of components that directly influence i as follows. First, in the "Discovery" stage (Algorithm 1), components are added one at a time to maximally reduce additional uncertainty as measured by conditional entropies, until no further reduction is possible. Then, in the "Removal" stage (Algorithm 2), each component inferred from the Discovery stage is examined and removed if such removal does not result in an increase of uncertainty regarding the time variability of i. In both stages, a shuffle test (Algorithm 3) is used to determine whether uncertainty reduction as measured by conditional MI is statistically significant.

Algorithm 3 Discovery stage

    Input: time series $X_t = \{x_t^{(i)}\}_{i=1,...,N;t=1,...,T}$ and component i
    Output: K_i
1: Initialize: $K_i \leftarrow \{\emptyset\}$, $p \leftarrow \phi$, $x \leftarrow 1$
2: **while** $x > 0$ **do**
3:     $p \leftarrow \text{argmax}_{j \neq \{i,K_i\}} I(X_t^{(i)}; X_t^{(j)}|X_t^{(K_i)})$
4:     **if** $(X_t^{(i)}; X_t^{(p)}; X_t^{(K_i)})$ passes the Shuffle Test (Algorithm 3) **then**
5:         $K_i \leftarrow K_i \cup \{p\}$
6:     **else**
7:         $x \leftarrow 0$
8:     **end if**
9: **end while**

Algorithm 4 Removal stage

    Input: time series $X_t = \{x_t^{(i)}\}_{i=1,\ldots,N;t=1,\ldots,T}$, component i, and set K_i

    Output: $\hat{K}_i$

1: **for** every $j \in K_i$ **do**
2:     **if** $(X_t^{(i)}; X_t^{(j)}; X_t^{(K_i/\{j\})})$ fails the Shuffle Test (Algorithm 3) **then**
3:         $K_i \leftarrow K_i/\{j\}$
4:     **end if**
5: **end for**
6: $\hat{K}_i \leftarrow K_i$

Algorithm 5 Shuffle test

    Input: time series $(X_t^{(i)} = \{x_t^{(i)}\}; X_t^{(j)} = \{x_t^{(j)}\}; X_t^{(K)} = \{x_t^{(K)}\}, \ t = 1, \ldots, T)$, threshold θ and number of shuffles N_s

    Output: pass / fail

1: **for** $\ell = 1, \ldots, N_s$ **do**
2:     generate a random permutation: $\sigma : \{1, \ldots, T\} \rightarrow \{1, \ldots, T\}$
3:     use σ to obtain a shuffled time series, $Y_t = \{y_t\}$, where $y_t \leftarrow x_{\sigma(t)}^{(j)}$
4:     compute $I_\ell \leftarrow I(X_t^{(i)}, Y_t | X_t^{(K)})$
5: **end for**
6: $S \leftarrow$ the $\lfloor (1-\theta)N_s \rfloor$th largest value from $\{I_1, \ldots, I_{N_s}\}$
7: **if** $I(X_t^{(i)}; X_t^{(j)} | X_t^{(K)}) > S$ **then**
8:     **output:** pass
9: **else**
10:     **output:** fail
11: **end if**

3.4   A Benchmark Problem

A simple test problem is created to validate the oMII algorithm. The time series data $\{X_t^i\}$ that has a multivariate Gaussian distribution is generated randomly. Here i represents the components and t represent the time index. The data is created to have mean $\vec{\mu} = \vec{0}$ and covariance Σ. The covariance matrix, which is the inverse of Laplacian matrix L, is calculated using a test network. The following steps are taken in the creation of the covariance matrix.

    1. Build a test network with set of nodes i.

2. Create the relevant adjacency matrix A such that

$$A_{i,j} = \begin{cases} 1 & \text{iff } i \leftrightarrow j \\ 0 & \text{otherwise.} \end{cases}$$

3. Define the matrix $L = D - A$, where

$$D = \begin{bmatrix} d_{1,1} & 0 & \dots & 0 \\ 0 & d_{2,2} & \dots & 0 \\ \dots & \dots & \dots & \dots \\ 0 & \dots & 0 & d_{n,n} \end{bmatrix}$$

4. Make a positive definite Laplacian matrix $\tilde{L}$ by adding the identity matrix to L.

$$\tilde{L} = L + I.$$

5. Set $\Sigma = \tilde{L}^{-1}$.

With the calculated Σ, the time series data is generated as $\{X_t^i\} \sim N(\vec{\mu}, \Sigma)$. The oMII algorithm is used to infer the direct influences between the nodes. The accuracy of the algorithm can be measured by comparing the inferred network (the predicted network) with the initial true network. Note that the spy graph of the adjacency matrix is used to presents the connections between nodes.

Fig 3.3(a) and (b) show connections in the true network and the prediction network created at 5 nodes and 10 nodes. The oMII algorithm uses two parameters, namely N_s and θ. N_s is the number of shuffles used in the shuffle test, and θ is the threshold in the shuffle test. Here $N_s = 100$ and $\theta = 0.01$ are used for the calculations. Five thousand (5000) sample data are used for the simulations. In Fig 3.3(a), we can see that the network connections in the predicted network are exactly the same as in the

true network. But in Fig 3.3(b), there are some new connections and lost connections in the predicted graph. The number of connections in the true network is 26 and in the predicted network is 25.

(a)

(b)
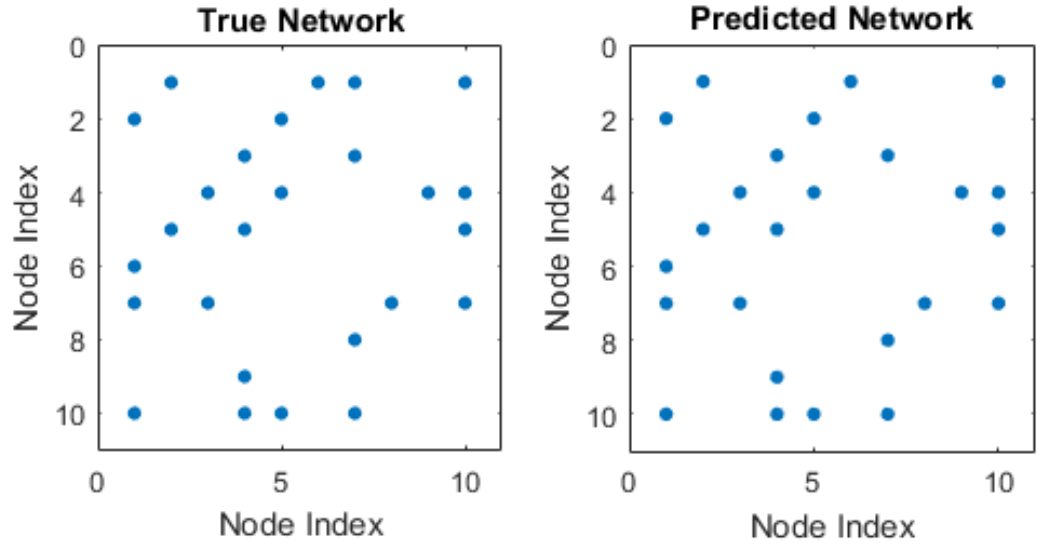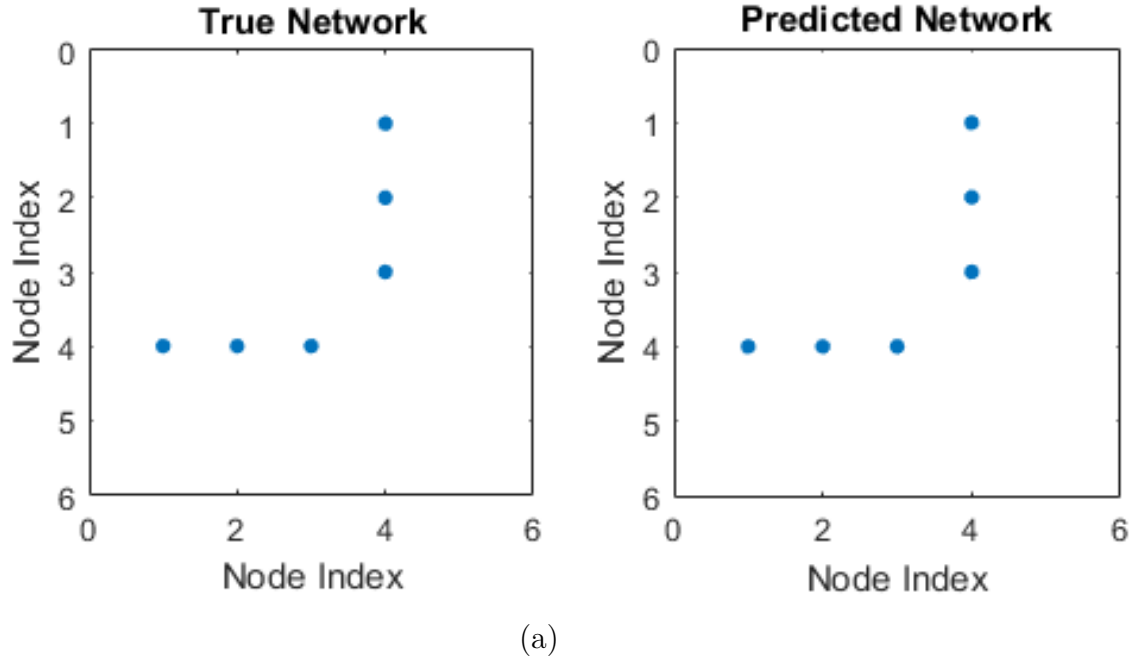
Figure 3.3: Comparison of the results with adjacency matrix at (a) 5 nodes, Ns =100, $\theta = 0.01$ and (b) 10 nodes, Ns =100, $\theta = 0.01$.

Figure 3.4 shows the true and predicted network connections at 10 nodes to the adjacency matrix shown in Fig. 3.3(b). The red color curve represents a connection that in the true network, but not in the predicted network.
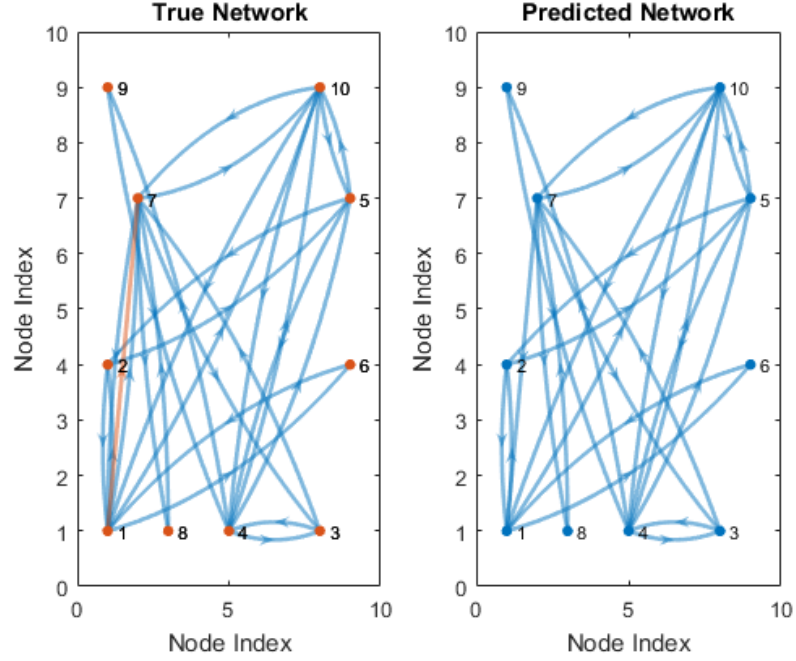
Figure 3.4: The number of connections in the true network and the predicted network as a function of nodes in the network at Ns =100 and $\theta = 0.01$

Further, we calculated the number of connections in a network at a different number of nodes. Fig 3.5 shows the number of connections as a function of a number of nodes. The predicted network connections are almost the same as in the true network. At some nodes, oMII over predicted the number of connections.
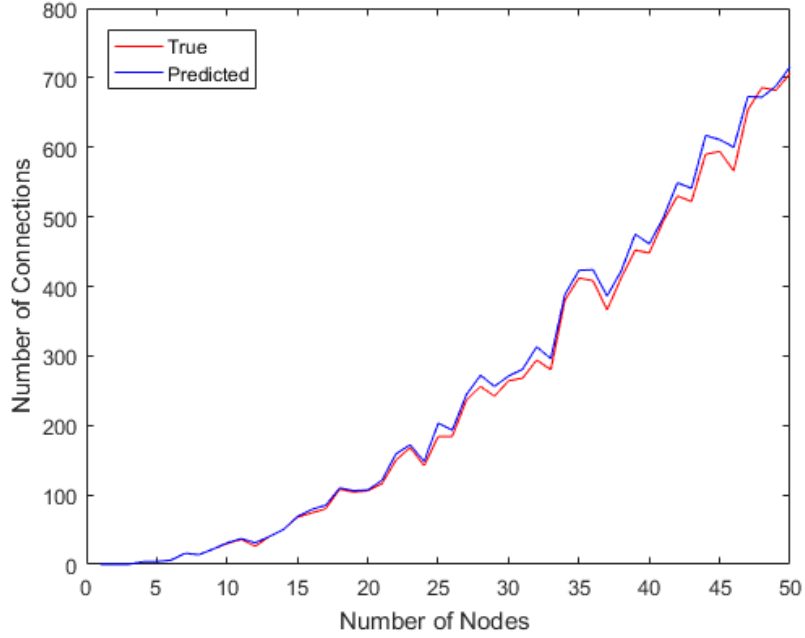
Figure 3.5: The number of connections in the true network and the predicted network as a function of nodes in the network at Ns =100 and $\theta = 0.01$

The network connections in the true network and the predicted network at $\theta = 0.1$ and $\theta = 0.001$ are shown in Fig. 3.6. There are 22 connections in the true network with 10 nodes. The number of connections of the predicted network at $\theta = 0.1$ is 24. oMII has over-predicted the connections between nodes at $\theta = 0.1$. However, when the $\theta = 0.01$, both true and predicted have exactly the same connections between nodes. It is worth to looking at false positive rate (FPR) and false negative rate (FNR) to check the efficacy of the method. We define the FPR and FNR as defined in Ref. [94]. Table 3.1 illustrates four events associated with condition A.

Table 3.1: Four events associated with a condition A on an experiment.

	Condition A	Not A
Test says "A"	True positive (TP)	False positive (FP)
Test says "Not A"	False negative(FN)	True negative (TN)

56

Then the false positive rate and false negative rate are defined as follows.

$$FPR = \frac{FP}{TP + FP} \tag{3.20}$$

$$FNR = \frac{FN}{TN + FN}. \tag{3.21}$$
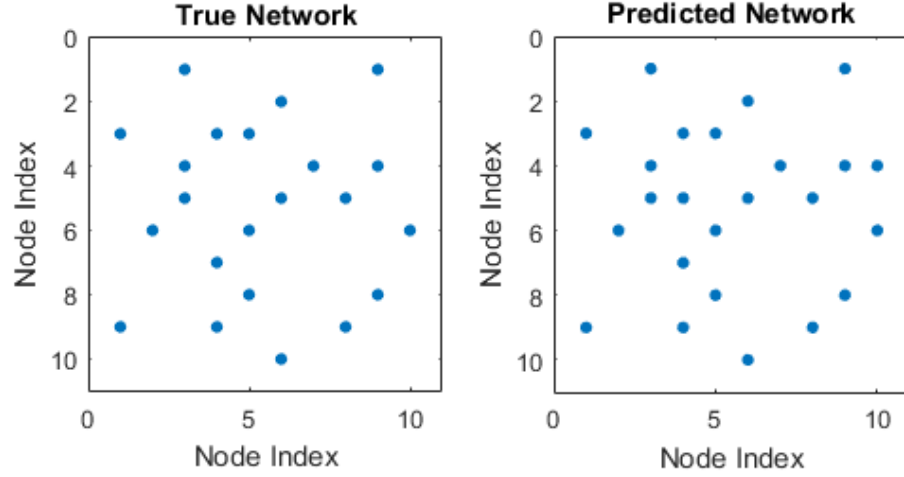
(a)
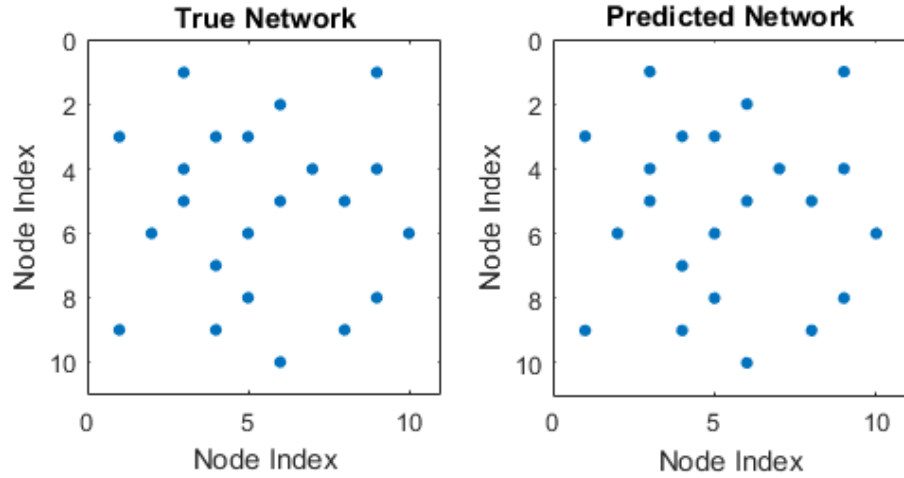
(b)

Figure 3.6: Comparison of the results with with (a) $\theta = 0.1$ and (b) $\theta = 0.001$ in the oMII algorithm. A network with 10 nodes at $N_s = 100$ and 5000 sample size is considered.

Figure 3.7 shows the FPR and the FNR at 20 independent simulations. These are done at different θ values. At any value of θ the FNR remains constant at zero. The FPR approaches zero as the θ decreases. Therefore, the accurate predictions can be made with oMII with a small θ value.
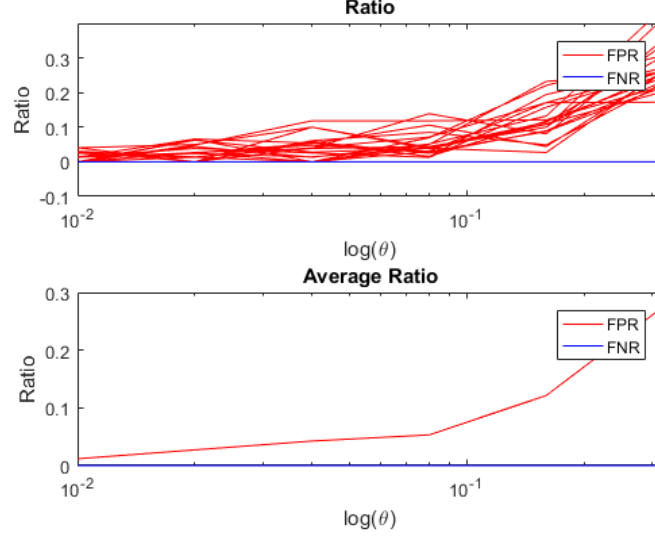
Figure 3.7: False positive and False negative ratio over the 20 independent simulations and the average of the rates.

Further, we analyze the effect of the sample size in the algorithm. Here $N_s = 100$, $\theta = 0.01$, and 10 nodes network are used. Figure 3.8 shows the average false positive and false negative ratios for different sample sizes at 20 independent simulations. When the sample size is more than 800, both ratios are approaching smaller values. Thus to get the accurate results with oMII, one needs to use a much bigger sample size.

59
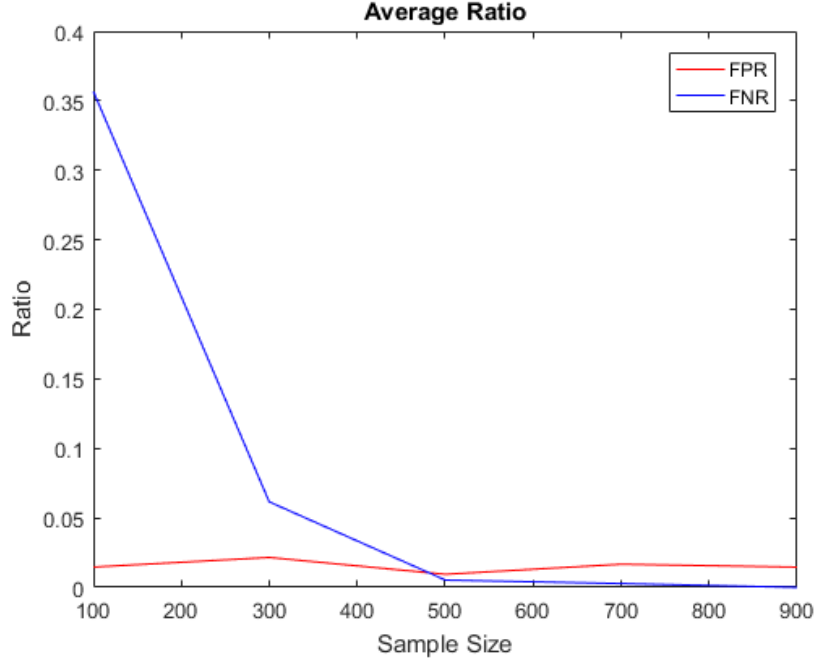
Figure 3.8: The average false positive and false negative ratio over the 20 independent simulations as a function of sample size.

In summary, the oMII method that was developed to uncover direct interactions is tested with a simple benchmark problem. The method is tested for a simple randomly generated data set. Results show that oMII is capable of identifying direct links to nodes in randomly-generated networks. The effect of the results at the parameters in the algorithm is discussed. To obtain accurate results, one needs to use a small θ values in the algorithm, because, the results show that the FPR and FNR approach to zero at small θ values. Also, results show that by using much larger data samples, accurate predictions can be made using the oMII algorithm. In conclusion, accurate predictions are guaranteed with at least 800 samples and $\theta \leq 0.01$.

Chapter 4

Noninvasive Damage Detection in Bridge Structures

In this chapter, we apply the oMII approach for damage detection in Bridge structures. These results are published in an article entitled "Information-theoretical noninvasive damage detection in bridge structures, *Chaos: An Interdisciplinary Journal of Nonlinear Science.* Here, we briefly describe the experimental instrumentation, statistical findings, and then show the results of the oMII computation. This work was also featured on SIAM news and American Institute of Physics news. These two articles are included in Appendix B and Appendix C.

4.1   Introduction

Damage detection of civil infrastructure such as bridges has gained considerable interest for obvious economic and public safety reasons. Damage here can be described as a change of material or geometrical properties that impact the performance of engineering systems [95]. In the literature there are many traditional methods to detect the damage of a bridge[13, 96–98]. Among them, non-invasive techniques are appropriate for many situations as they are non-destructive and often less expensive

at least as a precursory scanning approach, in case the more expensive and direct inspection methods are prescribed.

As dynamical properties of healthy and damaged bridges differ, parameters such as natural frequencies, damping ratio and mode shapes can be used to detect the presence of damage in a bridge. The modal curvature method, vibration based damage identification technique, has been used extensively in literature as the stiffness of the structure directly relate to the natural frequencies and mode shapes, [13, 96–100].

Model-based methods such as neural networks and genetic algorithms [101–103] have also been used as a basis to develop damage detection of bridges utilizing artificial intelligence and machine learning techniques. These methods have been be used to recognize patterns of the damaged and non-damaged systems. In [101] the study used a genetic algorithm based damage detection method, wherein the authors formulated the structure damage as an optimization problem. Moreover they used static displacements as measured responses. In [104], several drawbacks were discussed when adopting the traditional neural networks in dealing with patterns that vary over time. Also in [104], time-delay neural networks were proposed to detect the damage of railway bridges and compared with traditional neural networks.

In this chapter, we propose a mutual information (MI) based damage detection of a highway bridge, where the specific pairwise interactions are analyzed successively by an interaction analysis to uncover and detect interactions, and most importantly, changes in the way various regions of the structure may interact with each other as the system becomes damaged. We use optimal mutual information interaction (oMII) as explained in chapter 3 as analogous to our previously developed oCSE [90, 105, 106], as this is a method of uncovering *direct* interactions that are more indicatively sensitive to system changes. In the literature [107–114] many researchers used MI based techniques to analyze different dynamical fields.

Since the working premise is that a damaged bridge's dynamics are different, and

therefore so is the way vibrational energy may transmit through the structure, the MI of sensed accelerometers within the structure differs when comparing healthy bridge's pairwise MI to that of the same bridge later measured in a damaged state. Therefore, we assert definitively a principle that damaged verses undamaged bridges have different dynamics. Specifically direct influences may change due to damage. So comparing influences as inferred by oMII over time we claim that we can non-invasively detect important (damage) changes. Here we consider a specific bridge as our test platform. The New York State Route 345 bridge crosses over Big Sucker Brook, in the town of Waddington, NY and it was constructed in 1957. The instrumentation has involved 30 dual-axial accelerometers placed on the bridge at 30 locations therein. The test protocol has involved collection of data from three levels of damage as introduced by removing bolts from a diaphragm [115].

4.2 Information-theoretic Measures.

4.2.1 Spatial Pairwise Mutual Information

In many engineering applications such as the monitoring of mechanical structures, sensors are often placed spatially. This motivates a concept of spatial pairwise mutual information.

The idea of damage detection by information flow is to compare how signals measured from different spatial locations on the bridge respond to the challenge of the truck passage. Therefore, the idea is that the signals compared between sites, pairwise, may show a given coincidence as measured by MI when the bridge is in a healthy state, but the transmission of vibrational energy between sites becomes different if the bridge has been altered or damaged. *We assert that just as energy is transmitted by forces, similarly information associations detect the resulting changes of states.* The idea here is that the manner in which information flow occurs may be detectably

different between damaged and undamaged bridges. In particular, the MI between measurements at spatially nearby sensors pairs are dynamically different, considering a healthy bridge versus a damaged bridge. Rather than just MI of sensors with respect to each other sensors, we consider spatial pairwise MI carefully conditioning to isolate effects as we go. It is important to note that there is often a difference between direct and indirect influences. Most notably, if there is an indirect influence, the path of information flow may have many multiple channels through the structure, and therefore, even if damage diminishes one or many of the channels, then there still may be significant information flow when an influence is indirect. Thus the change might be hard to detect or masked if simply using the pairwise mutual informations without carefully conditioning. Therefore, it is important to identify the direct influences as the direct MI channels, as these are more sensitive to specific damage states. By our algorithm called oMII described in the next section that selects primary (direct) transmission channels, we consider the likely direct information coincidence of oMII as a more direct and sensitive measure of changes.

4.2.2 optimal Mutual Information Interaction (oMII)

It is important to distinguish between direct and indirect influences, because a direct change or damage site may subsequently affect many further sites downstream. So by identifying the most direct influences, we hope to both identify the specific location of changes and damage, but also this prevents what otherwise would be an overly populated map of (indirect) influences making it difficult to understand clear changes. Therefore,using oMII, the direct vibration transmission network routes in the bridge, between the sensor locations, can be identified, and most importantly, distinguished from the indirect influences. This iterative discovery process has been previously developed to identify causal networks from time series [90]. For the results shown here, we set the parameters $\theta = 0.1$ and $N_s = 100$ in the shuffle test.

4.3 Waddington Bridge Data: Description and Basic Statistical Properties

4.3.1 Description of the Waddington Bridge Data

In this section we describe the bridge that was used for damage detection, the instrumentation setup, and the levels of damage introduced to the structure.

The Waddington Bridge

The Waddingtonbridge, constructed in 1957, is located in New York State Route 345 over Big Sucker Brook in the town of Waddington, NY (see Fig. 4.1). The highway bridge investigated consists of a 19.1cm (7.5 in.) thick reinforced concrete slab supported by three interior $W33 \times 152$ and exterior $W33 \times 141$ steel girders over each span. The bridge has two-lane structures consisting of three 13.7 m (45 ft) simply supported spans carrying a total span of 41.7 m (137 ft) at an elevation of approximately 1.2 m (4 ft) from waterline. The girders have a center-to-center spacing of 2.1m (7 ft) and are supported by fixed and rocker steel bearings.

Figure 4.1: The Waddington Bridge, in New York State Route 345 over Big Sucker Brook in the town of Waddington, NY.

Instrumentation

In this case study, we use wireless sensor solution (WSS) for bridge health monitoring and condition assessment. The WSS was developed at Clarkson University as a versatile wireless sensing platform optimized for large scale, high rate, real-time acquisition [116, 117]. The system was developed based on off-the-shelf components to provide a low-power sensing interface for vibration, strain, and temperature measurements with signal conditioning tailored to the typical highway bridge response spectrum. The wireless communication is facilitated by a low-power chip transceiver employing direct sequence spread spectrum modulation over a 2.4GHz carrier frequency. Proprietary embedded software was used to sample data at an effective rate 128Hz.

The bridge span was instrumented in a rectangular grid array at 30 locations with dual-axis (vertical and lateral) accelerometers, in effect resulting in 60 vibration sensors.

The sensor locations are shown in the Fig. 4.2(a). The lateral and longitudinal spacing between these accelerometers are 2.13m and 1.96m, respectively.

Field Testing and Damage Introduction

The sequence of tests performed is outlined in Table 1. Each test consisted of the acquisition of approximately 90-second time history. Each case included three passes across the bridge with a truck in both directions. More explicitly, first test was performed for $\sim$ 90 seconds, and measurements of the sensors were taken after first pass of the truck, the second set of test measurements was taken after the second pass of the truck for another $\sim$ 90 seconds, and so on. In total 9 tests were performed.

Peak acceleration induced by the truck loading, as measured across the sampled locations, was generally 15mg, while peak lateral acceleration of 7mg was typical. The damage test was done with 6 bolts in 1st diaphragm connections (see Fig. 4.2(b)).

66
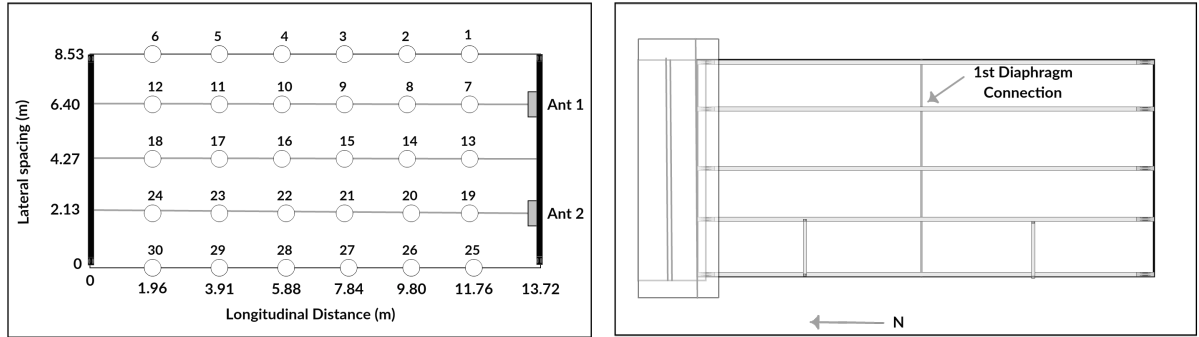
(a) (Top view) Physical spatial layout of the in- (b) Top view with the same orientation and cover-
dexed accelerometers, within the bridge structure. age area as in (a), here showing the location of the
The bridge is divided into three sections. When a 1st diaphragm connections where the damages are in-
truck goes by, its goes through all three sections. Introduced in the experiment.
this particular experiment, the sensors are placed to
cover one of these sections near one end of the bridge.

(c) Vibrational energy is introduced to the bridge
in a controlled manner by driving a truck over the
structure, both before and after damage has been
introduced

Figure 4.2: Physical layout of the accelerometers and the field test vibration intro-
duction.

Table 4.1: Baseline and Damage Test Scenarios.

Case	Test ID	Scenario	Comments
1	1-3	Baseline	"Healthy" Structure
2	4-6	1st diaphragm	Removal of four out of six bolts (Damage 1)
3	7-9	1st diaphragm	Removal of all six out of six bolts (Damage 2)

For each test (~ 90 seconds), lateral and vertical accelerations are measured and recorded at 128HZ, producing a raw time series $\{\tilde{x}_t^{(k)}\}$ for each sensor, where k denotes the index of the sensor as labeled in Fig. 4.2(a) and $t = 1, 2, \ldots, T = 11536$.

We standardize each raw time series by a linear transformation

$$x_t^{(k)} = \left(\tilde{x}_t^{(k)} - \mu(\tilde{x}^{(k)}) \right) / \sigma \left(\tilde{x}^{(k)} \right), \tag{4.1}$$

where $\mu(\cdot)$ and $\sigma(\cdot)$ denotes the empirical mean and standard deviation of the given time series $\{x_t\}_{t=1}^{T}$, that is, $\mu(x) = \frac{1}{T} \sum_{t=1}^{T} x_t$ and $\sigma(x) = \sqrt{\frac{1}{T-1} \sum_{t=1}^{T} (x_t - \mu(x))^2}$. Such transformation produces time series that have zero mean and unit variance. For the remainder of the paper we shall always deal with such standardized time series $\{x_t^{(k)}\}$.

4.3.2 Basic Statistical Findings - Laplace Distribution

Since the information theoretic entropies are in terms of probabilities, there is the necessity of good statistical estimation from sampled time series data. Recall that there is a total of 30 sensors, and 2 time series are measured and recorded at each sensor (accelerometer) location: lateral acceleration and vertical acceleration. Fig. 4.3 shows the distribution of the sensor time series plotted against two baseline distributions: the normal distribution and the Laplace distribution, both standardized to have zero mean and unit variance, given below:

$$
\begin{cases}
\text{(Normal distribution) } f(x|\mu, \sigma^2) &= \frac{1}{\sigma\sqrt{2\pi}} \exp{\frac{(x-\mu)^2}{2\sigma^2}}, \\[2mm]
\text{(Laplace distribution) } f(x|\mu, b) &= \frac{1}{2b} \exp{\frac{-|x-\mu|}{b}},
\end{cases}
\tag{4.2}
$$

with mean $\mu = 0$, $\sigma = 1$ (normal distribution), and $b = \sqrt{2}/2$ (Laplace distribution).

From the figure it is visually evident that the measured acceleration data more closely follow Laplace distribution than normal distribution. To draw this conclusion from a quantitative standpoint, we compute the l_1 norm between the standardized distribution of the time series for each sensor component and either a Laplace distribution or a normal distribution. The results are shown in Fig. 4.4, confirming that Laplace distribution is a better fit for the observed data across all sensors in all test scenarios.

We further establish the following theorem and prove some properties that holds for the entropy error for an independent and identically distributed source.

Theorem 4.3.1. *The entopy error, $eH(x)$ for an independent and identically distributed (i.i.d.) source X with probability distribution $\rho_1(x)$ and empirical distribution $\rho_2(x)$ is given by*

$$
|eH(x)| \leq ||(\ln \rho_1(x) - \ln \rho_2(x)||_1 + ||\rho_1(x) - \rho_2(x)||_1|| \ln \rho_2(x)||_1
$$

Then the following hold:

1. *If $\rho_1(x) = \rho_2(x)$, then $|eH(x)| = |H_1(x) - \hat{H}_1(x)| = 0$*

2. *If $||\rho_1(x) - \rho_2(x)||_1 < \epsilon/2M$, with $||\ln \rho_2(x)||_1 < M$ with $0 < \rho_1, \rho_2 < 1$ and $||\ln(\rho_1/\rho_2)||_1 < \epsilon/2$, then $|eH(x)| < \epsilon$,for $\epsilon > 0$.*

Proof. Let $H_1(x) = -\int \rho_1(x) \ln \rho_1(x) dx$ and $\hat{H}_1(x) = -\int \rho_2(x) \ln \rho_2(x) dx$ are the entropies of i.i.d source X with probability distribution $\rho_1(x)$ and empirical distribution $\rho_2(x)$.

69

(a) Baseline - Lateral direction (b) Baseline - Vertical direction

(c) Damage 1 - Lateral direction (d) Damage 1 - Vertical direction

(e) Damage 2 - Lateral direction (f) Damage 2 - Vertical direction
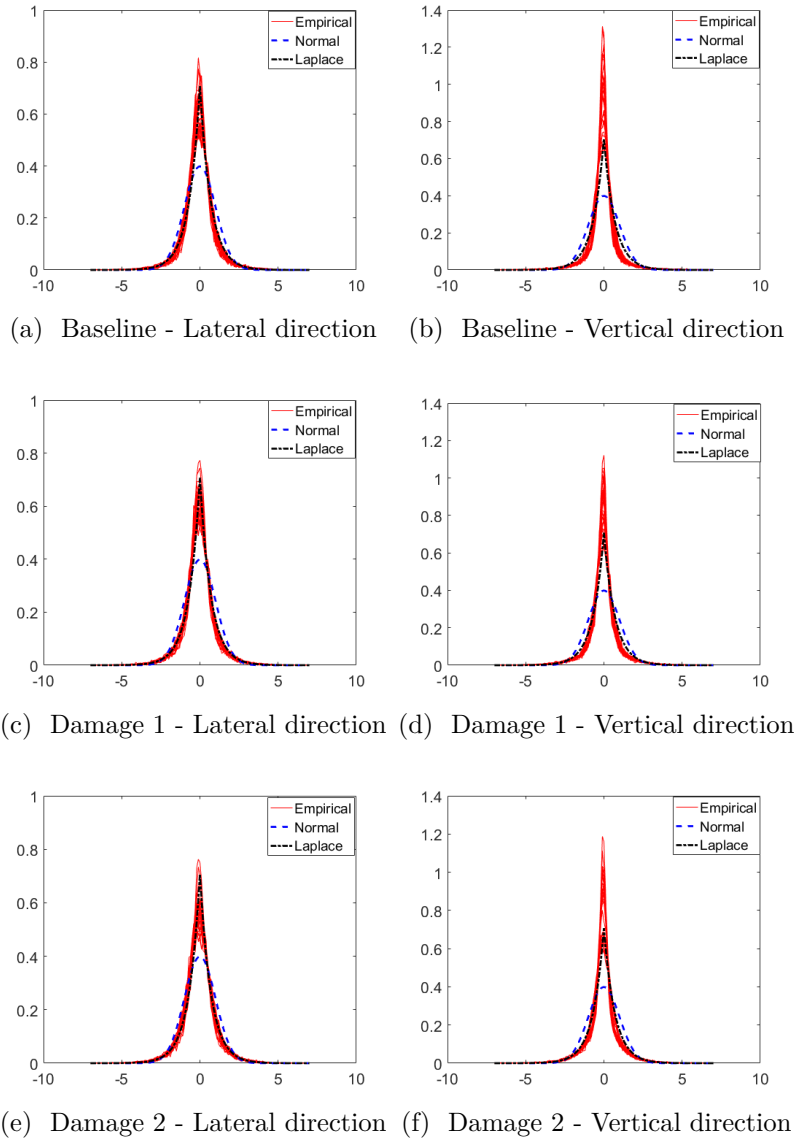
Figure 4.3: Probability distributions of the sensor time series after first pass of the truck. (a) Baseline-lateral, (b) Baseline-vertical, (c) Damage 1-lateral, (d) Damage 1-vertical, (e) Damage 2-lateral, (f) Damage 2-vertical. In all panels we also plot the normal distribution and the Laplace distribution for visual comparison. All distributions have been standardized to have zero mean and unit variance.

Consider

$$|eH(x)| = |H_1(x) - \hat{H}_1(x)|$$

$$= |\int (\rho_1(x) \ln \rho_1(x) - \rho_2(x) \ln \rho_2(x)) \, dx|$$

$$\leq ||\rho_1(x) \ln \rho_1(x) - \rho_2(x) \ln \rho_2(x)||_1$$

$$\leq ||\rho_1(x) \ln \rho_1(x) + \rho_1(x) \ln \rho_2(x) - \rho_1(x) \ln \rho_2(x) - \rho_2(x) \ln \rho_2(x)||_1$$

$$\leq ||\rho_1(x) (\ln \rho_1(x) - \ln \rho_2(x) + (\rho_1(x) - \rho_2(x) \ln \rho_2(x)||_1$$

$$\leq ||\rho_1(x) (\ln \rho_1(x) - \ln \rho_2(x)||_1 + ||\rho_1(x) - \rho_2(x) \ln \rho_2(x)||_1 \quad \text{(By Minkowski inequality)}$$

$$\leq ||\rho_1(x)||_1 ||(\ln \rho_1(x) - \ln \rho_2(x)||_1 + ||\rho_1(x) - \rho_2(x)||_1 || \ln \rho_2(x)||_1 \quad \text{(By Young's inequality)}$$

$$\leq ||(\ln \rho_1(x) - \ln \rho_2(x)||_1 + ||\rho_1(x) - \rho_2(x)||_1 || \ln \rho_2(x)||_1 \quad \text{(Since} ||\rho_1(x)||_1 = 1)$$

$$(4.3)$$

1. (Trivial case)

   If $\rho_1(x) = \rho_2(x)$

   $\Rightarrow \rho_1(x)/\rho_2(x) = 1$

   taking the natural logarithmic of both sides, $\ln(\rho_1/\rho_2) = 0$ and $\Rightarrow |eH(x)| \leq 0$.

   Since $|eH(x)| > 0$, $\Rightarrow |eH(x)| = 0$

2. If $||\rho_1(x) - \rho_2(x)||_1 < \epsilon/2M$ and $|| \ln \rho_2(x)||_1 < M$,

$$||\rho_1(x) - \rho_2(x)||_1 || \ln \rho_2(x)||_1 < \epsilon/2 \qquad (4.4)$$

   Since

$$|| \ln \rho_1(x) - \ln \rho_2(x)||_1 < \epsilon/2 \qquad (4.5)$$

   by 4.4

   $|eH(x)| \leq \epsilon$ for $\epsilon > 0$.

71

□

4.4 Results

4.4.1 Parametric Entropy Estimator for Multivariate Laplace Distribution

In the previous section we established that the lateral and vertical accelerations recorded by the bridge sensors more closely follow Laplace distributions rather than normal distributions. Assuming a parametric estimator for entropy generally requires fewer data points for the same level accuracy. On the other hand, the non-parametric approaches where no prior assumption on the form of the underlying distribution can be used to calculate information measures. However, non-parametric based estimators do not guarantee accuracy [118]. Thus parametric estimators for information measures based on the Laplace distributions are used for more accurate results.

If the underlying data follows a normal distribution, there is a parameter estimator based on a closed-form formula that only involves the variance (and covariance for multivariate data) of the time series. However, no such closed-form formula exists for the Laplace distribution. Our strategy is to use a Monte Carlo method to numerically evaluate the integrals which define entropies and mutual information, where the pdf in the integrals are assumed to be Laplace distributions whose covariances are directly estimated from data. Since there are multiple variables involved, the assumed distribution is a multivariate Laplace distribution whose pdf is given by [119]

$$f_X\left(\mathbf{x}\right) = \frac{1}{2\pi^{(d/2)}} \frac{2}{\lambda} \frac{K_{(d/2)-1}\left(\sqrt{\frac{2}{\lambda}q(\mathbf{x})}\right)}{\left(\sqrt{\frac{\lambda}{2}q(\mathbf{x})}\right)^{(d/2)-1}}, \tag{4.6}$$

where $\mathbf{x} \in \mathbb{R}^d$, $K_{(d/2)-1}$ is the modified Bessel function of the second kind with order

(a) Baseline - Lateral direction

(b) Baseline - Vertical direction

(c) Damage 1 - Lateral direction

(d) Damage 1 - Vertical direction

(e) Damage 2 - Lateral direction

(f) Damage 2 - Vertical direction
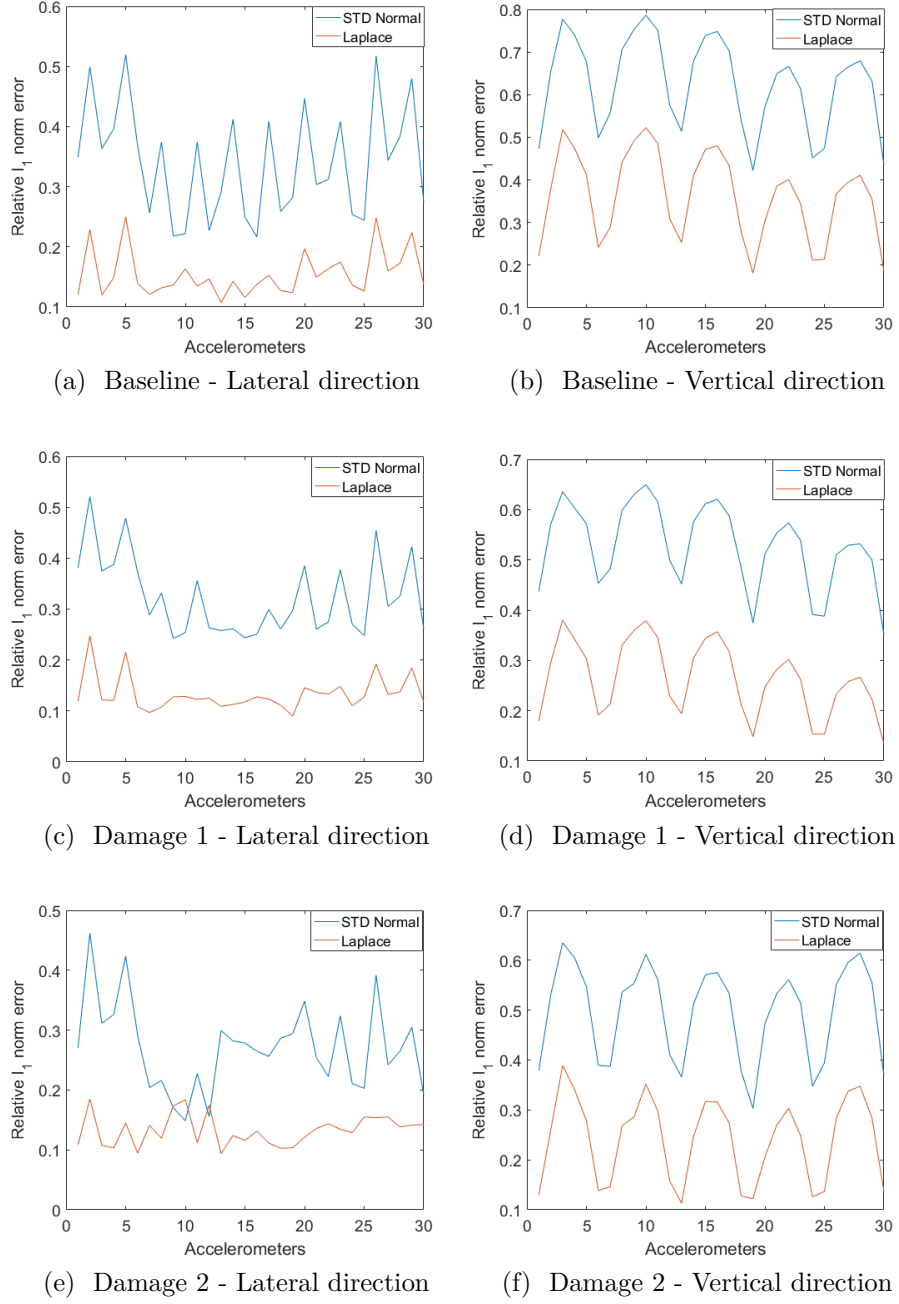
Figure 4.4: Relative l_1 - norm error of the probability distributions of the sensor time series after first pass of the truck. Here relative l_1 - norm error is defined by $||p_1 - p_2||/||p_1||$, where p_1 is the empirical distribution and p_2 is either standard normal or Laplace distribution. (a) Baseline-lateral, (b) Baseline-vertical, (c) Damage 1-lateral, (d) Damage 1-vertical, (e) Damage 2-lateral, (f) Damage 2-vertical. In all panels the distribution error is computed against either a standard normal or a Laplace distribution.

$(d/2) - 1$ evaluated at $\mathbf{x}$,

$$q(\mathbf{x}) = \lambda \left(\mathbf{x} - \mu\right)^{\top} \Sigma^{-1} \left(\mathbf{x} - \mu\right), \tag{4.7}$$

μ is the mean vector, Σ is the covariance matrix and $\lambda = \sqrt{\det(\Sigma)}$.

4.4.2   Spatial Pairwise MI - Baseline, Damage 1, Damage 2

This section illustrates use of pairwise mutual information to study the damage detection of the bridge. Bridge layout has 30 accelerometers. Each accelerometer records time series data for vertical and lateral directions, each. We use the spatial pairwise mutual informations as a probe to study the difference between healthy bridge structure and damaged bridge structures. In particular, for each sensor, we compute the MI between the time series produced by it and each of its 4 spatially nearest neighbors. All the results here are shown only for the scenarios that we call, baseline, damage 1, damage 2 after the first pass of the truck (tests 1, 4, 7 in Table 4.1). Fig. 4.5 shows the estimated pairwise mutual information of the lateral-direction accelerometer for the first pass of the truck in both directions. In particular, Fig. 4.5(a) describes the mutual interactions for baseline, which is referred as the healthy bridge. Here pairwise mutual informations are drawn as thickness of the line proportional to the pairwise mutual information. Maximum pairwise mutual information is shown between accelerometers 28-29, 26-27. Interactions are less than 0.108 between accelerometer 9-10 and 15-16. Fig. 4.5(b) describes the mutual interactions for damaged bridge, which is referred as the first damage of study of the bridge. Notice that, first damage study was done by removing 4 bolts (out of 6) from the first diaphragm. We can see that after the first damage, interactions remain in the same range for almost all the accelerometers. However, there is a loss of MI between 10-11 and 8-9, which can be identified clearly in Fig. 4.7. Further damage to the bridge in the tests was

done by removing all 6 bolts from first diaphragm, with the resulting pairwise mutual information shown in Fig. 4.5(c). Similar plots are shown with respect to the vertical accelerations in Fig. 4.6.

(a) MI-Baseline-Lateral   (b) MI-Damage1-Lateral   (c) MI-Damage2-Lateral

Figure 4.5: Pairwise mutual information between accelerometers in the lateral direction after first pass of the truck. Fig. (a) healthy bridge (b) Damaged bridge after removing 4 bolts of six bolts (c) Damaged bridge after removing all 6 bolts from the first diaphragm. There is a significant loss of mutual information in both damaged bridges compares with healthy bridge.

To more clearly illustrate the difference in information association between nearby spatial sites, we further plot the difference of spatial pairwise mutual information between the healthy bridge and damaged bridges, as shown in Fig. 4.7 (lateral direction) and Fig. 4.8 (vertical direction). In these figures, red and blue are used to respectively denote negative and positive changes due to the damage. Several observations are in order. First, (with very few exceptions) damage to the structure (as achieved by the removal of bolts in the tests) seems to generally lower the value of mutual information in the lateral direction between spatially nearby sites, indicating a lower coupling, and such change is enhanced with further structural damage [Fig. 4.7].

Secondly, some difference in connection strengths can be seen in the both Fig. 4.7 and Fig. 4.8. For example in Fig. 4.7(a) 11-12, 10-11, 8-9, 7-8 and in Fig. 4.8(a) 11-12, 10-11, 8-9, 16-17. Same mutual interaction strength differences between the above
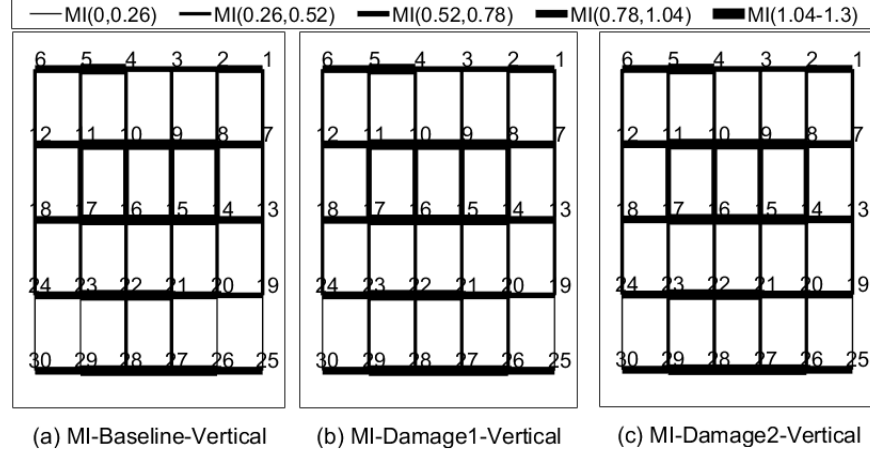
Figure 4.6: Pairwise mutual information between accelerometers in the vertical direction after first pass of the truck. Fig. (a) healthy bridge (b) damaged bridge after removing 4 bolts of six bolts (c) damaged bridge after removing all 6 bolts from the first diaphragm.

mentioned accelerometers can be seen in Fig. 4.7 (b) and Fig. 4.8(b), which describes the differences in information flow between the healthy bridge and the bridge after second damage in the lateral and vertical directions, respectively. However, some connections remain the same as measured by the spatially pairwise MI. Ex: see the connection 9-15 in the lateral direction [Fig. 4.7] and the connection 1-7 in the vertical direction [Fig. 4.8].

4.4.3 oMII - Baseline, Damage 1, Damage 2

In the previous section we use spatial pairwise MI to study damage detection of the bridge structure. However, pairwise mutual information itself cannot differentiate between direct and indirect couplings or select the most influential pairs among all possible couplings. The oMII connections by contrast identify direct influences, whether they be spatially nearest neighbors or more remote sites on the bridge structure. It is particularly valuable in a damage detection scenario where oMII connections may be especially fragile to changes in the structure. Applying the oMII algorithm as described in Section 4.2.2 to the lateral time series with parameters $\theta = 0.1$ for
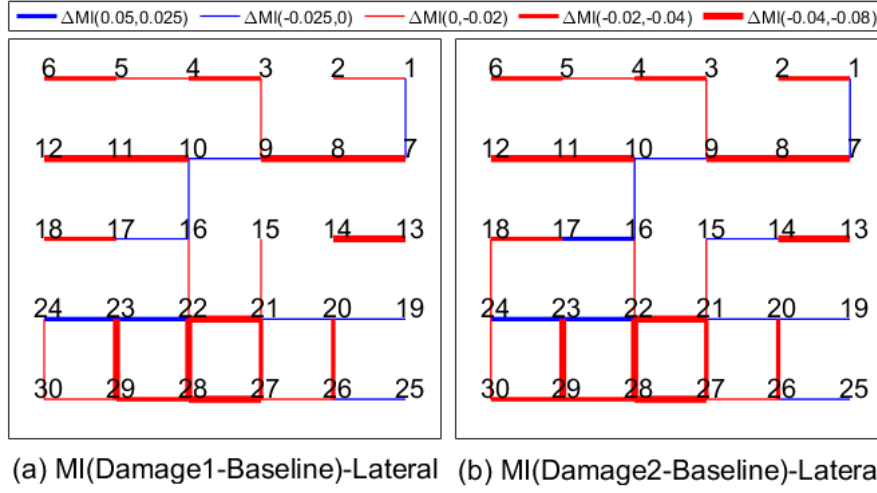
Figure 4.7: Difference of the pairwise mutual information between accelerometers in the lateral direction after 1st pass of the truck. (a) difference of healthy bridge and bridge after first damage (b) difference of healthy bridge and bridge after second damage. There is some difference of connection strengths after first damage and second damage.
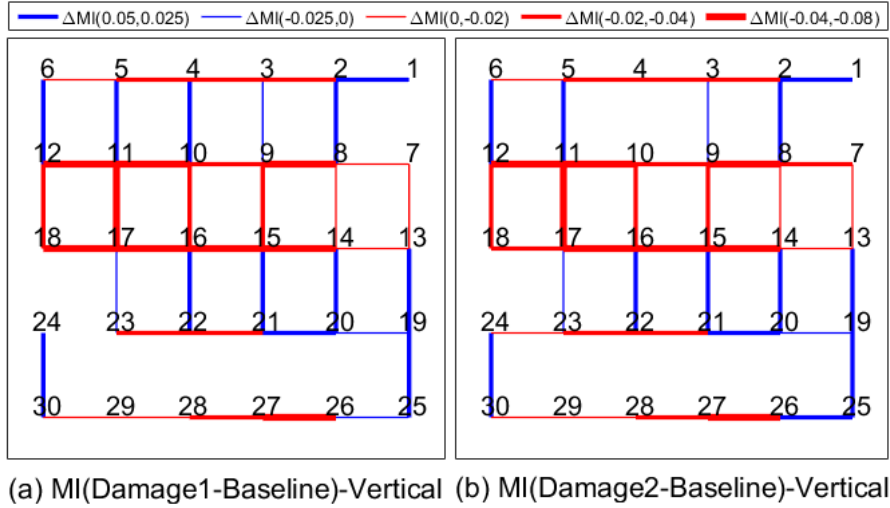
Figure 4.8: Difference of the pairwise mutual information between accelerometers in the vertical direction after 1st pass of the truck. (a) difference of healthy bridge and bridge after first damage (b) difference of healthy bridge and bridge after second damage. There is some difference of connection strengths after first damage and second damage in the vertical direction.

the stopping criteria and $N_s = 100$ in the shuffle test, we show the resulting oMII connections in Fig. 4.9 and Fig. 4.10 for lateral and vertical directions.

Figure 4.9 (a) shows the oMII interactions for the healthy bridge. It can be seen from the figure that the bridge structure supports more information flow in the same direction as the truck lanes (horizontal direction in the figure). Exceptions are near the center of the bridge which could have been due to the first diaphragm placed in the bridge structure (see Fig. 4.2(b)). The oMII interactions after the first damage (removal of 4 out of 6 bolts) and second damage (removal of all 6 bolts) are shown in Fig. 4.9(b-c). After the first damage, we can see there is both a loss of oMII connections and new ones. This indicates that the loosening of the bridge potentially allows for new pathways for vibrational signals to propagate. Clear change in the information flow in the center of the bridge can be seen from the Fig. 4.10. However, in the vertical axis also bridge structure supports more information flow in the same direction as the truck lanes.

To more clearly see which oMII connections are lost/created after damage, we plot the difference of the oMII connections between the healthy bridge and the damaged bridges in Fig. 4.11(a) (healthy vs. first damage) in lateral direction, Fig. 4.11(b) (healthy vs. second damage) in lateral direction, 4.12(a) (healthy vs. first damage) in vertical direction, and Fig. 4.12(b) (healthy vs. second damage) in vertical direction, respectively. In these figures, the lost connections are shown as dashed red lines and the new ones are illustrated by solid black lines. Directionality is denoted by arrows. One can see that there are 10 new connections (solid black lines) and 7 loss connections (dashed red lines) appear after the first damage in Fig. 4.11(a).

Due to the second damage, we can see there are significant changes in the information transfer between sensors. 10 new connections are occurred and 16 connections are lost after the second damage (see 4.11(b)). We can see from the 4.12(a) and 4.12(b) that the number of changes of connections in the vertical direction and lat-

(a) Baseline
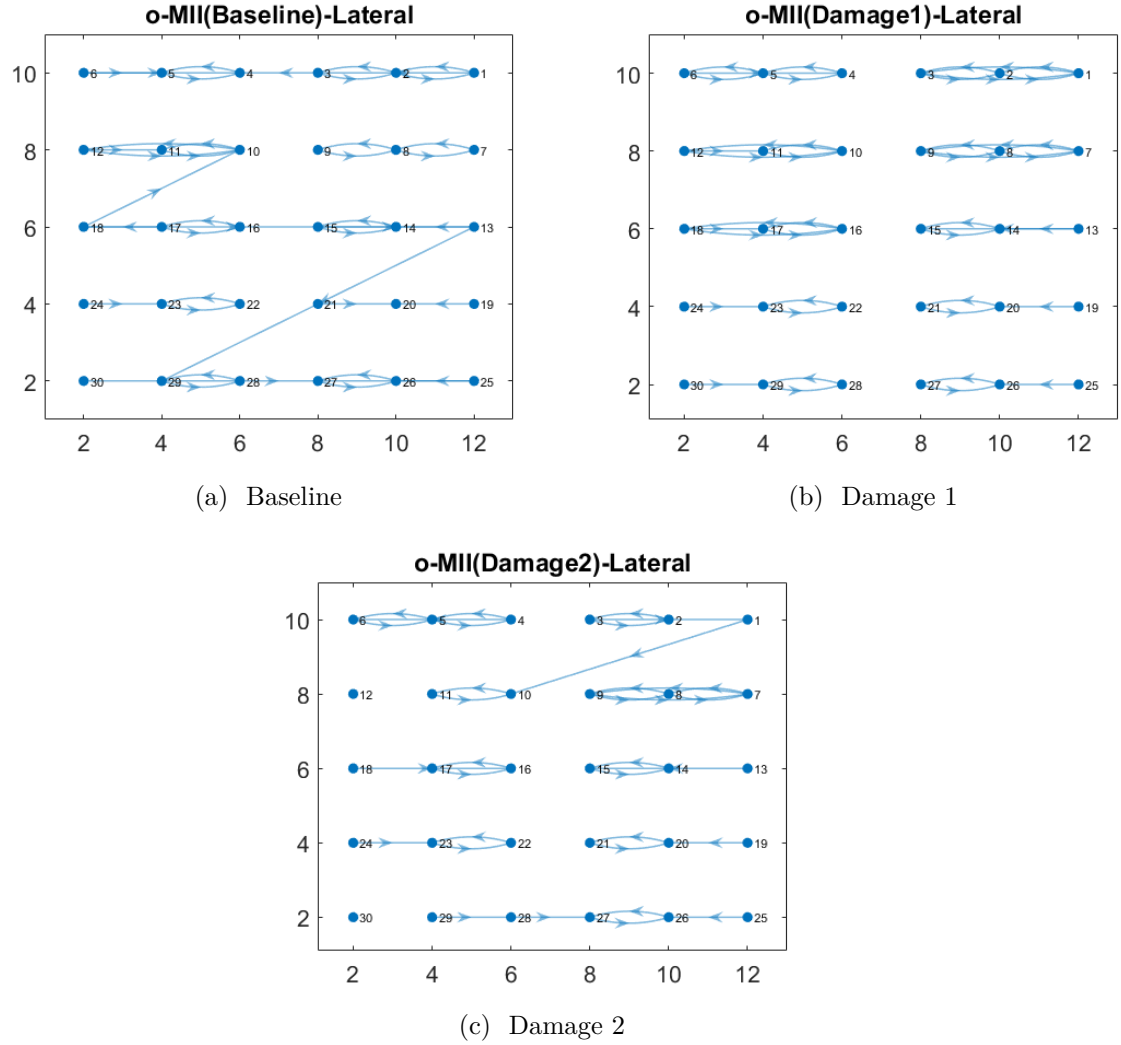
(b) Damage 1

(c) Damage 2

Figure 4.9: oMII interaction between accelerometers in the lateral direction after first pass of the truck. Fig. (a) healthy bridge (b) damaged bridge after removing four bolts from 6 bolts (c) damaged bridge after removing all the 6 bolts from the first diaphragm.
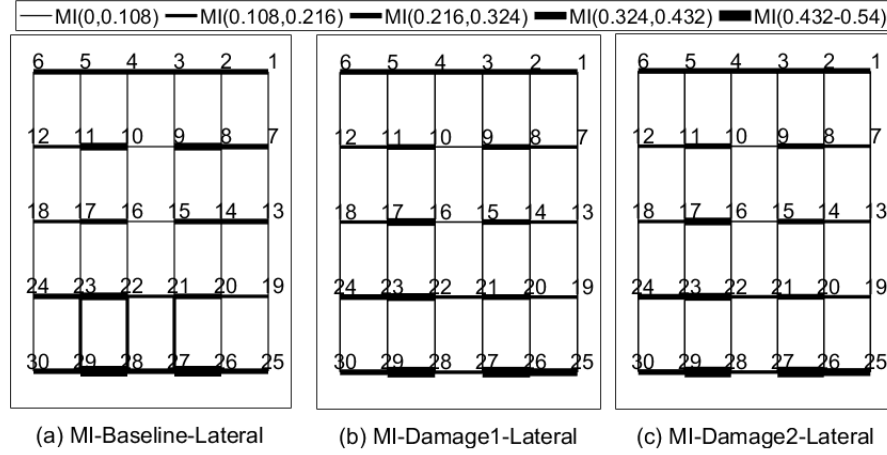
(a) Baseline
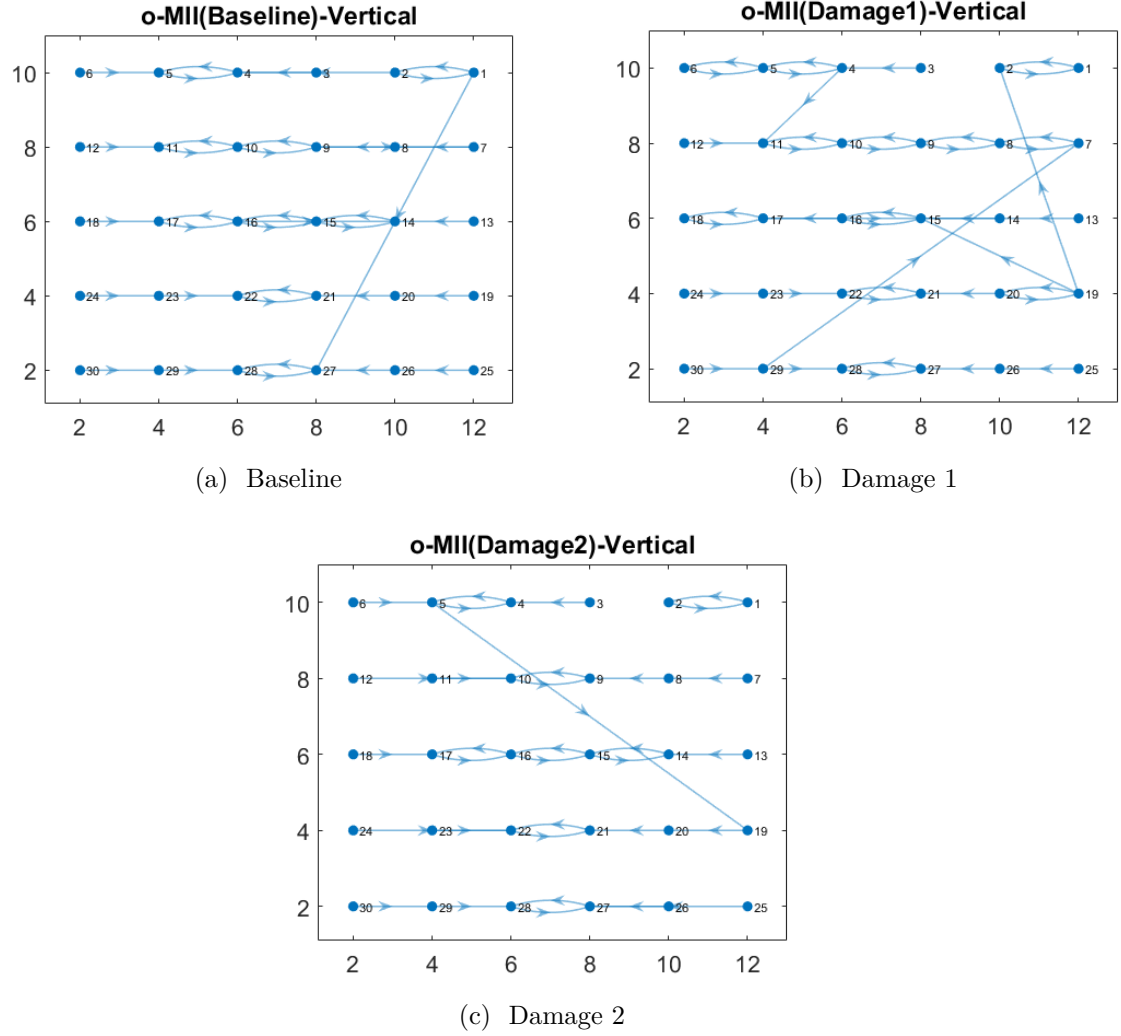
(b) Damage 1

(c) Damage 2

Figure 4.10: oMII interaction between accelerometers in the vertical direction after first pass of the truck. Fig.(a) healthy bridge (b) damaged bridge after removing four bolts from 6 bolts (c) damaged bridge after removing all the 6 bolts from the first diaphragm.

(a) Baseline - Damage 1　　　　　　　(b) Baseline - Damage 2
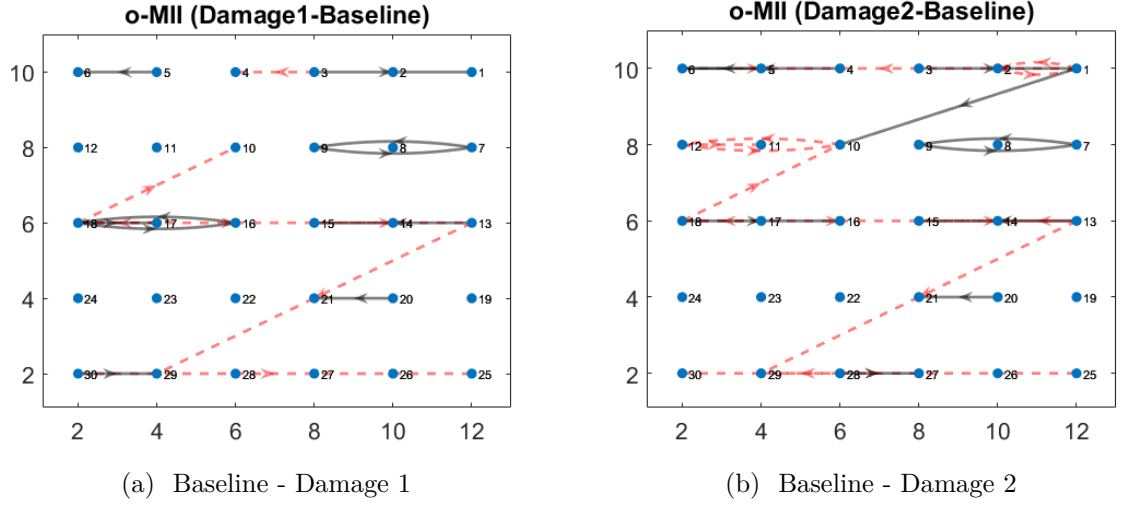
Figure 4.11: Difference of the oMII between baseline and damaged bridges in the lateral direction after 1st pass of the truck. (a) difference of healthy bridge and bridge after first damage (b) difference of healthy bridge and bridge after second damage. Red and black lines represent new connections and loss connections after damaged the bridge respectively.

eral direction remain same after the first damage. After the second damage, number of new and loss connections (so number of changes) have decreased in the vertical direction. However, the number of changes in the connections have increased in the lateral direction.

The results obtained by oMII as plotted in Fig. 4.11 and Fig. 4.12 show that for the vertical "gap" in the middle of the region which corresponds to where the diaphragm connections are, new connections are formed after damages are introduced. Interestingly, this pattern only appears for the lateral accelerations but not the vertical ones.

Another way to characterize the results is to look at degree distribution of outgoing and incoming links. The degree distribution (outgoing and incoming links) in the baseline and damaged bridge is shown in the Fig. 4.13. Yellow, cyan, and black bars represent the baseline, damage 1, damage 2 respectively. For some bridge systems, there are some sensors that do not have outgoing or incoming links. The maximum
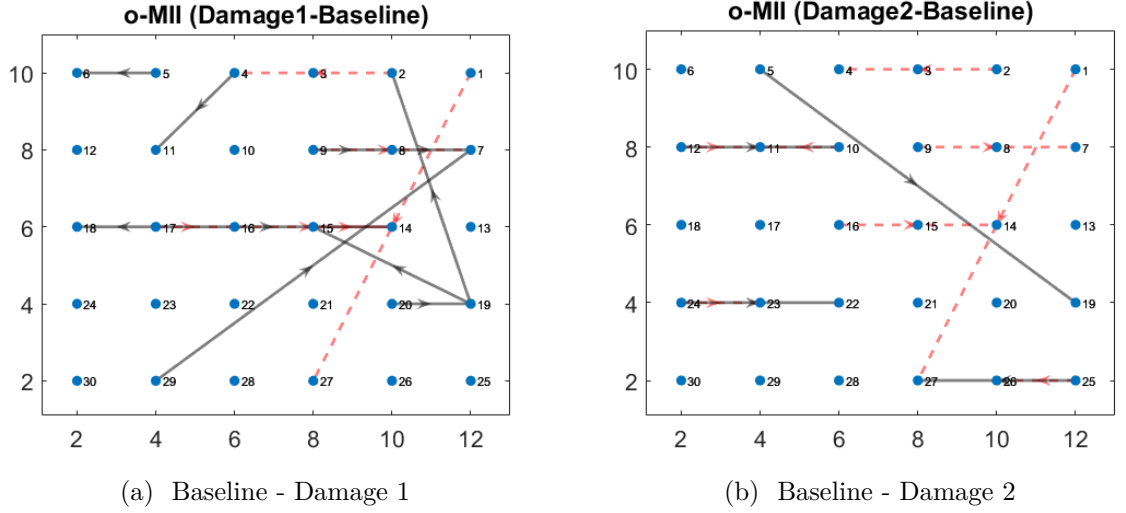
Figure 4.12: Difference of the oMII between baseline and damaged bridges in the vertical direction after 1st pass of the truck. (a) difference of healthy bridge and bridge after first damage (b) difference of healthy bridge and bridge after second damage. Red and black lines represent new connections and loss connections after damaged the bridge respectively.

amount of outgoing and incoming link is 3 for all structures. In both the lateral and vertical directions, both the probability of having no incoming links and the probability of having no outgoing links have increased after damage 2 (as compared to the healthy bridge). This implies that after introducing relatively large damage to the bridge there is a significant number of locations that become "disconnected" from the rest of the bridge in terms of information flow.

In summary, we observe that there are both vanishing and new direct connections between sensors as the damage experiment is progressed (Fig. 4.13), inferred as direct connections of the accelerometer signals by vibrational transmission of energy, and furthermore the sensed values are stable across the repeated experiment. Therefore, we have described a simple experimental protocol, driving a truck over a bridge with instrumentation, and a information theoretic way to interpret the data, that is positively indicative of the damage.

(a) Degree distribution - Lateral   (b) Degree distribution - Vertical
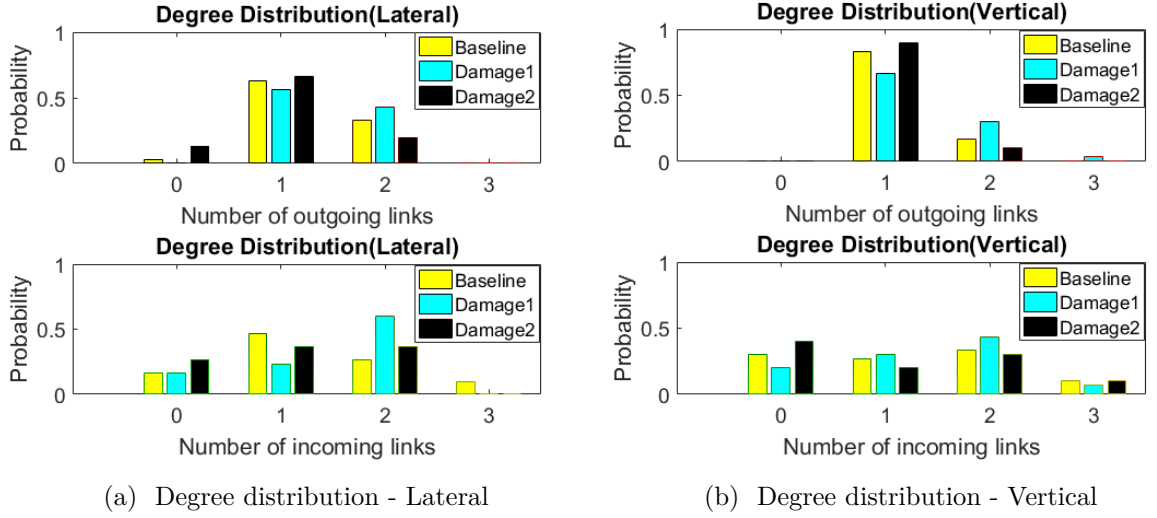
Figure 4.13: Degree distribution of the oMII between baseline and damaged bridge after 1st pass of the truck in the (a) lateral direction (b) vertical direction. 0, 1, 2, 3 are the number of outgoing and incoming links.

4.5 Discussion and Conclusion

In this work, we used an MI based approach to study damage detection of a bridge located in Waddington, New York. The damage to the bridge was introduced by removing bolts from the first diaphragm of the bridge and a sequence of tests were performed with time series data collected on various locations on the bridge. In particular, comparing to the baseline case where no damage was introduced, two levels of damage were tested by either removing four out of the six bolts (damage 1) or all six bolts (damage 2).

Our first finding is that the measured data, which are accelerations detected by sensors on the bridge, more closely follow Laplace distribution than normal distribution. This enables us to develop parametric estimators of mutual information and conditional mutual information that are more efficient than non-parametric ones.

Our second finding is that the spatial nearest-neighbor interactions as measured by mutual information tend to become weaker as more damage is imposed. This is consistent with the intuition that less force and energy pass between adjacent sites

as the bridge is "loosened" due to the removal of bolts.

Finally, we found that the more primary direction of direct influence and information flow as detected by oMII goes in the direction of traffic flow even after partial damage to the bridge. Based on the particular experiments from which these results are obtained, it is not yet clear whether such unidirectional dominance of information flow comes from the underlying mechanical structure or from the effect of drive-through by the trucks.

Among the many unsolved problems, we note that it is important to design experiments for which results from noninvasive damage detection techniques such as the ones investigated herein can be experimentally validated. The success of such validation is necessary for making reliable assessment of the structural fatigue as well as the risk of sudden and disastrous collapse of bridges.

Chapter 5

Sinkhole Detection using Full Waveform Inversion

5.1   Introduction

Anomalies such as voids in soils cause significant structural damage. When a void weakens support of the overlying earth, ground-surface depressions occur. Such a depression formed as a result of collapse is called sinkhole. Sinkholes can occur naturally or by manmade activities. Natural sinkholes occur when rocks, such as limestone, dolomite, carbonate rock, or salt beds below the land surface dissolve to create underground cavities. Hydraulic conditions such as excessive rainfall in a short period of time and lack of rainfall can also lead to sinkhole development [120]. On the other hand, humans are also responsible for sinkholes. Manmade activities such as mining, drilling, and construction can result in sinkholes [121]. Figure 5.1(a) and (b) illustrate the development process of a sinkhole by natural and human-made activities.

1. Water percolating into bedrock near ground level slowly erodes soluble rock such as limestone or dolomite, creating small cavities.
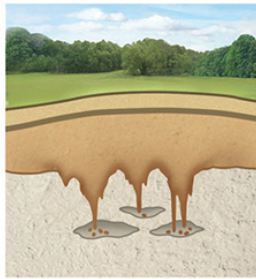
2. The soil on top of the bedrock, known as overburden, is composed largely of sand, silt or clay. In a process called suffosion, it starts to fall into cavities in the bedrock.

3. As this soil fills spaces in the bedrock below, a new cavity forms in the overburden, expanding toward the surface.

4. In weak soil, the cavity grows quickly in the shape of a funnel. In stiffer soil, such as clay, the cavity eventually becomes so large that the remaining overburden can no longer support itself or the weight of objects on the ground above it, and the overburden collapses, creating a sinkhole.

(a)

HUMAN-MADE

1. Infrastructure such as sewer pipes or water mains, located below loose deposits of earth, collapse as a result of erosion or age.
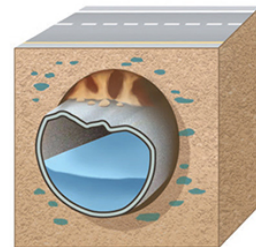
2. The loose earth fills the space created by the collapsed pipe and, in some cases, water from the pipe permeates the ground around it, weakening the surrounding soil.
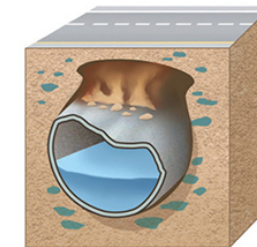
3. A cavity remains above the collapse, and expands upward to the surface.
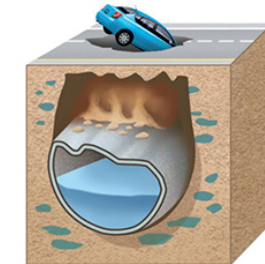
4. If sediments are very loose, a funnel-shaped sinkhole can occur quickly. But if there is a solid layer of material such as asphalt or concrete on the surface, the cavity below can remain concealed even as it grows. Once the weight becomes too much to bear, the cover collapses, and a more dangerous cylindrical sinkhole is formed.

(b)

Figure 5.1: The making of a sinkhole (photo credit: Ref. [16]).

These collapses can result in significant property damage as well as loss of life. For example, in 2013 in Florida, a man was swallowed by a sinkhole that opened beneath the bedroom of his house. This man's remains were never recovered. This sinkhole reopened up in 2015 and is shown in Fig. 5.2. Also, repairing such damaged structures after a collapse is expensive. Thus, understanding the causes of sinkholes has the potential to prevent such expensive structural damage ahead of time.

Figure 5.2: A 15-foot deep sinkhole in Florida that swallowed a man. (photo credit: Ref. [17]).

Geologists have developed many testing methods for health monitoring in the geological sites. Among them, nondestructive testing methods play an important role. There are many nondestructive testing methods available for sinkhole detection in a geological site. Gravity methods [18, 36, 37], electric resistivity methods [38, 39], and seismic methods are some exciting new methods in locating sinkholes.

These methods have advantages and disadvantages in characterizing sinkholes. Gravity methods [18, 36, 37] are based on a density contrast between the material filling the sinkhole and its surroundings. The gravity field on the subsurface is not uniformly distributed everywhere. The strength of the gravity depends on the distribution of the mass of materials below the subsurface. Thus the density property of subsurface materials can be used for sinkhole identification [37]. Figure 5.3 illustrates the relative surface variation of Earth's gravitational acceleration over geological structures. If the void or sinkhole is close to the ground surface, then the void can be located by measuring the gravitational pull across the void. The gravity method is a relatively inexpensive method [18]. However, if the depth from the free surface to the void is greater than the size of the sinkhole, accurate predictions cannot be made from the measured data [42].
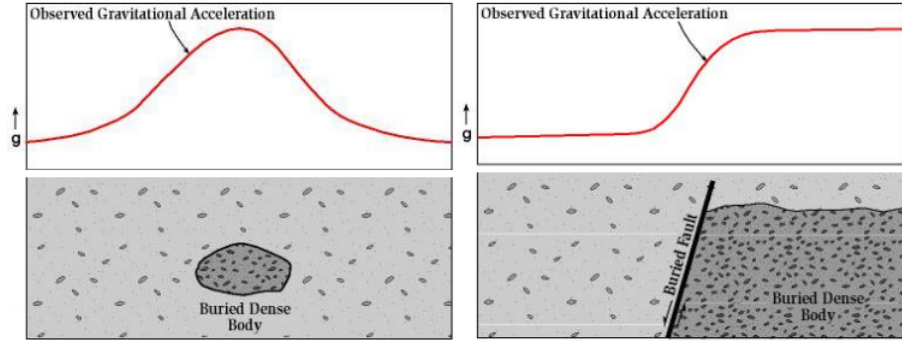
Figure 5.3: The relative variation of Earth's gravitational acceleration over geologic structures (photo credit: [18]).

Resistivity methods [38, 39] are another technique for solving the sinkhole problem. These methods involve the measurements of the apparent resistivity of soils and rocks. Resistivity methods utilize direct currents or low frequency alternating currents to investigate the resistivity of the subsurface. One of the advantages of these methods is that resistivity methods are relatively easy to perform in difficult field conditions. But, like gravitational methods, the approach is only applicable for finding shallow voids [42].

Full seismic surface wave fields can also be used to identify and quantify embedded sinkholes. This method can be used to characterize variable soil/rock layers, as the propagation properties of seismic waves are modulated by the anomalies and layer interfaces [42]. The seismic waves can be divided into two categories according to the wave propagation in a medium; body waves and surface waves. Body waves propagate in the interior of a medium. There are two main types of elastic body waves; longitudinal waves (P-wave or primary wave) and shear waves (S-wave or secondary wave). P-waves generate compression particle motion parallel to the direction of propagation–also known as compressional waves–and may be transmitted through solid rock and fluids. S-waves generate particle motion perpendicular to the direction of propagation. S-waves are slower than P-waves and cannot move through a liquid medium. The surface waves propagate in a shallow zone near a free surface. Surface

waves have a lower frequency than body waves.

In the seismic wave method, ground vibrations are incurred by striking a hammer against a metal plate, producing seismic waves which emanate from the source (see Fig. 5.4). These waves are detected and the arrival time is recorded by the geophone, which is placed on the ground along the direction of the seismic wave propagation. Then, using the arrival time, ground properties such as wave velocities are determined. Some of the popular seismic wave methods are surface wave methods and borehole methods.

The surface wave method (SWM) is a seismic characterization method based on the analysis of the geometric dispersion of surface waves [122]. Surface waves travel parallel to the surface or near the surface. They are characterized by low velocity, low frequency, and relatively high amplitude. Surface waves with different frequencies travel at different velocities. They are easily generated by both active (hammer and plate, weight drop) and passive (micro-tremors) sources. One of the limitations of SWM is that the result is one-dimensional as the assumed model is one dimensional [122]. i.e. the surface model assumes it does not include lateral changes in velocity and layer geometry [123].
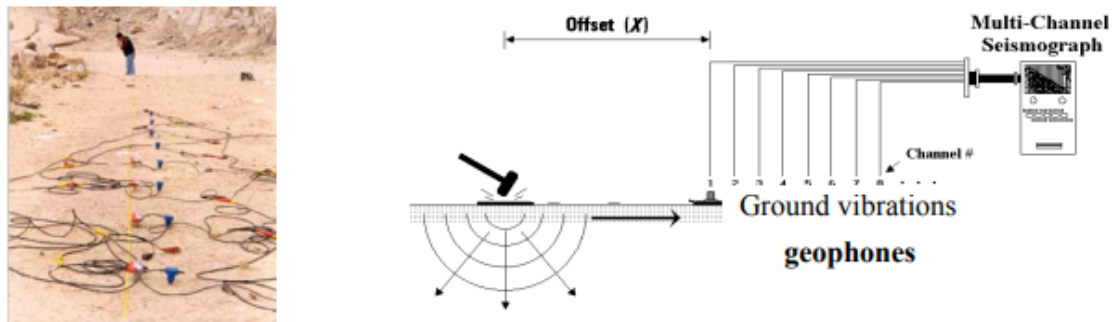
Figure 5.4: A field layout of seismic survey. Here the multi-channel seismograph is built-in with internal computer geophones (photo credit: [19])

There are two types of borehole methods; downhole seismic testing and cross-holes seismic testing. In downhole testing technique, a source is placed at the top of a bore-

hole and vertical changes in seismic velocity are measured. Using geophones, travel times at multiple intervals in the borehole can be measured. In cross-hole (or "cross-well") seismic testing, the velocity of seismic waves between boreholes is measured. In the conventional approach, a 3-component borehole geophone is lowered down one hole and a source is lowering down an adjacent hole(s) by firing the source at some prescribed depth interval. Figure 5.5 illustrates the field layout of the conventional cross-hole method. The source and geophones are always at the same elevation. In each receiver hole, the energy from each shot is measured at a single depth. Velocities are found by dividing the travel times by the distance between the holes [20].
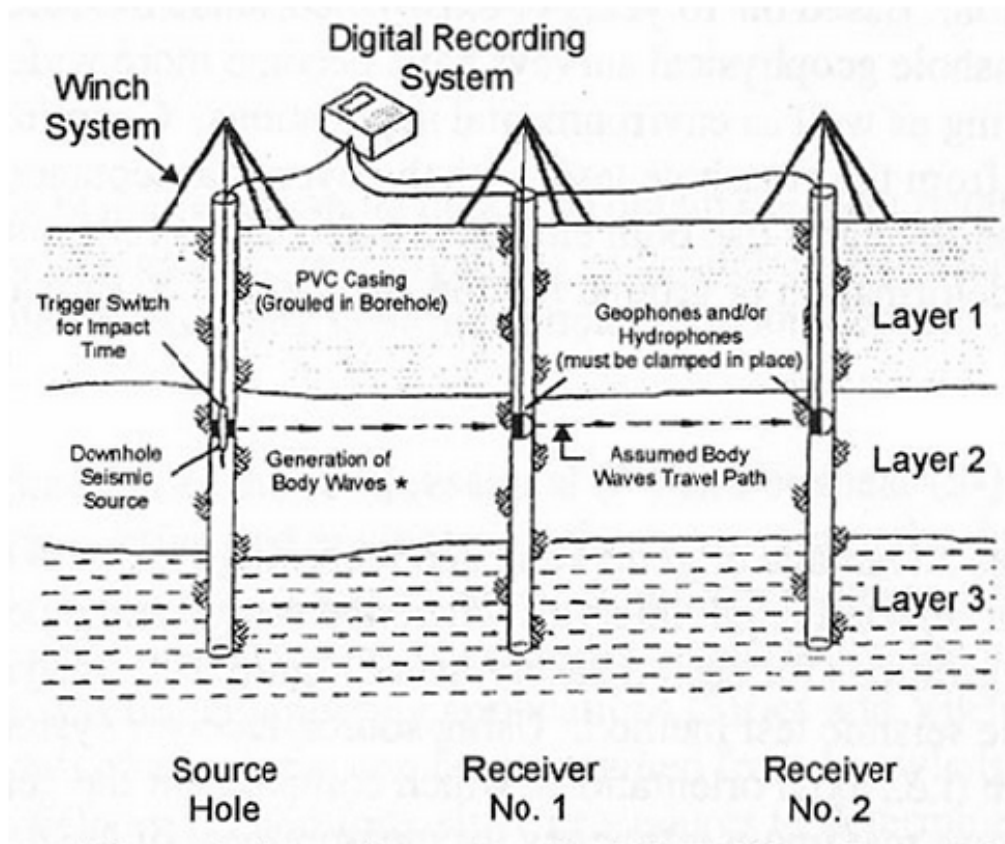
Figure 5.5: A field layout of cross-hole seismic testing (photo credit: [20])

The full-waveform inversion (FWI) approach [40, 41] is another approach that offers the potential to produce higher resolution imaging of the subsurface by extracting

information contained in the complete waveforms [42]. This approach can be determined the properties of the subsurface from seismic data (wavefield data) obtained at receivers, which are placed on the subsurface. The FWI approach can be illustrated using the workflow given in Fig. 5.6.
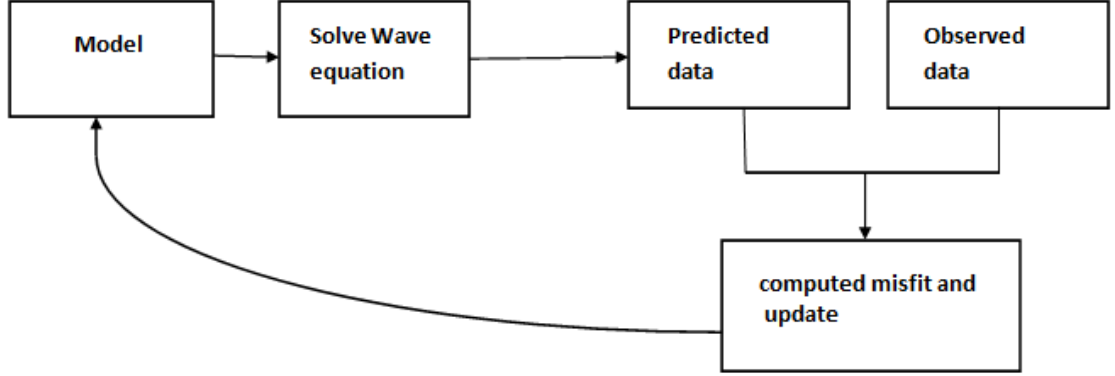
Figure 5.6: Illustration of FWI method

The model we consider is an initial guess based a known properties of the subsurface. The model's results (wavefield data) are solved wave equations assuming an elastic media producing "predicted data". Simultaneously, wavefield data is observed experimentally at the receivers, which are placed on the surface. Then the difference between the predicted data and the observed data are minimized to obtain properties of the subsurface. The model is updated iteratively until the residual is sufficiently small.

In the FWI approach, the process of estimating wavefield by solving wave equations at known model parameters is known as the forward problem. If M is the model space (or parameter space) and D is the data (wave field) space, then the forward model $F : M \to D$ can be defined by

$$F\left(\mathbf{m}\right) = \mathbf{d}, \tag{5.1}$$

where $\mathbf{m} \in M$ is the model parameters that represent the subsurface. For example, in the acoustic case, the model parameters are the P-wave velocities, S-wave velocities, density, and Lame coefficients defined at each cell of the numerical mesh used in the forward simulations. $\mathbf{d} \in D$ represents seismic responses of the surface recorded at the receivers. F is the corresponding modeling operator, which is specified by the equation of motion and boundary conditions.

Finding $\mathbf{m}$ by seeking the minimum of the residuals between the model responses obtained by simulation of wave equations and the observed seismic data is known as the inverse problem. The residual can be defined as

$$\Delta \mathbf{d} = \mathbf{d}_{\text{est}}\left(\mathbf{m}\right) - \mathbf{d}_{\text{obs}} \tag{5.2}$$

where $\mathbf{d}_{\text{est}}$ is the estimated data associated with the model parameters m and $\mathbf{d}_{\text{obs}}$ is observed data. The inverse problem is called well-posed if there is a unique and continuous solution to the problem with a small perturbation of responses $\mathbf{d}$. Otherwise, the problem is called ill-posed. One of the common approaches to ensuring the well-posedness is to regularize the ill-posed problem. By regularizing the problem, one can obtain a unique and consistent solution to the problem. We present more mathematical details of the inverse problem and the regularization in Section 5.4.

In the literature, many waveform inversion algorithms were developed for application in large-scale (kilometer-scale) domains [124–129]. For example, a frequency domain method to carry out the inversion with discrete space-frequencies is presented in Ref. [124]. That method allows a significant reduction in computational time by selecting a few frequencies. In general, in the large scale problems, the surface waves can be well separated and removed from body waves prior to the inversion process. However, in small-scale (meter or millimeter scales), separation of the body waves from the surface is difficult [42]. In the literature, only a few studies of waveform

inversion involving body and surface waves have been performed for near-surface investigations on synthetic data at meter scales [130, 131] or real laboratory data at millimeter scales [42].

Recently, Ref. [21] developed an FWI technique which inverted body and surface waves in the case of real experimental data. This approach uses a Gauss-Newton technique to invert the full seismic wave-fields of near-surface velocity profiles by matching the observed and computed waveforms in the time domain. Virtual sources and a reciprocity principle are used to calculate partial derivative wave-fields (gradient matrix) to reduce the computing time.

The Gauss Newton method consists of the computation of Jacobian matrix, which records the partial derrivatives of the seismic data. One of the drawbacks of the Gauss-Newton method is a large memory requirement to store the Jacobian matrix [21, 132–134].

In the literature, several techniques were used to reduce the memory usage for the Jacobian matrix [132–134]. For example, Ref. [132] used a non-linear conjugate gradient method for seismic wave inversion as it does not require the inversion of the dense Hessian matrix. However, the convergence rate of the results may be slow with the conjugate gradient method and not efficient for the problems with more parameters.

Ref. [133] proposed Gauss-Newton-Krylov based method, which is a matrix-free implementation of the Gauss-Newton method for full-wave inversion problems. The authors in Ref. [133] showed that this approach is well suited for a nonlinear and ill-conditioned problem such as inverse wave propagation.

A compressed implicit Jacobian scheme for 3D electromagnetic data inversion was proposed in Ref. [134]. A significant reduction in memory usage for the Jacobian matrix is obtained with the implicit Jacobian scheme for reconstructing electromagnetic data.

We introduce a different cell size based technique as an option for the Jacobian matrix storage. The goal is to address the computational efficiency and the memory requirements of the developed method in Ref. [21]. The difference cell size based technique is applied to a synthetic model and compared with the Gauss-Newton inversion regular method, which is developed in Ref. [21].

The rest of the chapter is organized as follows. The derivation of the wave propagation equations in elastic media is presented in Section 5.2. We present the Full-wave inversion method, which was introduced in Ref. [21] in Section 5.3. Mathematical details and illustration of the inverse problem and regularization problem are given in Section 5.4. Section 5.5 presents the different cell size approach. The comparison of the methods and results for a synthetic model are presented in Section 5.6.

5.2   Wave Propagation in Elastic Media

Equations of wave propagation in elastic media are derived by using Newton's Second Law of Motion and Hooke's Law [135]. These equations can be derived by considering the total force applied to a volume element of an elastic media. We consider a volume element V with surface area S. The total force is accounted for by the body force act within the volume element and its surface force field.

$$F_{\text{Total}} = F_{\text{Surface}} + F_{\text{Body}} \tag{5.3}$$

The surface force can be derived from the traction T. The traction vector describes the surface force as a contact force at one point and is defined by

$$\mathbf{T}\left(\mathbf{n}\right) = \lim_{\Delta S \to 0} \left(\frac{\Delta F_{\text{Surface}}}{\Delta S} \right), \tag{5.4}$$

where $\Delta F_{\text{Surface}}$ is the force acting on the volume element with surface ΔS at a point

and $\mathbf{n}$ is normal on the surface element. Thus

$$F_{\text{Surface}} = \int_S \mathbf{T}(\mathbf{n}) \, dS \tag{5.5}$$

The body force F_{Body} can be obtained by considering Newton's second law,

$$F = mg, \tag{5.6}$$

where g is the acceleration due to gravity, m is the mass of the volume element, and density $\rho = \frac{m}{V}$. Thus

$$dF_{\text{Body}} = \rho g dV \tag{5.7}$$

$$F_{\text{Body}} = \int \rho g dV \tag{5.8}$$

The total force is obtained as

$$F_{\text{Total}} = \int_V \rho f dV, \tag{5.9}$$

where f is the local acceleration field given by $f = \frac{\partial^2 \mathbf{u}}{\partial t^2}$. Here $\mathbf{u}$ is the displacement. The traction vector can be calculated using the nine component stress tensor σ.

$$\mathbf{T}(\mathbf{n}) = \sigma \cdot \mathbf{n} \tag{5.10}$$

Therefore, the force balance equation can be written as

$$\int_S \sigma \cdot \mathbf{n} dS + \int_V \rho g dV = \int_V \rho \frac{\partial^2 \mathbf{u}}{\partial t^2} dV \tag{5.11}$$

The divergence theorem is used to transform the volume integral and the surface

95

integral in Eq. 5.11. Then one can obtain

$$\nabla \cdot \sigma + \rho g = \rho \frac{\partial^2 \mathbf{u}}{\partial t^2} \tag{5.12}$$

In the absence of body forces, the equation of motion is obtained as

$$\nabla \cdot \sigma = \rho \frac{\partial^2 \mathbf{u}}{\partial t^2} \tag{5.13}$$

The stress acting on the surface of a volume element can also cause deformation, such as linear, shearing, and rotation. This internal deformation can be described by a component strain tensor ϵ_{ij}, which is related to displacement.

$$\epsilon_{ij} = \frac{1}{2} \left(\frac{\partial u_i}{\partial x_j} + \frac{\partial u_j}{\partial x_i} \right) \tag{5.14}$$

Hooke's law describes the relationship between stress and strain for linear elasticity

$$\sigma_{ij} = C_{ijkl} \epsilon_{kl}, \tag{5.15}$$

where C_{ijkl} is the third-order stiffness tensor, which represents 21 independent elastic moduli of the anisotropic medium. For elastic, isotropic medium the stiffness tensor can be written with two elasticity coefficients, the Lame parameters λ and μ. Here μ is called the shear-modulus.

$$C_{ijkl} = \lambda \delta_{ij} \delta_{kl} + \mu \left(\delta_{ik} \delta_{jl} + \delta_{il} \delta_{jk} \right), \tag{5.16}$$

where $\delta_{ij} = 1$ only if $i = j$. Then

$$\sigma_{ij} = \lambda \theta \delta_{ij} + 2\mu \epsilon_{ij}, \tag{5.17}$$

where θ is the stress tensor given by $\theta = \sigma_{xx} + \sigma_{yy} + \sigma_{zz}$. Now we can substitute Eq. 5.17 in to Eq. 5.12 and the elastic wave equation is obtained as

$$\rho \frac{\partial^2 \mathbf{u}}{\partial t^2} = \bigtriangledown (\lambda \theta) + \mu \bigtriangledown^2 \mathbf{u} + \mu \bigtriangledown \theta + 2\epsilon \cdot \bigtriangledown \mu \tag{5.18}$$

The strength of the $\bigtriangledown \lambda$ and $\bigtriangledown \mu$ tend to zero when the wave frequency is high compared to the scale length of the variation in λ and μ. Ignoring the gradient terms of λ and μ, the elastic wave equation can be approximated as

$$\rho \frac{\partial^2 \mathbf{u}}{\partial t^2} = (\lambda + 2\mu) \bigtriangledown (\bigtriangledown \cdot \mathbf{u}) - \mu \bigtriangledown \times \bigtriangledown \times \mathbf{u} \tag{5.19}$$

By introducing the particle velocity $\mathbf{v} = \frac{\partial \mathbf{u}}{\partial t}$, we can express the equations of wave propagation as

$$\rho \frac{\partial v_i}{\partial t} = f_i + \frac{\sigma_{ij}}{\partial x_j} \tag{5.20}$$

$$\frac{\partial \sigma_{ij}}{\partial t} = \lambda \frac{\partial \theta}{\partial t} \delta_{ij} - 2\mu \frac{\partial \epsilon_{ij}}{\partial t} \tag{5.21}$$

$$\frac{\partial \epsilon_{ij}}{\partial t} = \frac{1}{2} \left(\frac{\partial v_i}{\partial x_j} + \frac{\partial v_j}{\partial x_i} \right) \tag{5.22}$$

5.2.1 The Links Between Wave Velocities and Elastic Moduli

Seismic waves are elastic waves. The two independent parameters in elastic tensor can be expressed in terms of elastic moduli. If κ represents the bulk modulus of the material, then

$$\lambda = \kappa - \frac{2\mu}{3} \tag{5.23}$$

and the Young's moduli

$$E = \frac{(3\lambda + 2\mu)\,\mu}{(\lambda + \mu)}. \tag{5.24}$$

97

The wave propagation velocity depends on the elasticity and the density of the medium. The P-wave and S-wave velocities are

$$V_p = \sqrt{\frac{\kappa + 4\mu/3}{\rho}} = \sqrt{\frac{\lambda + 2\mu}{\rho}} \tag{5.25}$$

and

$$V_s = \sqrt{\frac{\mu}{\rho}}, \tag{5.26}$$

where V_s and V_p are P-wave and S-wave velocities of the medium. Moreover, the shear moduli G is defined as

$$G = \mu = \rho V_s^2. \tag{5.27}$$

5.3   Full-Waveform Inversion

The FWI technique consists of two stages. The first stage includes forward modeling to generate synthetic wave-fields and the second stage includes the model updating by considering when the residual between predicted and measured surface velocities are negligible. In this thesis, we consider wave equations in 2-D cartesian coordinates.

5.3.1   Forward Problem

Forward modeling seeks the solutions of the 2-D elastic wave equations. We simulate wave propagation by solving 2-D elastic wave equations numerically. The governing equations for 2-D elastic wave propagation can be obtained using Equations 5.20-5.22.

Let σ_{xx}, σ_{zz}, and σ_{xz} be the components of stress tensor and u, v be the particle velocity components. The spatial directions in the 2D plane are x and z.

Then the equations governing particle velocity in 2-D are

$$\frac{\partial u}{\partial t} = \frac{1}{\rho} \left(\frac{\partial \sigma_{xx}}{\partial x} + \frac{\partial \sigma_{xz}}{\partial z} \right) = f_1 \left(\rho \right) \tag{5.28}$$

$$\frac{\partial v}{\partial t} = \frac{1}{\rho} \left(\frac{\partial \sigma_{xz}}{\partial x} + \frac{\partial \sigma_{zz}}{\partial z} \right) = f_2 \left(\rho \right) \tag{5.29}$$

and the equations governing stress-strain tensor are

$$\frac{\partial \sigma_{xx}}{\partial t} = (\lambda + 2\mu) \frac{\partial u}{\partial x} + \lambda \frac{\partial v}{\partial z} = f_3 \left(\lambda, \mu \right) \tag{5.30}$$

$$\frac{\partial \sigma_{zz}}{\partial t} = \lambda \frac{\partial u}{\partial x} + (\lambda + 2\mu) \frac{\partial v}{\partial z} = f_4 \left(\lambda, \mu \right) \tag{5.31}$$

$$\frac{\partial \sigma_{xz}}{\partial t} = \mu \left(\frac{\partial v}{\partial x} + \frac{\partial u}{\partial z} \right) = f_5 \left(\mu \right) \tag{5.32}$$

Here $\rho \left(x, z \right)$ is the mass density, $\mu \left(x, z \right)$, and $\lambda \left(x, z \right)$ are the Lame's coefficients of the material. The equations 5.28-5.32 can be written as

$$F \left(\rho \left(x, z \right), \mu \left(x, z \right), \lambda \left(x, z \right) \right) = \mathbf{d}. \tag{5.33}$$

Equations 5.28-5.32 are the forward equations of the FWI method. We can express the forward equations in the form of $A\mathbf{x} = \mathbf{b}$, where

$$A = \begin{bmatrix} \frac{\partial \sigma_{xx}}{\partial x} + \frac{\partial \sigma_{xz}}{\partial z} & 0 & 0 \\ \frac{\partial \sigma_{xz}}{\partial x} + \frac{\partial \sigma_{zz}}{\partial z} & 0 & 0 \\ 0 & \frac{\partial u}{\partial x} + \frac{\partial v}{\partial z} & 2\frac{\partial u}{\partial x} \\ 0 & \frac{\partial u}{\partial x} + \frac{\partial v}{\partial z} & 2\frac{\partial v}{\partial x} \\ 0 & 0 & \frac{\partial v}{\partial x} + \frac{\partial u}{\partial z} \end{bmatrix}, \mathbf{x} = \begin{bmatrix} \frac{1}{\rho} \\ \lambda \\ \mu \end{bmatrix}, \text{and } \mathbf{b} = \begin{bmatrix} \frac{\partial u}{\partial t} \\ \frac{\partial v}{\partial t} \\ \frac{\partial \sigma_{xx}}{\partial t} \\ \frac{\partial \sigma_{zz}}{\partial t} \\ \frac{\partial \sigma_{xz}}{\partial t} \end{bmatrix}. \tag{5.34}$$

To solve the above forward equations numerically, specific boundary conditions are needed. We impose three boundary conditions: the free surface boundary condition on the top of the domain, the absorbing boundary condition on the right side of the

domain and bottom of the domain, and the symmetric boundary condition on the left-hand side of the domain.

Free Surface Boundary Conditions

The measurements of the wavefield are generally collected along the earth's subsurface. Therefore, we impose the free surface boundary condition on the top of the domain by setting the vertical stress components are as zero.

$$
\begin{cases}
\sigma_{xz} = 0 \\
\sigma_{zz} = 0.
\end{cases}
\tag{5.35}
$$

Absorbing Boundary Conditions

Numerical methods are solved for a region of space by imposing artificial boundaries. Therefore, to avoid the reflections from the boundaries, absorbing boundary conditions should be applied on the right-hand side and the bottom of the domain. Thus the absorbing condition at the bottom of the domain is

$$
\begin{cases}
\frac{\partial u}{\partial t} + V_s \frac{\partial u}{\partial z} = 0 \\
\frac{\partial v}{\partial t} + V_p \frac{\partial v}{\partial z} = 0
\end{cases}
\tag{5.36}
$$

and at the right-hand side of the domain

$$
\begin{cases}
\frac{\partial u}{\partial t} + V_s \frac{\partial u}{\partial x} = 0 \\
\frac{\partial v}{\partial t} + V_p \frac{\partial v}{\partial x} = 0,
\end{cases}
\tag{5.37}
$$

where V_s and V_p are sheer and pressure wave velocities, respectively.

Symmetric Condition

To save computational time, we imposed a symmetric condition along the load line. Thus at the left-hand side of the domain we set

$$\begin{cases} \sigma_{xz} = 0 \\ u = 0. \end{cases} \tag{5.38}$$

To solve the forward equations, one can use numerical approaches such as finite difference method, finite element method, and Fourier/spectral method. Ref. [21] used a classic velocity-stress staggered-grid finite-difference solution of the 2-D elastic wave equations in the time domain (Virieux, 1986) with the absorbing boundary conditions (Clayton and Engquist, 1977). In that approach, a direct discretization of the equations 5.28-5.32, both in time and in space is considered. We follow the same approach for solving forward equations.

5.3.2 A Classic Finite Difference Scheme

To solve Eqs. 5.28-5.32 with the above boundary conditions 5.35 - 5.37, the derivatives are discretized using central finite differences. For instance, the second order central difference approximation formula for the function $f \in C^3[a, b]$ and $x - h, x, x + h \in [a, b]$ is defined as:

$$f'(x) = \frac{f(x + h) - f(x - h)}{2h} + \mathbf{O}\left(h^2\right), \tag{5.39}$$

where $\mathbf{O}\left(h^2\right)$ is the truncation error. This term indicates that the error of the approximation is proportional to the step size of h. To get a good approximation with a small error, h should be sufficiently small.

In our problem, for a field variable f, the temporal discretization is

$$D_t [f]_{i,j}^k = \frac{f_{i,j}^{k+1/2} - f_{i,j}^{k-1/2}}{\delta t} = \frac{\partial f}{\partial t}|_{i,j}^k + O(\delta^2) \tag{5.40}$$

and the spatial discretizations are

$$D_x [f]_{i,j}^k = \frac{f_{i+1/2,j}^k - f_{i-1/2,j}^k}{h_1} = \frac{\partial f}{\partial x}|_{i,j}^k + O(h_1^2) \tag{5.41}$$

$$D_z [f]_{i,j}^k = \frac{f_{i,j+1/2}^k - f_{i,j-1/2}^k}{h_3} = \frac{\partial f}{\partial z}|_{i,j}^k + O(h_3^2). \tag{5.42}$$

Here i, j, and k represent the indices used in the discretization for the directions x, y and time. The domain is discretized in the x, y and time directions as shown in Fig. 5.7. h_1, h_3, and δt are the grid steps for x, z and time directions, respectively. f can take $u, v, \sigma_{xx}, \sigma_{zz}, \sigma_{xz}$. For example, the derivative terms $\frac{\partial u}{\partial t}$, $\frac{\partial \sigma_{xx}}{\partial x}$, and $\frac{\partial \sigma_{xz}}{\partial z}$ in Eq. 5.28 can be approximated as

$$\frac{\partial u}{\partial t} = \frac{u_{i,j}^{k+1/2} - u_{i,j}^{k-1/2}}{2\delta t} \tag{5.43}$$

$$\frac{\partial \sigma_{xx}}{\partial x} = \frac{\sigma_{xx_{i+1/2,j}}^k - \sigma_{xx_{i-1/2,j}}^k}{2h_1} \tag{5.44}$$

$$\frac{\partial \sigma_{xz}}{\partial z} = \frac{\sigma_{xz_{i,j+1/2}}^k - \sigma_{xz_{i,j-1/2}}^k}{2h_3} \tag{5.45}$$

Then, Eq. 5.28 can be approximated using Eqs. 5.43, 5.44, and 5.45 as,

$$\frac{u_{i,j}^{k+1/2} - u_{i,j}^{k-1/2}}{2\delta t} = \frac{1}{\rho} \left(\left(\frac{\sigma_{xx_{i+1/2,j}}^k - \sigma_{xx_{i-1/2,j}}^k}{2h_1} \right) \left(\frac{\sigma_{xz_{i,j+1/2}}^k - \sigma_{xz_{i,j-1/2}}^k}{2h_3} \right) \right) \tag{5.46}$$
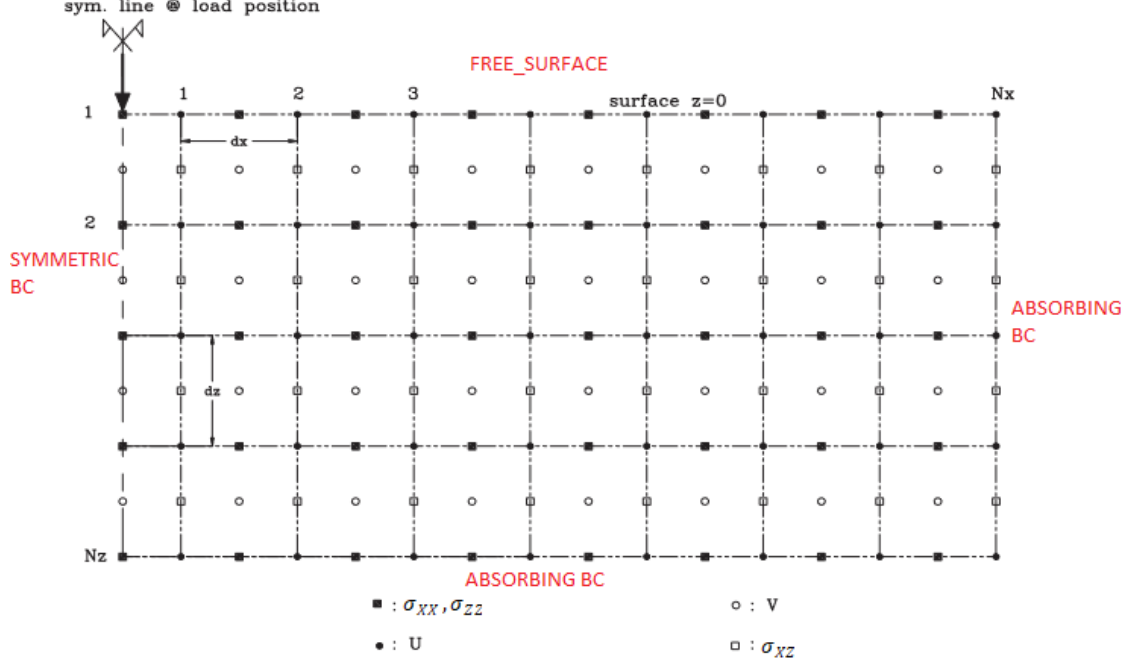
Figure 5.7: The discretization of the domain (photo credit: Ref. [21]).

Equations 5.47 - 5.51 are the second order accuracy numerical scheme after discretizing the system of differential equations (Virieux, 1986). The velocity field $(U, V) = (u, v)$ at time $\left(k + \frac{1}{2}\right) \delta t$ and the stress-tensor field $(T_{xx}, T_{zz}, T_{xz}) = (\sigma_{xx}, \sigma_{zz}, \sigma_{xz})$ at time $(k + 1) \delta t$ are explicitly calculated with the numerical scheme.

$$U_{i,j}^{k+1/2} = U_{i,j}^{k-1/2} + B_{i,j}\frac{\delta t}{h_1}\left(Txx_{i+1/2,j}^k - Txx_{i-1/2,j}^k\right) + B_{i,j}\frac{\delta t}{h_3}\left(Txz_{i,j+1/2}^k - Txz_{i,j-1/2}^k\right)$$

$$(5.47)$$

$$V_{i+1/2,j+1/2}^{k+1/2} = V_{i+1/2,j+1/2}^{k-1/2} + B_{i+1/2,j+1/2}\frac{\delta t}{h_1}\left(Txz_{i+1,j+1/2}^k - Txz_{i,j+1/2}^k\right)$$

$$+ B_{i+1/2,j+1/2}\frac{\delta t}{h_3}\left(Tzz_{i+1/2,j+1}^k - Txz_{i+1/2,j}^k\right) \qquad (5.48)$$

$$Txx_{i+1/2,j}^{k+1} = Txx_{i+1/2,j}^k + (L+2M)_{i+1/2,j}\frac{\delta t}{h_1}\left(U_{i+1,j}^{k+1/2} - U_{i,j}^{k+1/2}\right)$$

$$+ L_{i+1/2,j}\frac{\delta t}{h_3}\left(V_{i+1/2,j+1/2}^{k+1/2} - U_{i+1/2,j-1/2}^{k+1/2}\right) \qquad (5.49)$$

$$Tzz_{i+1/2,j}^{k+1} = Tzz_{i+1/2,j}^k + (L+2M)_{i+1/2,j}\frac{\delta t}{h_1}\left(V_{i+1/2,j+1/2}^{k+1/2} - V_{i+1/2,j-1/2}^{k+1/2}\right)$$

$$+ L_{i+1/2,j}\frac{\delta t}{h_3}\left(U_{i+1,j}^{k+1/2} - U_{i,j}^{k+1/2}\right) \qquad (5.50)$$

$$Txz_{i,j+1/2}^{k+1} = Txz_{i,j+1/2}^k + M_{i,j+1/2}\frac{\delta t}{h_3}\left(U_{i,j+1}^{k+1/2} - U_{i,j}^{k+1/2}\right)$$

$$+ M_{i,j+1/2}\frac{\delta t}{h_1}\left(V_{i+1/2,j+1/2}^{k+1/2} - V_{i-1/2,j+1/2}^{k+1/2}\right) \qquad (5.51)$$

Here, M and L represent the Lame coefficients (μ, λ) and

$$B = \frac{1}{\rho} \qquad (5.52)$$

as shown in Fig. 5.7.

Moreover, the initial condition at time $t = 0$ is set such that the stress and velocity are zero everywhere in the domain. The medium is perturbed by changing vertical stress σ_{zz} at the source using

$$R(t) = \left[1 - 2\pi^2 f_c^2 (t - t_0)^2\right]\exp\left[-\pi^2 f_c^2 (t - t_0)^2\right], \qquad (5.53)$$

where f_c is the center of the frequency band and t_0 is the time shift.

Stability Criterion

Numerical schemes are associated with numerical errors due to the approximation of the derivatives in the partial differential scheme. It is important to obtain a stable wave propagation solution from the finite difference scheme. With some numerical schemes, the errors made at one-time step grow as the computations proceed. Such a numerical scheme is said to be unstable so the results blow up. If the errors decay with time as the computations proceed, we say a finite difference scheme is stable. In that case, the numerical solutions are bounded.

To obtain a bounded solution from the finite difference scheme, we obtain δt from the stability criterion (Virieux, 1986) given by

$$\delta t \leq \frac{1}{V_{\max}\sqrt{\frac{1}{h_1^2} + \frac{1}{h_3^2}}}. \tag{5.54}$$

Here $V_{\max}$ is the maximum P-wave velocity in the media.

Inputs for the forward problem are the model parameters such as density, Lames's moduli, P-wave velocity, and S-wave velocity. Then the particle velocities and stresses (outputs) are calculated by implementing the numerical scheme (Eqs. 5.47 - 5.51) in MATLAB.

5.3.3 Inverse Problem

The FWI is the problem of finding the parametrization of the subsurface using seismic wave field. Thus the goal of inversion is to estimate a discrete parametrization of the subsurface by minimizing the residual between the observed seismic data and the numerically predicted seismic data. If seismic waves are generated from NS sources (one shot at a time) and are recorded by NR receivers, then the residual for all shots

and receivers can be defined as

$$\Delta\mathbf{d}_{ij} = F_{ij}(\mathbf{m}) - \mathbf{d}_{ij}, \tag{5.55}$$

where $\mathbf{d}_{i,j}$ and $F_{i,j}(\mathbf{m})$ are the observed data and the estimated data associated with the model parameters $\mathbf{m}$, and indices i and j denote the ith shot and j^{th} receiver, respectively. In this problem, the model parameters are density, $\rho(x,z)$, or one of Lame's moduli, $\lambda(x,z)$ and $\mu(x,z)$ or $V_s(x,z)$ and $V_p(x,z)$. However, due to the relationship between elastic moduli and wave velociies only three model parameters are enough to characterize the subsurface.

This problem can be modeled as a least squares problem. The objective function of the inverse problem can be expressed as minimizing a least square error $E_d(m)$. For $\Delta\mathbf{d} : M \rightarrow D$ the problem is

$$\text{argmin}_{\mathbf{m}} E_d(\mathbf{m}) = \frac{1}{2}\Delta\mathbf{d}^T\Delta\mathbf{d} = \frac{1}{2}||\Delta\mathbf{d}||_2^2, \tag{5.56}$$

where $E_d(\mathbf{m})$ is called the misfit function [129]. Here $\Delta\mathbf{d} = \{\Delta\mathbf{d}_{i,j}, i = 1, ..., NS, j = 1, ..., NR\}$. $\Delta\mathbf{d}$ is a column vector, which is the combination of residuals $\Delta\mathbf{d}_{i,j}$ for all shots and receivers. Optimization problems of this form are called nonlinear least-squares problem and our target here is to find model parameters $\mathbf{m}^*$ that minimizes $E_d(\mathbf{m})$.

Model updating methods such as Gradient descent method, Newton method, and the Gauss-Newton method can be used to solve the above optimization problem.

Gradient Descent Method

The gradient method solve the non linear least square problem with search directions defined by the gradient of the function $E_d(\mathbf{m})$. $E_d(\mathbf{m})$ decreases in the negative

direction of the gradient of $E_d(\mathbf{m})$, $-\nabla E_d(\mathbf{m})$. For iterations n $\geq$ 0,

$$\mathbf{m}^{n+1} = \mathbf{m}^n - \alpha \nabla E_d(\mathbf{m}) \tag{5.57}$$

iterates to find the minimum number $\mathbf{m}^*$. Here α is the step size. The gradient contains the first partial derivatives of $E_d(\mathbf{m})$ with respect to the model parameters $\mathbf{m}$.

$$\nabla E_d(\mathbf{m}) = \left[\frac{\partial F_i(\mathbf{m})}{\partial m_j}\right]^T \Delta d, \tag{5.58}$$

where $i = 1, ..., NS \times NR$ and $j = 1, ..., M$. Here $\left[\frac{\partial F_i(\mathbf{m})}{\partial m_j}\right]$ is defined as the Jacobian matrix J.

Gauss-Newton Method

The Newton method is based on the model update with the second order partial derivatives of the function $E_d(\mathbf{m})$. The Hessian matrix,

$$H = -\nabla^2 E_d(\mathbf{m}) = \frac{\partial}{\partial m_p}\left[J^T \Delta \mathbf{d}\right] \tag{5.59}$$

records the second order derivatives. The Newton method is given by

$$\mathbf{m}^{n+1} = \mathbf{m}^n - H^{-1} J^T \Delta \mathbf{d}. \tag{5.60}$$

However, the calculation of the Hessian matrix is difficult. Therefore, the Newton method has not been often used in geophysical inverse problems. The Hessian matrix can be written as

$$H = J^T J + \frac{\partial J^T}{\partial m_p} \Delta \mathbf{d}. \tag{5.61}$$

By considering the negligibility of the second term of the Eq. 5.61, the Hessian matrix can be approximated as

$$H_a = J^T J \tag{5.62}$$

and the Gauss-Newton formula [124] with the approximate Hessian matrix is

$$\mathbf{m}^{n+1} = \mathbf{m}^n - H_a^{-1} J^T \Delta \mathbf{d}. \tag{5.63}$$

The Gauss-Newton method is effective for solving non-linear problems and guarantees faster convergence rates than the gradient method. With good initial guesses, the Gauss-Newton method converges nearly quadratically. But theoretically, the Gauss-Newton method converges linearly. However, when the Jacobian is ill-conditioned or singular, the search direction becomes very large and the Gauss-Newton method is not globally convergent. Thus to solve the original problem, regularization of the original problem can be used.

The regularized misfit function E used in geophysical inversion[129] is defined as

$$E\left(\mathbf{m}\right) = E_d\left(\mathbf{m}\right) + \lambda E_m\left(\mathbf{m}\right), \tag{5.64}$$

where λ is the regularization parameter that controls the relative importance of the $E_m\left(\mathbf{m}\right)$, where $E_m\left(\mathbf{m}\right)$ is the model objective function that contains a priori information of the model. $E_m\left(\mathbf{m}\right)$ can be written as

$$E_m\left(\mathbf{m}\right) = \frac{1}{2}||L\Delta\mathbf{m}||^2, \tag{5.65}$$

where L is discrete linear operator [129]. Then the regularized Gauss-Newton formula with step size α is

$$\mathbf{m}^{n+1} = \mathbf{m}^n - \alpha^n \left[J^T J + \lambda L^T L\right]^{-1} J^T \Delta \mathbf{d}. \tag{5.66}$$

When $L = I$, Eq. 5.66 represents the damped least-squares method [129]. L can be used as a discrete 2-D Laplacian operator[136], which is defined as

$$L_i \Delta \mathbf{m} \approx P_i \Delta \mathbf{m} = (\Delta m_i)^E + (\Delta m_i)^W + (\Delta m_i)^N + (\Delta m_i)^S - 4(\Delta m_i), \qquad (5.67)$$

where E, W, N, and S are the four neighbors of the ith model parameter and P_i is the ith row of the Laplacian matrix whose elements are either 1, -4, or 0. Ref. [129] used both model objective functions from damped least-squares method and discrete 2-D Laplacian operator in the regularized problem. The regularized Gauss-Newton formula [129] to geophysical inversion can be written as

$$\mathbf{m}^{n+1} = \mathbf{m}^n - \alpha^n \left[J^T J + \lambda_1 P^T P + \lambda_2 I^T I \right]^{-1} J^T \Delta \mathbf{d}. \qquad (5.68)$$

The step length α^n is determined by

$$\alpha^n \approx \frac{\left[J^T g^n \right]^T [F(\mathbf{m}^n) - \mathbf{d}]}{\left[J^T g^n \right]^T [J^t g^n]}, \qquad (5.69)$$

where $g^n = \left[J^T J + \lambda_1 P^T P + \lambda_2 I^T I \right]^{-1} J^T [F(\mathbf{m}^n) - \mathbf{d}]$.

For model updating, Ref. [21] uses Eq. 5.68 in the FWI. Following modifications to the residual and the Jacobian matrix are also used in Ref. [21].

1. The residual Δd_{ij} is modified to avoid the influence of the source on the estimation during inversion. For that modification cross-convolution[1] of wave-fields is used. The symbol * denotes the convolution. Let the model $\mathbf{m}$ includes all unknowns (S-wave and P-wave velocities of cells). For each shot gathering, the

---

[1]The convolution of two functions f and g is defined as the integral of the product of the two functions after one is reversed and shifted. Mathematically,

$$(f * g) = \int_{-\infty}^{\infty} f(\tau) g(t - \tau) \, d\tau$$

estimated wave-fields are convolved with a reference trace from the observed wave-field, and the observed wave-fields are convolved with a reference trace from the estimated wave-field. Thus the modified residual between estimated and observed data for the ith shot and j^{th} receiver is

$$\Delta d_{ij} = F_{i,j}\left(\mathbf{m}\right) * d_{i,k} - d_{ij} * F_{i,k}\left(\mathbf{m}\right), \tag{5.70}$$

where $d_{i,j}$ and $F_{i,j}\left(\mathbf{m}\right)$ are the observed data and the estimated data associated with the model $\mathbf{m}$. $F_{i,k}\left(m\right)$ and $d_{i,k}$ are the reference traces from the estimated and observed data, respectively, at the kth receiver position.

2. The Jacobian matrix J is obtained by taking the partial derivatives of seismograms with respect to parameters of model $\mathbf{m}$ and convolving with the reference traces and defined by

$$J_{ij,M} = \frac{\partial F_{i,j}\left(\mathbf{m}\right)}{\partial m_p} * d_{i,k} - d_{i,j} * \frac{\partial F_{i,k}\left(\mathbf{m}\right)}{\partial m_p}, \tag{5.71}$$

for $i = 1, ..., NS, j = 1, ..., NR$, and $p = 1, ..., M$.

The Gauss-Newton model updating algorithm that minimizes the error $E_d(\mathbf{m})$ can be expressed as

---
Algorithm 6 Gauss- Newton Algorithm

    Input: starting point $\mathbf{m}_0$, tolerance ϵ
    Output: $\mathbf{m}^*$
 1: $\mathbf{m}_k \leftarrow \mathbf{m}_0$
 2: Calculate Jacobian J and P
 3: $\mathbf{p}_k \leftarrow J^T J + \lambda_1 P^T P + \lambda_2 I^T I$
 4: $R \leftarrow ||\mathbf{p}_k||$
 5: $\alpha^k \leftarrow$ step size
 6: $\mathbf{m}_{k+1} \leftarrow \mathbf{m}_k + \alpha^n \mathbf{p}_k$
 7: **if** $R = ||\mathbf{p}_k|| < \epsilon$ **then**
 8:     $\mathbf{m}^* \leftarrow \mathbf{m}_{k+1}$
 9: **else** $\mathbf{m}_k \leftarrow \mathbf{m}_{k+1}$
10: **end if**

The λ_1 and λ_2 are between 0 and ∞. For this study, $\lambda_1 = 0.05$ and $\lambda_2 = 0.0005$ are chosen as appropriate values.

5.4   Illustration of Inverse Problem and Regularization Problem

Let's consider the problem defined by the matrix equation

$$A\mathbf{x} = \mathbf{b}. \tag{5.72}$$

The forward problem is the problem of finding $\mathbf{b}$ for a given A and $\mathbf{x}$. The inverse problem is the problem of finding $\mathbf{x}$ for a given A and $\mathbf{b}$. In many applications, we measure the data or responses $\mathbf{b}$ and try to find the quantities or parameters of the original problem. A simple example of an inverse problem is Model fitting. For a given data set of measured points (t_i, y_i), we wish to determine the parameters a, b, and c in such a way that the observed data are fitted to some theoretical model given by

$$y = a + bt + ct^2. \tag{5.73}$$

Figure 5.8 illustrates the inverse and forward problem for a mathematical model.
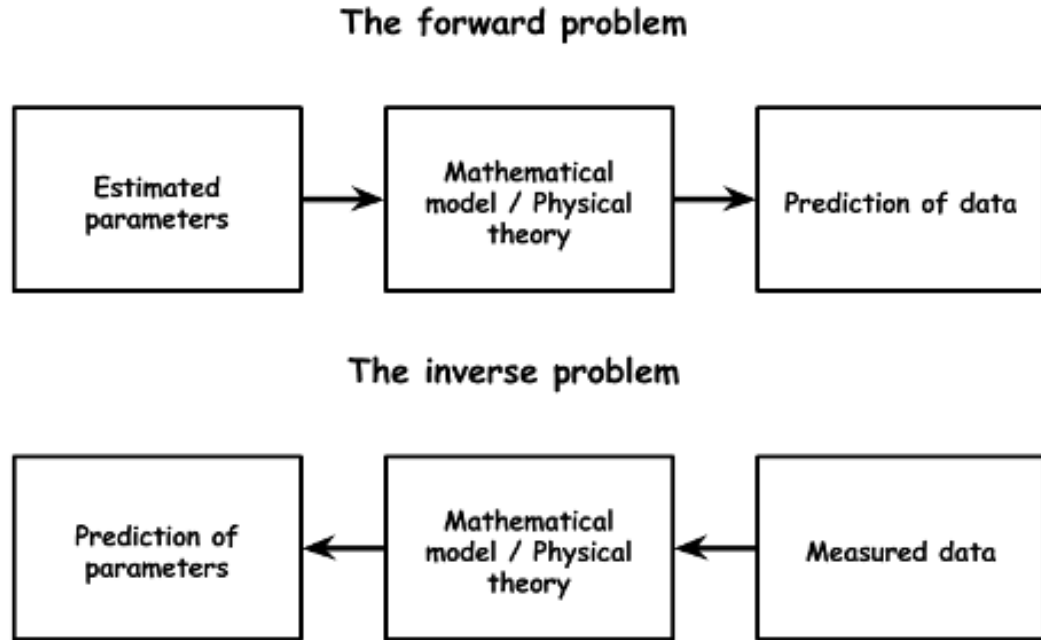
Figure 5.8: The forward and the inverse problem (photo credit: Ref. [22])

According to Hadamard [137], the problem defined by the matrix equation:

$$A\mathbf{x} = \mathbf{b} \qquad (5.74)$$

is well-posed, if the following three conditions hold:

1. it has a solution

2. the solution is unique

3. the solution depends continuously on data and parameters.

A problem that violates any of these three conditions is called an ill-posed problem. Let's illustrate these conditions using simple examples.

Example 5.4.1. *Consider the problem [23], $A\boldsymbol{x} = \boldsymbol{b}$, where*

$$A = \begin{bmatrix} 1 & 1 \\ 2 & -1 \end{bmatrix}, \boldsymbol{b} = \begin{bmatrix} 5 \\ 4 \end{bmatrix} \text{ and } \boldsymbol{x} = \begin{bmatrix} x_1 \\ x_2 \end{bmatrix}. \tag{5.75}$$

To solve the problem, we can write the problem as a system of two equations.

$$x + y = 5 \tag{5.76}$$

$$2x - y = 4 \tag{5.77}$$

These two lines intersect at the point $(3, 2)$, which is called the solution (see Fig. 5.9(a)). In this case, the problem has only one solution and we say that the problem has unique solution. The unique solution is $x = \begin{bmatrix} 3 \\ 2 \end{bmatrix}$.

This problem satisfies the first two conditions of the well-posedness.

Example 5.4.2. *Consider the problem [23], $A\boldsymbol{x} = \boldsymbol{b}$, where*

$$A = \begin{bmatrix} -2 & 1 \\ -4 & 2 \end{bmatrix}, \boldsymbol{b} = \begin{bmatrix} 3 \\ 2 \end{bmatrix} \text{ and } \boldsymbol{x} = \begin{bmatrix} x_1 \\ x_2 \end{bmatrix}. \tag{5.78}$$

By writing the problem as a system of two equations,

$$-2x + y = 3 \tag{5.79}$$

$$-4x + 2y = 2 \tag{5.80}$$

one can see that two parallel lines in the xy-plane (see Fig. 5.9(b)). There is no point of intersection and therefore, no solution to the original problem. Thus the problem is ill-posed.

Example 5.4.3. *Consider the problem [23], $A\boldsymbol{x} = \boldsymbol{b}$, where*

$$A = \begin{bmatrix} 4 & -2 \\ 6 & -3 \end{bmatrix}, \boldsymbol{b} = \begin{bmatrix} 6 \\ 9 \end{bmatrix} \quad and \quad \boldsymbol{x} = \begin{bmatrix} x_1 \\ x_2 \end{bmatrix}. \tag{5.81}$$

In this problem, both equations can be written as

$$y = 2x - 3. \tag{5.82}$$

Thus any point on the line is a solution and there are infinitely many solutions (see Fig. 5.9(c)). One can see that this problem is ill-posed since it does not satisfy the second condition, which is the uniqueness of the solutions.
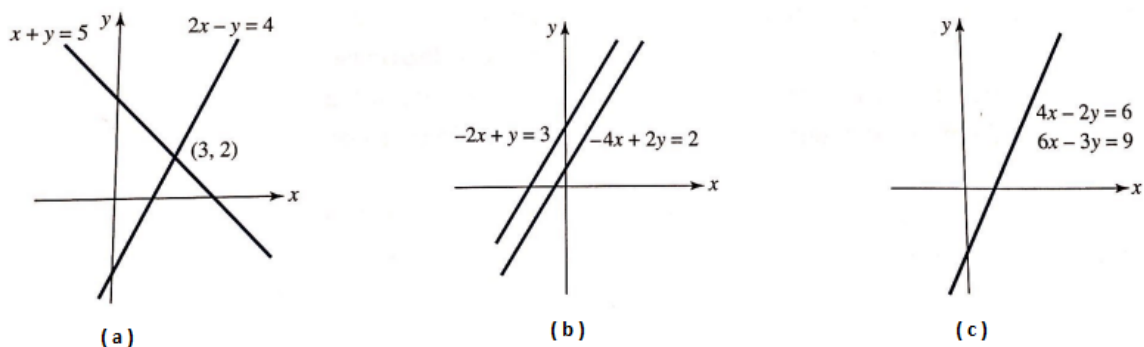
Figure 5.9: Three possibilities that can arrive in solving of $A\mathbf{x} = \mathbf{b}$. (photo credit: Ref. [23])

The third condition of the well-posedness can be described as if a small changes in initial condition and parameter values result in small changes in the solution. To measure this change, we can use condition number with an appropriate measure. The condition number is defined more precisely as the maximum ratio of the relative error in $\mathbf{x}$ to the relative error in $\mathbf{b}$. If the condition number is large or infinite, a small change (error) in $\mathbf{b}$ may result a large change (error) in $\mathbf{x}$.

The condition number of A in Ex. 5.4.1 is 1.76. That means small change in $\mathbf{b}$ causes a small change in the solution. Thus the problem has a well-defined solution.

114

The condition number in Ex. 5.4.2 is 4.8×10^{16}. This implies that the problem in Ex. 5.4.2 is ill-conditioned and does not have a well-posed solution for all data and parameters.

A problem defined by $A\mathbf{x} = \mathbf{b}$ with a square matrix A of size $n \times n$ posses well-posed solution, then the matrix is invertible, i.e. $\det A \neq 0$ and the unique solution is given by $\mathbf{x} = A^{-1}\mathbf{b}$. The problem is ill-posed if the $\det A = 0$ or the matrix A is not invertible.

One can see that, for Ex. 5.4.1, $\det A = -3 \neq 0$ and the solution is given as

$$\mathbf{x} = A^{-1}\mathbf{b} = \begin{bmatrix} 1/3 & 1/3 \\ 2/3 & -1/3 \end{bmatrix} \begin{bmatrix} 5 \\ 4 \end{bmatrix} = \begin{bmatrix} 3 \\ 2 \end{bmatrix} \tag{5.83}$$

However, for Ex. 5.4.2, $\det A = 0$. For these type of problems where the problem is ill-posed, to obtain a solution, a regularization method can be used. In general, least square solution of an inverse problem $A\mathbf{x} = \mathbf{b}$ seeks to minimize

$$||A\mathbf{x} - \mathbf{b}||^2. \tag{5.84}$$

The regularization problem is defined by adding a regularization term to the least squares minimization problem as

$$||A\mathbf{x} - \mathbf{b}||^2 + ||\Gamma \mathbf{x}||^2, \tag{5.85}$$

where Γ is the Tikhonov matrix. This matrix can be chosen as a multiple of the identity matrix. Thus the regularization problem can be written as solving $A\mathbf{x} = \mathbf{b}$ such that minimizing

$$||A\mathbf{x} - \mathbf{b}||^2 + \alpha ||\mathbf{x}||^2, \tag{5.86}$$

where α is the regularization parameter. The next example shows how to regularize

an ill-posed problem and achieve a solution to the regularization problem.

Let's consider the ill-posed problem given in Ex. 5.4.2. The system of equations can be row reduce to obtain

$$
\begin{bmatrix} -2 & 1 \\ 0 & 0 \end{bmatrix} \begin{bmatrix} x_1 \\ x_2 \end{bmatrix} = \begin{bmatrix} 3 \\ -2 \end{bmatrix}.
$$

We seek the solution for x_1 and x_2.

One can see that this system of equations has an inconsistent solution as the second equation implies that $0 = -2$. If we like to find a solution on the line $-2x_1 + x_2 = 3$ which is closest to the origin, then the regularization problem can be defined as

$$
\arg \min_{x_1, x_2} \left\| \begin{bmatrix} -2 & 1 \\ 0 & 0 \end{bmatrix} \begin{bmatrix} x_1 \\ x_2 \end{bmatrix} - \begin{bmatrix} 3 \\ -2 \end{bmatrix} \right\|^2 + \left\| \begin{bmatrix} x_1 \\ x_2 \end{bmatrix} \right\|^2. \tag{5.87}
$$

The closest distance to the origin can be found using any distance measure, such as Euclidean distance (l^2 norm), l^1, and l^∞. Using the new problem, we can find a solution.

5.5 Different Cell Size Method to Store Jacobian

To solve the inverse problem introduced in Section 5.3.3, the regularized Gauss-Newton formula, which is defined in Eq. 5.68, can be used. The term $J^T J$ is defined as approximation to the Hessian matrix H. The major drawback of the Gauss-Newton method is memory and computational requirements of the Hessian matrix approximation.

The size of the Jacobian matrix is equal to the number of measured data points at receivers for each shot ($NR \times NS$) times the number of parameters (number of cells in the domain). In 3-D problems the size of the data set and the number of cells

in the domain is usually large. Hence, the storage of the Jacobian matrix requires an adequate amount of storage. For large scale problems, as the size of the Jacobian matrix increases, expenses to calculate $J^T J$ and invert $J^T J + \lambda_1 P^T P + \lambda_2 I^T I$ in Eq. 5.68 also increase. As we discussed in Section 5.1, there are several approaches to manage the storage and computational requirements of the inversion. Other than those techniques, Ref. [129] suggested a way to calculate H_a matrix without fully storing the Jacobian matrix. In their approach, the Jacobian matrix was divided into sub-matrices at the receivers and H_a matrix was calculated as follows:

$$
H_a = J^T J = \begin{bmatrix} J_1^T & J_2^T & \ldots & J_{NR}^T \end{bmatrix} \begin{bmatrix} J_1^T \\ J_2^T \\ \ldots \\ J_{NR}^T \end{bmatrix} = \sum_j^{NR} J_j^T J_j \tag{5.88}
$$

In this way, the H_a can be calculated by summing up the sub-matrices. The above technique can be implemented in MatLab with a loop that goes through the number of receivers. Therefore, the full Jacobian matrix does not have to be stored. Ref. [21] used the same technique for calculating H_a matrix. In the implementation, Ref. [21] did all the above manipulation with arrays rather than the matrices. Before calculating the H_a matrix, Ref. [21] converted the Jocobian sub matrices to an array.

In this thesis, we introduce an approach called different cell size method in addition to the computational techniques used in Ref. [129] and Ref. [21]. One special observation on the Jacobian matrix is that the partial derivatives values of the seismograms corresponds to the bottom cells in the domain are smaller when compared with those values at the top cells. By considering that fact, we decompose the spatial domain into three zones: zone 1, zone 2, and zone 3. Here the Jacobian matrix has the smallest values at the cells corresponding to the zone 3. Then zone 2 and 3 are discretized again with a bigger step size in the x direction and z direction. The dis-

cretization ratio for zone 3 is larger than that of zone 2 and the discretization ratio for zone 2 is larger than that of zone 1. For example, if dx and dz are step size for the regular domain in the x and z direction, then the discretization ratios for zone 2 can be $2dx$ and $2dz$. The discretization ratios for zone 3 can be $3dx$ and $3dz$. According to that, one cell in the zone 2 is created by combining 4 smaller cells and one cell in the zone 3 is created by combining 9 smaller cells in the regular domain

The values of the Jacobian at the bigger cells in zone 2 and zone 3 are re-evaluated by taking the sum of the values at the smaller cells. Then the values at the cells for the three zones are stored in matrices and converted to a single array. Figure 5.10 illustrates the procedure of the new discretization and converting values from matrix to an array for the three zones.
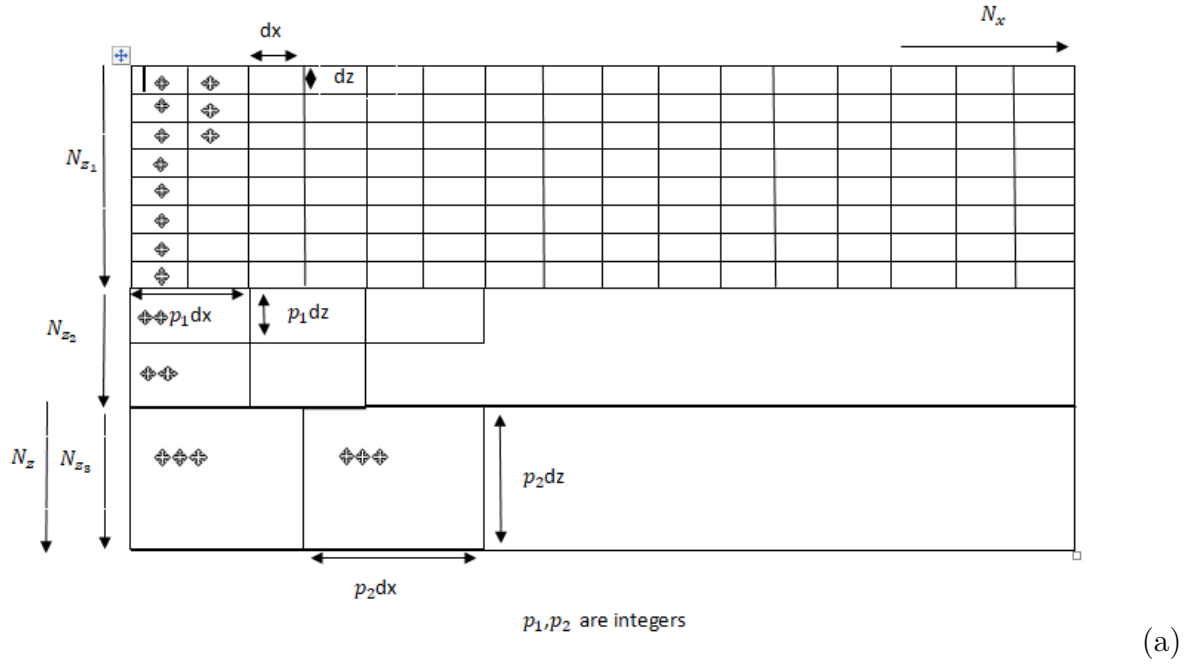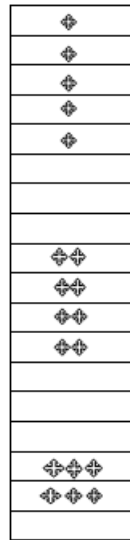
Figure 5.10: (a) Decomposition of the initial domain. The cell size of zone 1, zone 2, zone 3 are $dx \times dz$, $p_1 dx \times p_2 dz$, and $p_3 dx \times p_3 dz$, respectively. Here p_1, p_2 are integers. (b) The array formulation for the values in the cells in the domain.

Notice that the length of the obtained array for the different cell size method is shorter than the length of the array obtained with the regular cell method, which uses

Jacobian matrix without combining cells, for the initial domain. For the regular cell size method, the number of parameters is equal to the number of cells in the domain. For the proposed different cell size method, the number of cells is less than that of the regular cell size method as the bottom cells in the bottom zones are combined. Thus the size of the Hessian approximation matrix is smaller than that of the regular cell size method. Due to that, the Hessian approximation matrix can be calculated faster and less Jacobian storage is required. Thus the different cell size method is computationally inexpensive compared with the regular cell size method. Once we calculate the Hessian matrix, the Gauss-Newton update was used to find the shear wave and pressure wave velocities. Then the velocities in the bigger cells (combined cells) in zone 2 and zone 3 are converted back to smaller cells. The velocities at the smaller cells are calculated by taking the average of the bigger cells.

5.6   Numerical Results

In this section we investigate the capacity of the FWI in detection of embedded voids. The FWI technique with the different cell size method is applied to a synthetic model. Results are compared with the regular cell size method, which was used in Ref. [21].

5.6.1   A Synthetic Model with an Embedded Void

We consider a synthetic model of the earth for the investigation. The velocity profiles of the earth, i.e., S-wave and P-wave velocities of cells, are assumed to be known a priori. In the test configuration, the locations of a set of sources and receivers are also known. Using a known velocity structure, surface waveform data are calculated. These waveform data are then used as the input to the inversion program. If the waveforms were obtained from a field test, then the velocity structures can be extracted from the inversion of the surface waveform data. Theoretically, the extracted

velocity profile should be the same as the velocity profile assumed at the start.

We consider a synthetic model, which consists of two layers with an embedded air-filled void. The S-wave velocities V_s of the materials are 200 m/s for the soil layers and 700 m/s for limestone. The P-wave velocity is generated from the S-wave velocity V_p using

$$V_p = \sqrt{(2\,(1-\nu)\,/\,(1-2\nu))}V_s \tag{5.89}$$

for the entire domain. Here ν is 0.33. The void is encoded by setting the S-wave velocity in some computational cells to zero and P-wave velocity of those cells to 300 m/s. We consider 49.5 m long and 18 m depth domain for the test configuration. Figure 5.11 shows the S-wave velocity and P-wave velocity profiles for the assumed model. The soil layer (cyan color) is located approximately 7 m depth from the surface and the limestone layer (yellow color) is located from 8 m to 18 m depth. The void, blue rectangle in the domain, is located at the 15 m in the x direction and 7 m in the z direction (depth).
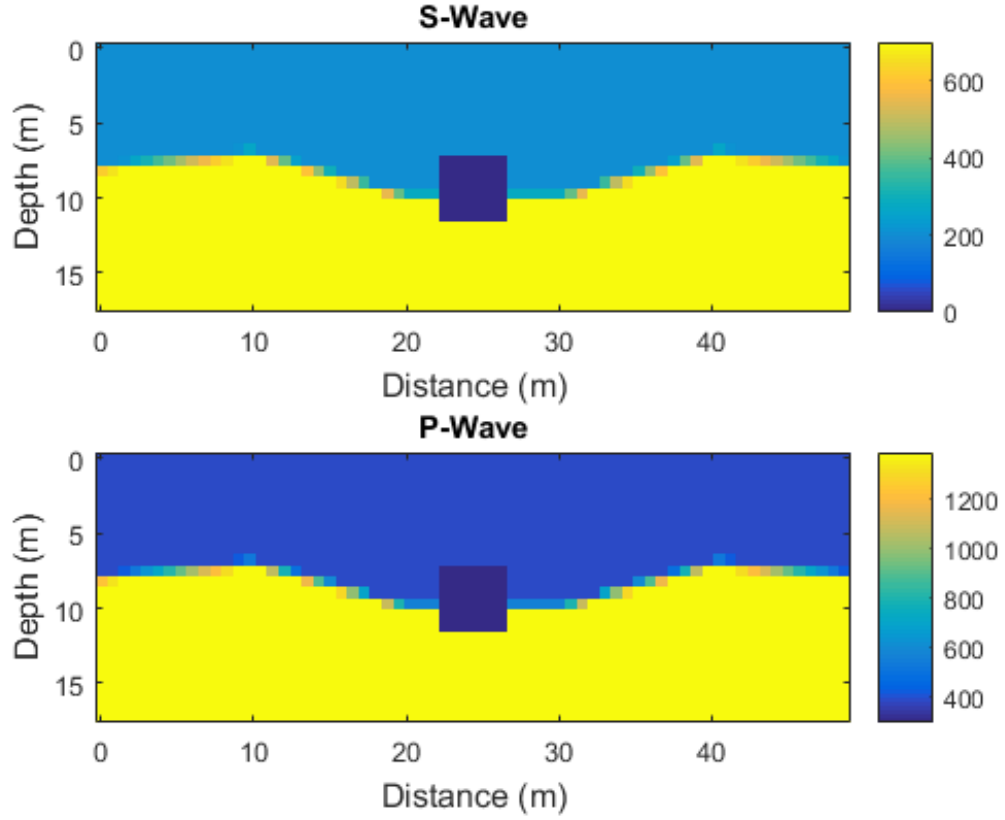
Figure 5.11: Velocity profiles of the true model

The finite difference code developed by Ref. [21] was used to generate a synthetic waveform data set. The code was modified to be used with the difference cell size method. The synthetic waveform data were recorded from 32 receivers spaced every 1.5 m from station 0.75 m to 49.5 m. 33 shots were used at 1.5 m spacing starting from 0 to 36 m on the ground surface. Fig. 5.12 shows the receiver locations and source positions. The waveform data obtained with the finite difference code is used for inversion. For the data inversion, an initial model is generated with S-wave velocity increasing with depth (from 200 m/s at the surface to 600 m/s at the bottom) and P-wave velocity was generated from the S-wave velocity using Eq. 5.89. Figure 5.13 shows the initial model, which was used for the inversion. Step size in the regular grid is $dx = dz = 0.3$ in both x and z directions. Widths of the three regions for the difference cell size methods are 6.75 m, 9 m, and 2.25 m for zone 1, zone 2, and zone

3, respectively (see Fig. 5.12). The corresponding step sizes are $dx, 2dx$, and $3dx$ for zone 1, zone 2, and zone 3, respectively.
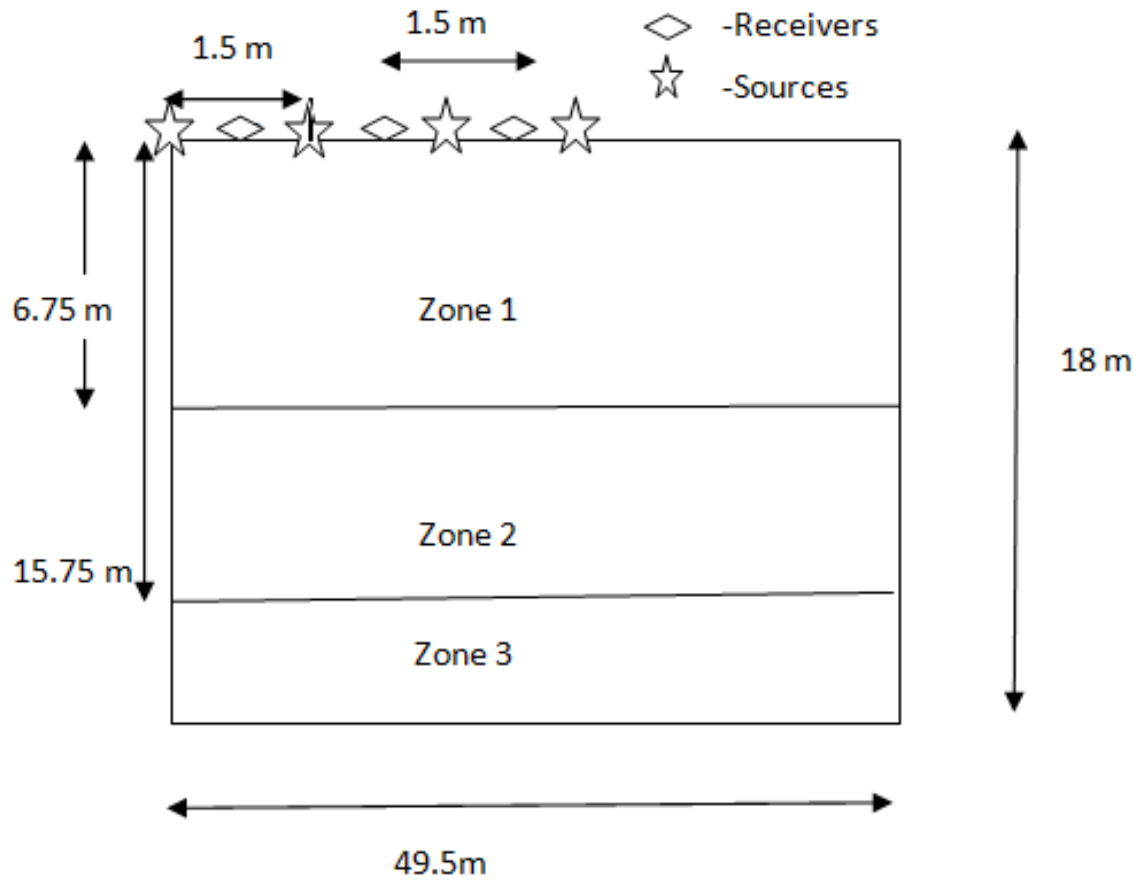
Figure 5.12: The domain categorization as zone 1, zone 2, and zone 3. Receivers and sources are on the ground surface.
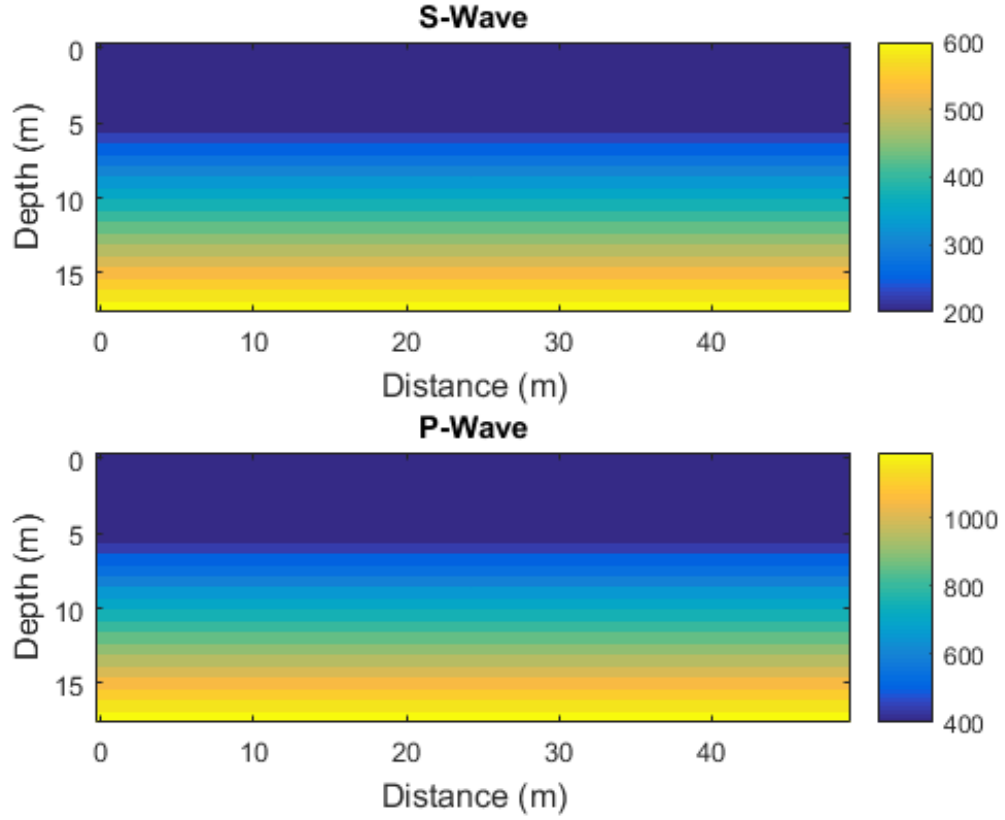
Figure 5.13: Velocity profiles of the initial model

With the initial model, four inversions are performed for the data sets at four frequency ranges at central frequencies of 10, 15, and 20 Hz. The first inversion at a central frequency of 10 Hz started with the initial model. The other inversions at the central frequencies 15 and 20 Hz were performed by using the inversion results at the lower central frequency as the initial model. During the inversion, S-wave and P-wave velocities were updated using Eq. 5.68.

The inversion results with the central frequency 10 Hz and 15 Hz are shown in Fig. 5.14(a) and (b), respectively. At 10 Hz, the void and the two layers can be clearly characterized by the S-wave velocity profile. Two layers can also be characterized from the P-wave velocity profile, but the void cannot be seen clearly from the P-wave velocity profile. From the inversion results at $15Hz$, the void can be characterized by both S-wave and P-wave velocity profiles. Notice that inversion results at 10 Hz were

used as the initial model for the inversion at 15 Hz.

(a)

(b)
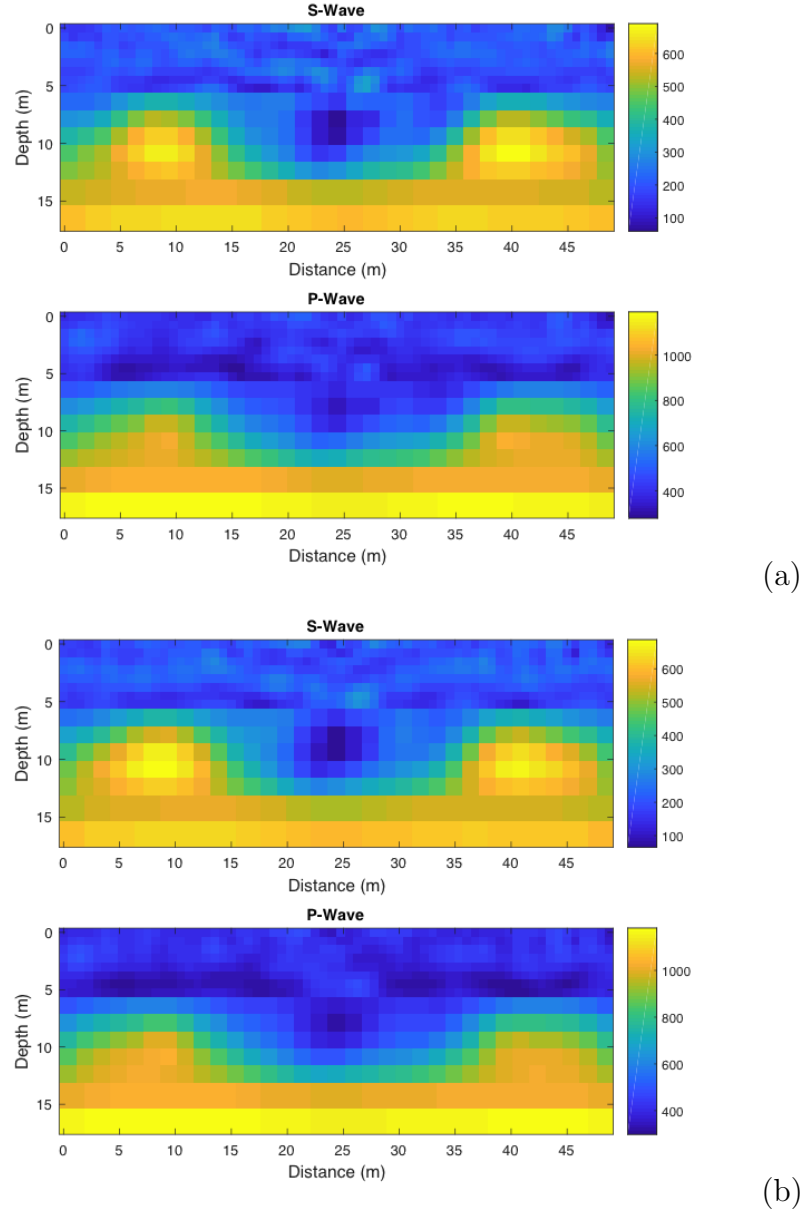
Figure 5.14: The inversion results for S-wave and P-wave velocities at the central frequency (a) 10 Hz and (b) 15 Hz.

Convergence of the iteration method was tested by using the residual between the estimated and observed data. In all inversions, the convergence occurred at 20 iterations. Figure 5.15 shows the estimated and observed waveforms at receiver positions for the inversion at the central frequency at 20 Hz. The residuals at the

receivers are very small due the similar waveform of observed and estimated data.
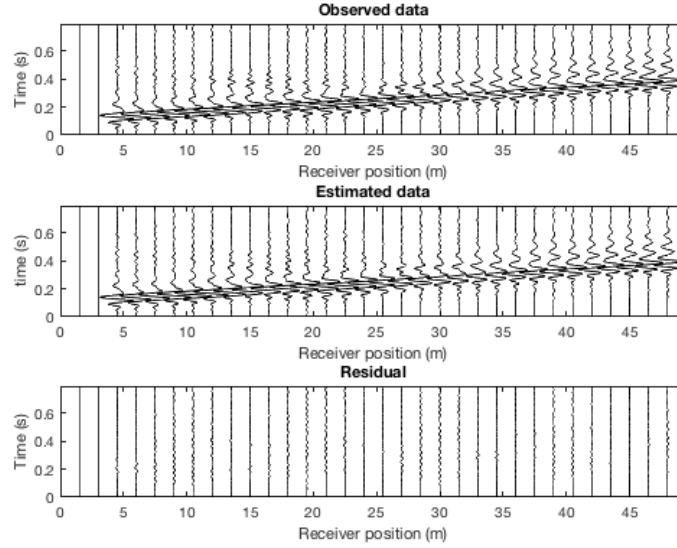
(a)

Figure 5.15: The observed and estimated data for the inversion at the central frequency 20 Hz using the different cell size approach

The normalized least squares error for 20 iterations are shown in Fig. 5.16. One can see the 0.8 order reduction in the error from the 1st iteration to the 20th iteration. After the 20th iteration, the error reached a plateau and results are converged at the 20th iteration.
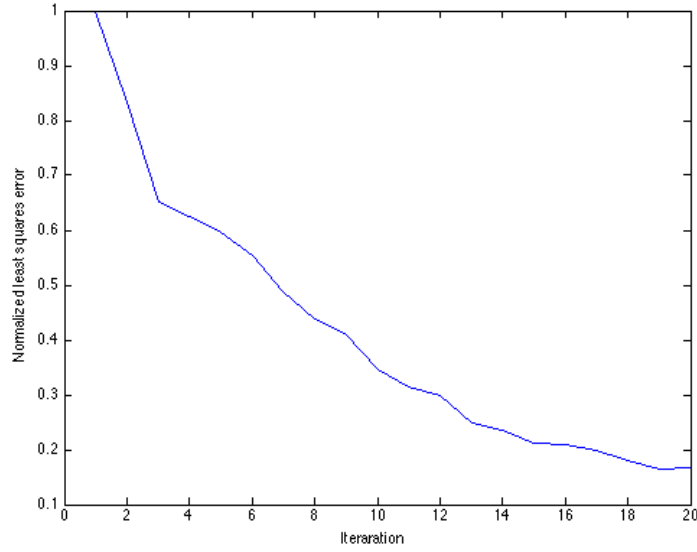
(a)

Figure 5.16: Least square error as a function of integration number at simulations

Computational Efficiency of the Different Cell Size Method

The results of the different cell size method are compared with the regular cell size method used in Ref. [21]. The comparison here is done only to see the accuracy and computational efficiency of the different cell size method. The model updates at 20 Hz from the regular grid method and different cell size method are shown in Fig. 5.17. By comparing both models with the true model, one can accurately identify the void and the soil layers. Moreover, both methods are able to characterize the location, shape, and the S-wave velocity of the void. However, one should notice that the Hessian approximation matrix calculation with regular cell size method took about 3 hours on a Mac computer with a 2.6 GHz processor, while the different cell size method took only about 2.5 hours. For the synthetic model that we considered here, the domain was discretized to have $24 \times 66 = 1584$ cells. Thus the number of parameters in the model is 1584. Since the number of sources multiplied by the number of receivers is 1506, the size of the Jacobian matrix is 1506×1584 and the size of the $H_a = J^T J$ is 1584×1584. When we use our different cell size approach to combine the bottom

127

cells of the domain, the number of cells in the domain was reduced to 814, so the number of parameters of the problem was reduced to 814. With this different cell size method, the size of the $H_a = J^T J$ is 814×814, which is less expensive to calculate. One can see that the size of the H_a has reduced to approximately to $1/4$ of the original H_a matrix. The reduction of the size of H_a depends on the discretization ratio of zone 3 and zone 2 and the decomposition of the domain. For real experiments, usually, the inversion problems are large scale problems. In the 3-D problems, the size of the data sets and the number of parameters of the model are large. The different cell size method is competitive even with high resolutions. For example, consider the case with $100 \times 150 = 15000$ cells, widths of the zone 1, zone 2, zone 3 are 46 m, 24 m, and 30 m, and discretization ratios for zone 1, zone 2, zone 3 are 1,2, and 3. Then the size of the new H_a matrix is 8300×8300. The size of new H_a has reduced approximately to $1/4$ of the original H_a matrix. Thus the differentThe results of the difference cell size method are compared with the regular cell size method used in Ref. [21]. The comparison here is done only to see the accuracy and the computational efficiency of the different cell size method. The model updates at 20 Hz from the regular grid method and different cell size method are shown in Fig. 5.17. By comparing both models with the true model, one can accurately identify the void and the soil layers. Moreover, both methods are able to characterize the location, shape, and the S-wave velocity of the void. However, one should notice that, the Hessian approximation matrix calculation with regular cell size method took about 3 hours on a Mac computer with a 2.6 GHz processor, while the difference cell size method took only about 2.5 hours. For the synthetic model that we considered here, the domain was discretized to have 24×66 =1584 cells. Thus the number of parameters in the model is 1584. Since the number of sources multiplied by the number of receivers is 1506, the size of the Jacobian matrix is 1506×1584 and the size of the $H_a = J^T J$ is 1584×1584. When we use our different cell size approach to combine the bottom cells of the domain, the number of

cells in the domain was reduced to 814, so the number of parameters of the problem was reduced to 814. With this different cell size method, the size of the $H_a = J^T J$ is 814×814, which is less expensive to calculate. One can see that the size of the H_a has reduced to approximately to $1/4$ of the original H_a matrix. The reduction of the size of H_a depends on the discretization ratio of zone 3 and zone 2 and the decomposition of the domain. For real experiments, usually, the inversion problems are large scale problems. In the 3-D problems, the size of the data sets and the number of parameters of the model are large. The difference cell size method is competitive even with high resolutions. For example, consider the case with $100 \times 150 = 15000$ cells, widths of the zone 1, zone 2, zone 3 are 46 m, 24 m, and 30 m, and discretization ratios for zone 1, zone 2, zone 3 are 1,2, and 3. Then the size of the new H_a matrix is 8300×8300. The size of new H_a has reduced approximately to $1/4$ of the original H_a matrix. Thus the difference cell size method is more efficient than the regular grid method and has a good potential for 3-D wave inversion and large scale problems. cell size method is more efficient than the regular grid method and has a good potential for 3-D wave inversion and large scale problems.
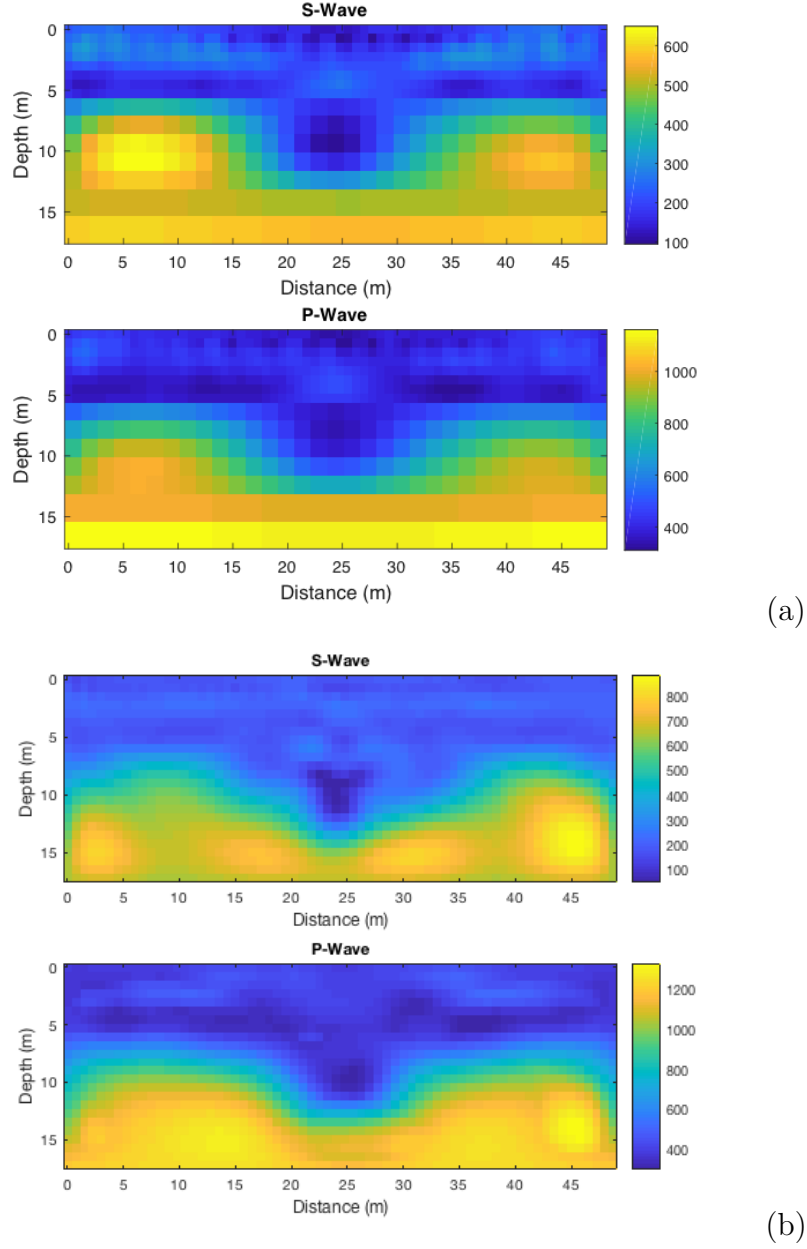
Figure 5.17: The inversion results for S-wave and P-wave velocities at the central frequency 20Hz using (a) the different cell size approach and (b) the regular grid method

Figure 5.18(a) and (b) show the inverted 2-D profiles of S-wave velocity and P-wave velocity variations along the depth, respectively. Blue color curve represents velocity variation with depth in the pre-assumed true model. The observed velocity variation from inversion using the regular method and the different cell method are shown in

green color and purple. The first layer appears from 0 to 8 m depth. The second layer appears from 12 m to 18 m depth. The void is located from 8 m to 12 m depth. The velocity variations from both regular and difference cell size method closely follow the same variations as true model. One can see that two layers, including the void, are clearly characterized by both velocity profiles.
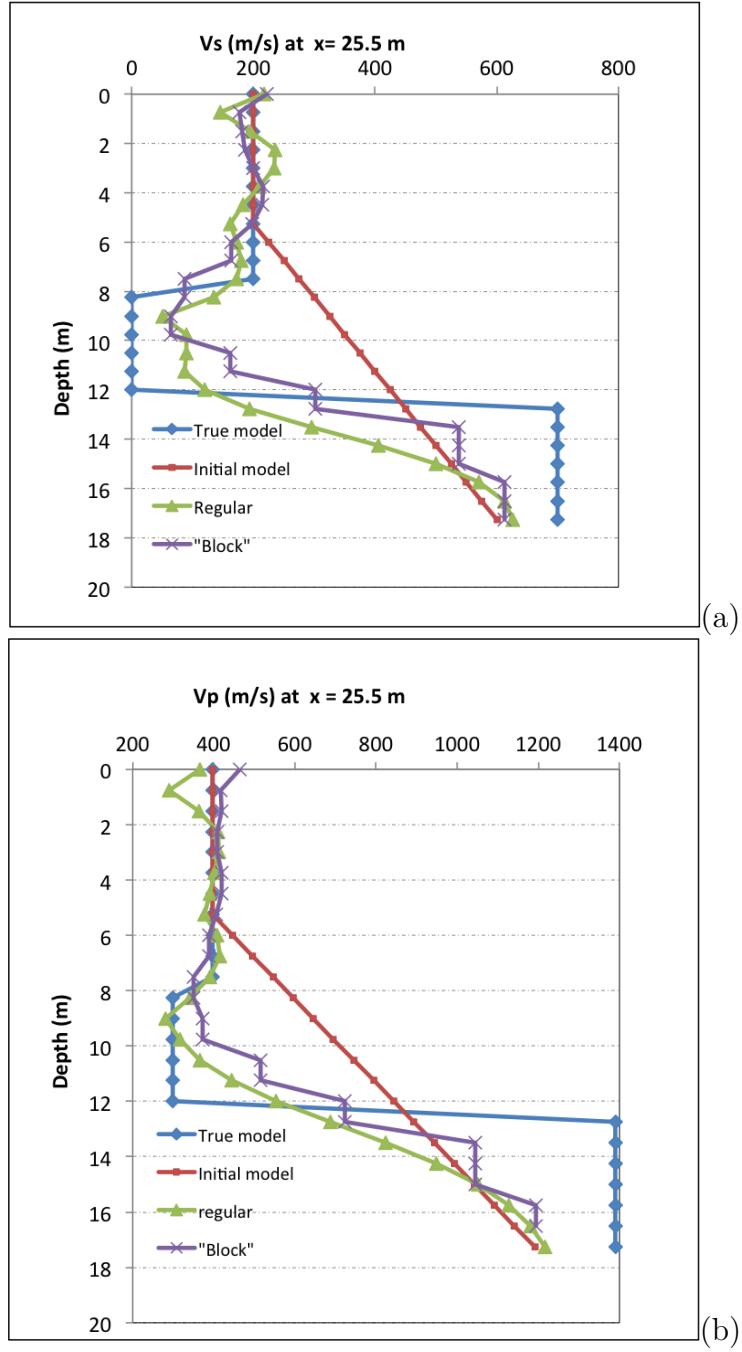
Figure 5.18: The variation of the velocity profile at $x = 25.5$ m (a) S-Wave velocity profile (b) P-Wave velocity profile

5.7   Discussion and Conclusions

In this chapter, full seismic waveform inversion method using the Gauss-Newton method was utilized for detection of embedded sinkholes. The forward problem for simulating seismic wave fields was solved using the velocity-stress staggered-grid finite difference method. A model update of the inversion method was performed with the Gauss-Newton method with the difference cell size method.

One of the major disadvantages of the Gauss-Newton model updating is the large amount of computational and memory required to calculate the Hessian approximation matrix and the Jacobian matrix. To overcome the computation and memory requirements, we used difference cell size approach for storing the Jacobian matrix. The values of the Jacobian, which were obtained using partial derivatives of seismograms with respect to the parameters, at the bottom part of the cells in the domain take smaller values compared with the values of Jacobian at the upper part of the domain. In this approach, the domain is decomposed into three zones according to the values of the Jacobian at the cells. The cells in the bottom of the zones are combined to create larger cells. The Jacobian matrix is then recalculated appropriately.

The results are validated for a synthetic model with an embedded air-filled void. The synthetic model, which consists of two layers of an earth model, is investigated. The inversion at three frequency ranges with central frequencies of 10, 15, and 20 Hz were performed. The void can be characterized from both S-Wave and P-Wave velocities. The computational requirements for both the difference cell size method and the regular cell size method are compared. The difference cell method is able to compute the Hessian with less computational time than required for regular method. In conclusion, the developed approach is well suitable for 3D full wave inversion with other geotechnical conditions.

Chapter 6

A Local Time Mesh Refinement Method for Simulation of Elastic Wave Propagation

The full-wave inversion method that was introduced in chapter 3 is a numerical simulation based method. The accuracy of the results and the efficacy of the method depend on the numerical approaches that were used in seismic wave propagation. In the FWI method, the forward modeling consists of generating synthetic wave fields. In chapter 3, the synthetic wave field is generated by solving 2-D elastic wave equations using the classic velocity-stress staggered-grid finite difference scheme. Simulation of elastic wave equations with small-scale heterogeneities can be done with the classic finite difference approach at small step sizes with uniform grid. However, simulation of a 3-D seismic survey with small-scale heterogeneities is impossible with the classic finite difference approach even on modern supercomputers due to large number of source gatherings and grid points [138]. Therefore, a mesh refinement approach (or multi-grid method) that can be applied to different regions of domain with different step sizes is needed.

Ref. [138] introduced an approach for numerical simulation of wave propagation in media with sub-seismic-scale heterogeneities such as cavities and fractures. Their method is based on local mesh refinement with respect to time and space. The main features of the approach are the use of temporal and spatial refinement on two different surfaces, use of the embedded-stencil technique of grid step with respect to time, and use of the fast Fourier based interpolation to couple variables for spatial mesh refinement.

We adapted the approach introduced in Ref. [138] with some modification. For spatial mesh refinement, Ref. [138] used the fast Fourier based interpolation. However, in this chapter, we modify the technique with cubic smoothing spline interpolation rather than the finite Fourier interpolation for spatial mesh refinement. By using cubic smoothing spline interpolation, we can achieve a better results for wavefield data for the fine grid zone. For the comparison, we simulate a 2-D elastic wave equation with both the modified technique and the technique in Ref. [138]. The results of both methods are compared with uniform mesh method and the cubic smoothing spline interpolation show a significant improvement than the finite Fourier interpolation.

The rest of the chapter is arranged as follows. Section 6.1 presents the modified local mesh refinement method with cubic spline interpolation. The results for 2-D wave propagation are presented in Section 6.2.

6.1 Non-uniform mesh refinement method

In this section, we present the non-uniform mesh refinement method proposed in Ref. [138] with some modification for spatial mesh refinement. Ref. [138] used fast Fourier interpolation for spatial mesh refinement, but here we use cubic spline interpolation.

The domain is categorized into a coarse grid and a fine grid. The coarse grid is the

regular grid that we introduce in Section 5.3.2. Regular grids are considered with integer and half-integer points. The time grid and the spatial grid are denoted by $T^C = \left\{t^N | N = 0, 1/2, 1, ...\right\}$ and $\Omega^C = \{((x)_I, (z)_J) | I = 0, \pm 1/2, \pm 1, ...; J = 0, \pm 1/2, \pm 1, ...\}$, respectively. The grid steps with respect to time and the spatial directions x and z are τ, h_1, and h_3, respectively. The sub-grids are introduced so that they do not intersect with each other. Figure 6.1 shows a sketch of the staggered grid scheme.
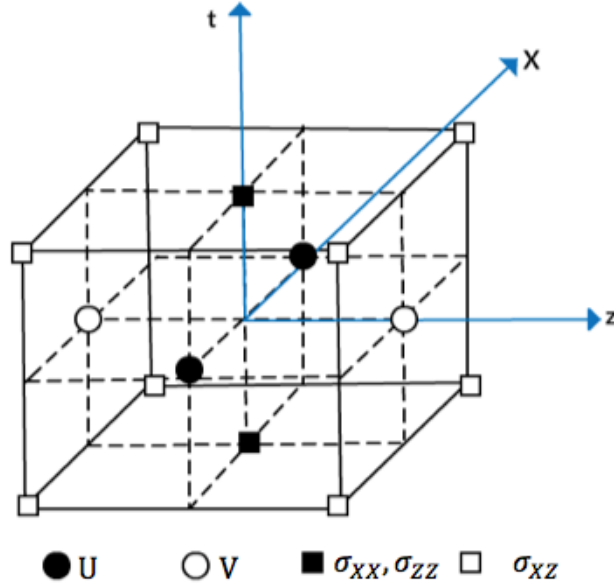
Figure 6.1: The grid structure for the standard staggered grid scheme.

The sub grids in the staggered grid can be introduced as

$$T_\sigma^C = \left\{ t^{n+1/2} | n \in \mathbb{N} \right\}, T_{u,v}^C = \{t^n | n \in \mathbb{N}\} \tag{6.1}$$

$$\Omega_{\sigma_{xx}}^C = \Omega_{\sigma_{zz}}^C = \left\{ \left((x)_i, (z)_j\right) | i \in \mathbb{Z}, j \in \mathbb{Z} \right\}, \tag{6.2}$$

$$\Omega_{\sigma_{xz}}^C = \left\{ \left((x)_{i+1/2}, (z)_{j+1/2}\right) | i \in \mathbb{Z}, j \in \mathbb{Z} \right\}, \tag{6.3}$$

$$\Omega_u^C = \left\{ \left((x)_{i+1/2}, (z)_j\right) | i \in \mathbb{Z}, j \in \mathbb{Z} \right\}, \tag{6.4}$$

$$\Omega_v^C = \left\{ \left((x)_i, (z)_{j+1/2}\right) | i \in \mathbb{Z}, j \in \mathbb{Z} \right\}. \tag{6.5}$$

The fine grid is introduced in such a way that the coarse grid is a subset of the

fine grid. Two sub grids for velocity fields and the stress tensor fields with respect to time in the fine zone are defined. The refinement ratio with respect to time is taken as K.

$$T_\sigma^F = \left\{ t^{n+\frac{1}{2}+\frac{k}{K}} | n \in \mathbb{N}, k = 1, ..., K \right\} \tag{6.6}$$

$$T_{u,v}^F = \left\{ t^{n+\frac{k}{K}} | n \in \mathbb{N}, k = 1, ..., K \right\} \tag{6.7}$$

$$T^F = T_\sigma^F + T_u^F \tag{6.8}$$

The fine grid with respect to space for field variables can be introduced as

$$\Omega_{\sigma_{xx}}^F = \Omega_{\sigma_{zz}}^F = \left\{ \left((x)_{i+l_1/L_1} , (z)_{j+l_3/L_3} \right) | i \in \mathbb{Z}, j \in \mathbb{Z} \right\}, \tag{6.9}$$

$$\Omega_{\sigma_{xz}}^F = \left\{ \left((x)_{i+1/2+l_1/L_1} , (z)_{j+1/2+l_3/L_3} \right) | i \in \mathbb{Z}, j \in \mathbb{Z} \right\}, \tag{6.10}$$

$$\Omega_u^F = \left\{ \left((x)_{i+1/2+l_1/L_1} , (z)_{j+l_3/L_3} \right) | i \in \mathbb{Z}, j \in \mathbb{Z} \right\}, \tag{6.11}$$

$$\Omega_v^F = \left\{ \left((x)_{i+l_1/L_1} , (z)_{j+1/2+l_3/L_3} \right) | i \in \mathbb{Z}, j \in \mathbb{Z} \right\}, \tag{6.12}$$

for $l_1 = 1, ..., L_1$ and $l_3 = 1, ..., L_3$.

$$\Omega^F = \Omega_{\sigma_{xx}}^F + \Omega_{\sigma_{xz}}^F + \Omega_u^F + \Omega_v^F \tag{6.13}$$

where L_1 and L_3 are the refinement ratios with respect to the spatial directions in x and z. The refinement ratios $K, L_1,$ and L_3 are taken to be odd numbers, which ensures the consistency of all sub grids.

The transition zone is introduced when switching from coarse grid to the fine grid. A sketch of the refined grid for the standard staggered grid scheme is shown in Fig.6.2.
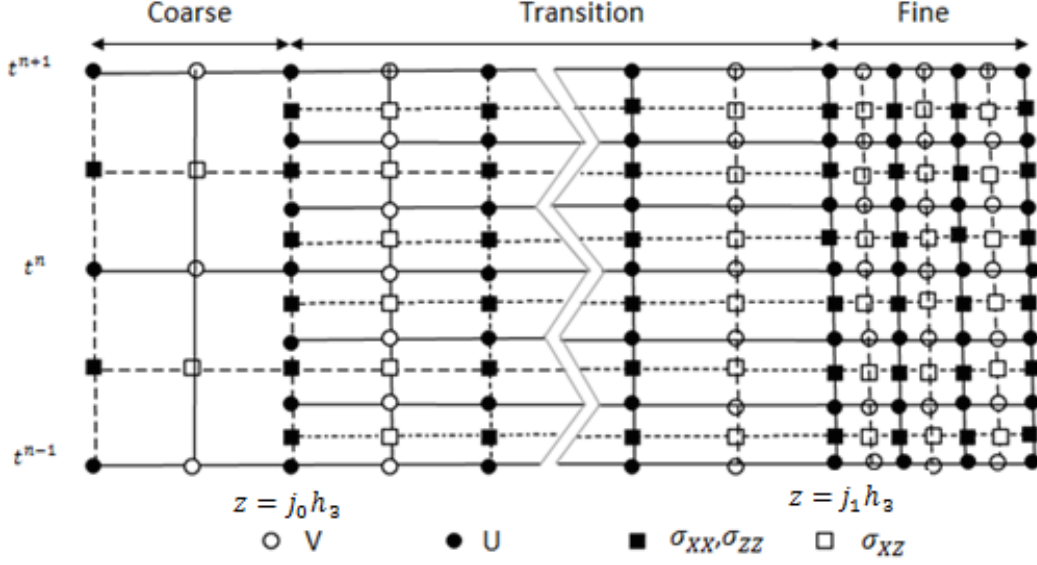
Figure 6.2: A sketch of the refined grid for the standard staggered grid scheme.

The refinements are introduced in the following ranges along the spatial direction z:

- a coarse zone - $z < j_0 h_3$, where j_0 is is an integer. Both time and space are coarse in this zone.

- a transition zone - $j_0 h_3 < z < j_1 h_3$, where j_0 is an integer and j_1 is an half integer. In this zone, coarse grid in space and fine grid in time are used.

- a fine zone - $z < j_1 h_3$. In this zone, both a fine grid in time and space are used.

The grid functions of the field variables can be defined as the cross product of time and the corresponding spatial domains.

6.1.1 Wave equation discretization

The wave equations are discretized by using central finite differences. This approximation scheme has of second order accuracy. The Finite difference operations, which

are defined on the filed variable f for the coarse grid are given by

$$D_t^C [f]_{I,J}^N = \frac{f_{I,J}^{N+1/2} - f_{I,J}^{N-1/2}}{\tau} = \frac{\partial f}{\partial t}|_{I,J}^N + O(\tau^2) \qquad (6.14)$$

$$D_x^C [f]_{I,J}^N = \frac{f_{I+1/2,J}^N - f_{I-1/2,J}^N}{h_1} = \frac{\partial f}{\partial x}|_{I,J}^N + O(h_1^2) \qquad (6.15)$$

$$D_z^C [f]_{I,J}^N = \frac{f_{I,J+1/2}^N - f_{I,J-1/2}^N}{h_3} = \frac{\partial f}{\partial z}|_{I,J}^N + O(h_3^2). \qquad (6.16)$$

Here, f represents $u, v, \sigma_{XX}, \sigma_{ZZ}$, and σ_{XZ}.

The finite difference operations acting on the fine grid are

$$D_t^F [f]_{I,J}^N = \frac{f_{I,J}^{N+1/2K} - f_{I,J}^{N-1/2K}}{\tau/K} = \frac{\partial f}{\partial t}|_{I,J}^N + O(\tau^2) \qquad (6.17)$$

$$D_x^F [f]_{I,J}^N = \frac{f_{I+1/2L_1,J}^N - f_{I-1/2L_1,J}^N}{h_1/L_1} = \frac{\partial f}{\partial x}|_{I,J}^N + O(h_1^2) \qquad (6.18)$$

$$D_z^F [f]_{I,J}^N = \frac{f_{I,J+1/2L_3}^N - f_{I,J-1/2L_3}^N}{h_3/L_3} = \frac{\partial f}{\partial z}|_{I,J}^N + O(h_3^2). \qquad (6.19)$$

In order to obtain bounded solutions, we need to employ the stability criterion

$$\tau \leq \frac{1}{V_{\max}\sqrt{\frac{1}{h_1^2} + \frac{1}{h_3^2}}}, \qquad (6.20)$$

where V_{max} is the maximum of the P-wave velocity. Thus in the transition zone, successive mesh refinement is used. Therefore, the fine grid at time T^F and the coarse spatial grid, Ω^C, are used. The finite difference operations acting on the transition zone are

$$D_t^F [f]_{I,J}^N = \frac{f_{I,J}^{N+1/2K} - f_{I,J}^{N-1/2K}}{\tau/K} = \frac{\partial f}{\partial t}|_{I,J}^N + O(\tau^2) \qquad (6.21)$$

$$D_x^C [f]_{I,J}^N = \frac{f_{I+1/2,J}^N - f_{I-1/2,J}^N}{h_1} = \frac{\partial f}{\partial x}|_{I,J}^N + O(h_1^2) \qquad (6.22)$$

$$D_z^C [f]_{I,J}^N = \frac{f_{I,J+1/2}^N - f_{I,J-1/2}^N}{h_3} = \frac{\partial f}{\partial z}|_{I,J}^N + O(h_3^2) \qquad (6.23)$$

6.1.2 Refinement of Solutions at Interfaces

For a smooth transition from coarse to fine, the transition zone is introduced. At the same time, solutions at the interfaces $z = j_0 h_3$ and $z = j_1 h_3$ should be updated in a special manner for smooth transition. The solutions at the interface $z = j_0 h_3$ are calculated before updating the solutions at the transition zone. At the interface $z = j_0 h_3$, only time need to be fined. Similarly, solutions at the interface $z = j_1 h_3$ are calculated before updating the solutions in the fine zone.

Refinement of temporal steps at the interface $z = j_0 h_3$

In the interface $z = j_0 h_3$, time interval $[t^n, t^{n+1}]$ can be divided as

- $t \in (t^n, t^{n+1/2}]$

- $t \in (t^{n+1/2}, t^{n+1}]$

for an integer n. Figure 6.3 shows the section of the time grid at the interface $z = j_0 h_3$. Then solution is updated separately inside the sub-time interval. Note that the time step in the coarse grid and fine grid are τ and τ/K for a positive, odd integer, K. Since only the temporal refinement occurs in the transition zone, the time step for the transition zone is τ/K.
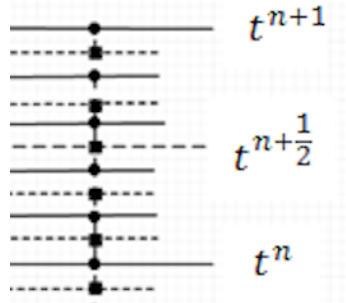
Figure 6.3: A section of the time grid

The time interval $t \in (t^n, t^{n+1/2}]$

Since j_0 is an integer, only the diagonal component of the stress sensors σ_{XX} and σ_{ZZ} are updated at the interface. These stress sensors should be updated at the instances $t^{n+(2k-1)/2K}$ for $k = 1, 2, ..., (K+1)/2$.
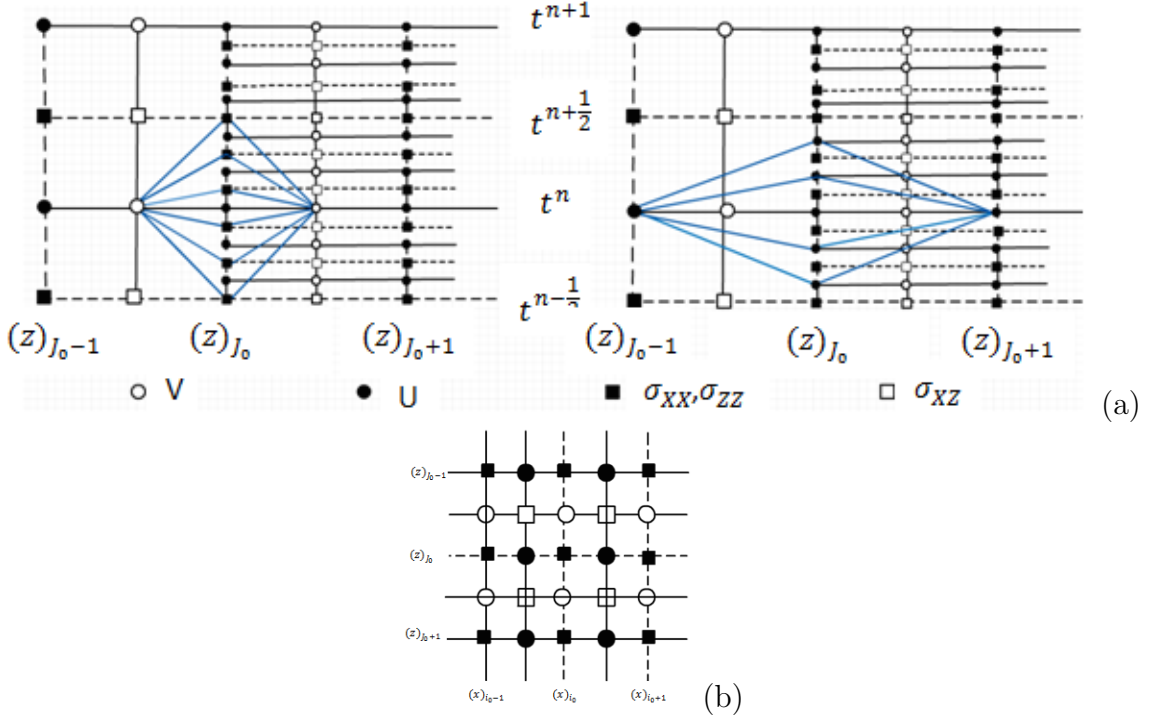
Figure 6.4: 2D (t, z) projection of embedded stencils used to update the solution from the instant t^n to $t^{n+1/2}$. (a) update of stresses at the interface (b) Spatial staggered grid stencil used to update velocity component

Approximations for the stress tensor at the interface $j_0 h_3$ are obtained as

$$\frac{(\sigma_{xx})_{i,J_0}^{n+\frac{2k-1}{K}} - (\sigma_{xx})_{i,J_0}^{n-\frac{2k-1}{K}}}{(2k-1)\frac{\tau}{2K}} = (\hat{\lambda}_{i,J_0} + 2\hat{\mu}_{i,J_0})D_1^C[u]_{i,J_0}^n$$

$$+\hat{\lambda}_{i,J_0}D_3^C[v]_{i,J_0}^n \quad (6.24)$$

$$\frac{(\sigma_{zz})_{i,J_0}^{n+\frac{2k-1}{K}} - (\sigma_{zz})_{i,J_0}^{n-\frac{2k-1}{K}}}{(2k-1)\frac{\tau}{2K}} = \hat{\lambda}_{i,J_0}D_1^C[u]_{i,J_0}^n + (\hat{\lambda}_{i,J_0}$$

$$+2\mu_{i,J_0})D_3^C[v]_{i,J_0}^n \quad (6.25)$$

141

for $k = 1, ..., (K+1)/2$. The velocity vector component is updated at the interface $z = j_0 h_3$ using the finite difference approximation of the equation,

$$\rho \frac{\partial^2 u}{\partial t^2} = \frac{\partial}{\partial x}\left((\lambda + \mu)\frac{\partial u}{\partial x} + \lambda\frac{\partial v}{\partial z}\right) + \frac{\partial}{\partial z}\left(\mu\frac{\partial v}{\partial x} + \mu\frac{\partial v}{\partial z}\right). \tag{6.26}$$

The time interval $t \in (t^{n+1/2}, t^{n+1}]$

In the time interval $t \in (t^{n+1/2}, t^{n+1}]$, the velocity and the stress tensors are updated with the following equations:

$$\hat{\rho}_{i+\frac{1}{2},J_0} \frac{(u)_{i+\frac{1}{2},J_0}^{n+\frac{1}{2}+\frac{2k-1}{2K}} - (u)_{i+\frac{1}{2},J_0}^{n+\frac{1}{2}-\frac{2k-1}{2K}}}{(2k-1)\frac{\tau}{2K}} = D_1^C[\sigma_{xx}]_{i+\frac{1}{2},J_0}^{n+\frac{1}{2}}$$

$$+ D_3^C[\sigma_{zz}]_{i+\frac{1}{2},J_0}^{n+\frac{1}{2}}, \tag{6.27}$$

for $k = 1, ..., (K+1)/2$.

$$\frac{\partial^2 \sigma_{xx}}{\partial t^2} = (\lambda + 2\mu)\frac{\partial}{\partial x}\left(\frac{1}{\rho}\frac{\partial \sigma_{xx}}{\partial x} + \frac{1}{\rho}\frac{\partial \rho_{xz}}{\partial z}\right) + \lambda\left(\frac{1}{\rho}\frac{\partial \sigma_{xz}}{\partial x} + \frac{1}{\rho}\frac{\partial \sigma_{zz}}{\partial z}\right) \tag{6.28}$$

$$\frac{\partial^2 \sigma_{xx}}{\partial t^2} = \lambda\frac{\partial}{\partial x_1}\left(\frac{1}{\rho}\frac{\partial \sigma_{xx}}{\partial x} + \frac{1}{\rho}\frac{\partial \rho_{xz}}{\partial z}\right) + (\lambda + 2\mu)\left(\frac{1}{\rho}\frac{\partial \sigma_{xz}}{\partial x} + \frac{1}{\rho}\frac{\partial \sigma_{zz}}{\partial z}\right) \tag{6.29}$$

142
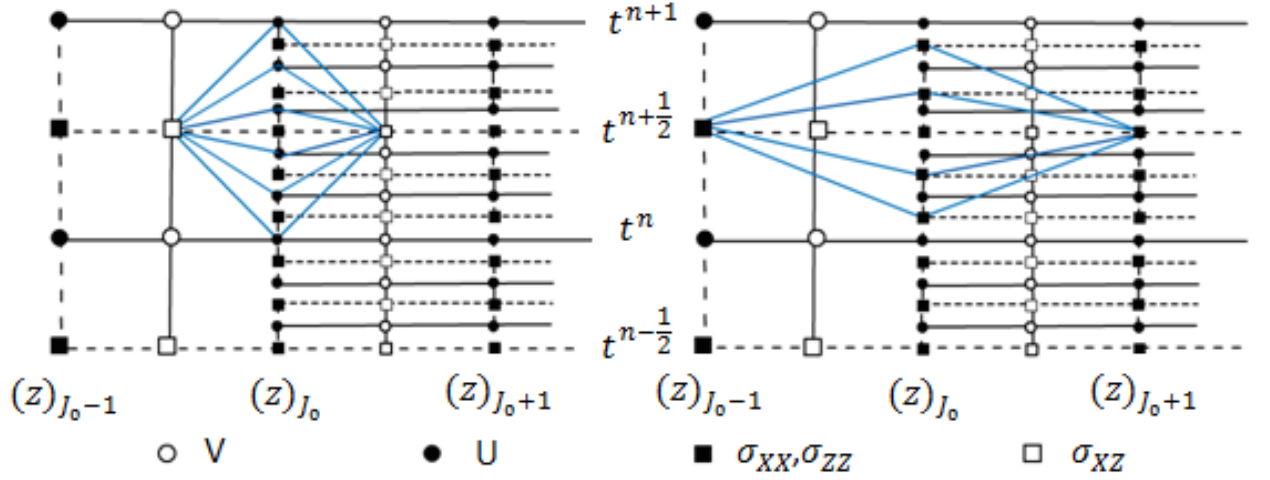
Figure 6.5: 2D (t, z) projection of embedded stencils used to update the solution from the instant $t^{n+1/2}$ to t^{n+1}. Stress component at the interface is updated with the stencil.

Refinement of the spatial steps at the interface, $j_1 h_3$

The interface $j_1 h_3$ appears between the transition zone and the fine grid zone. Notice that j_1 is a half-integer number. The step size of the spatial direction in the transition zone are h_1 and h_3. Also, space grid in the transition zone is a coarse grid. Thus the step sizes of the fine grid are taken as $h_1/L1$ and h_3/L_3 where L_1 and L_2 are refinement ratios in the x and z direction. To update the solution at the interface $j_1 + \frac{1}{2L_3}$ from the coarse to the fine grid, the following equations are obtained using the finite-difference approximation.

$$\hat{\rho}^N_{I,J_1+\frac{1}{2L_3}} D^F_t [v]^N_{I,J_1+\frac{1}{2L_3}} = D^F_1 [\sigma_{xz}]^N_{I,J_1+\frac{1}{2L_3}}$$

$$+ D^F_3 [\tilde{\sigma}_{zz}]^N_{I,J_1+\frac{1}{2L_3}} \tag{6.30}$$

$$D_t^F[\sigma_{xz}]_{I,J_1+\frac{1}{2L_3}}^N = \hat{\mu}_{I,J_1+\frac{1}{2L_3}}^N \left(D_1^F[v]_{I,J_1+\frac{1}{2L_3}}^N \right.$$

$$\left. + D_3^F[\tilde{u}]_{I,J_1+\frac{1}{2L_3}}^N \right), \tag{6.31}$$

In the above equations, $\sigma_{\tilde{Z}Z}$ and $\tilde{u}$ indicates that the up sampling of the variables σ_{ZZ} and u is required along the interface $j_1 h_3$. These components are defined on the line $z = j_1 h_3$ as shown in Fig. 6.6. Thus the 1D interpolation is needed to get these components in the fine grid due to the shift of the grids. Ref. [138] applied a fast Fourier transform for the interpolation. However, we use the cubic smoothing spline [24, 139] for the interpolation.
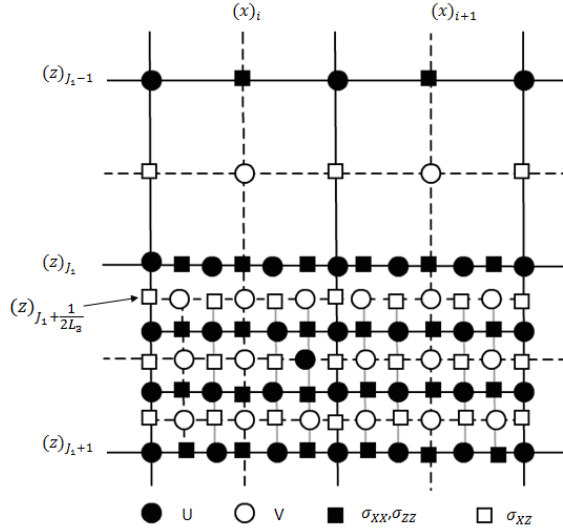
Figure 6.6: The grid of the spatial mesh refinement interface $(x_3)_{J_1}$.

6.1.3 Cubic smoothing spline Interpolation

For a given a set of co-ordinates (x_i, y_i), for $i = 1, 2, ..., n$ of a function $y = f(x)$, a cubic spline finds a curve that connects the gap between the two adjacent points (x_j, y_j) and (x_{j+1}, y_{j+1}). The cubic spline approach uses cubic functions S_i, $i = 1, 2, .., n-1$ and their first and second derivatives.

The cubic function can be expressed as

$$S_i(x) = a_i(x - x_i)^3 + b_i(x - x_i)^2 + c_i(x - x_i) + d_i, \qquad (6.32)$$

where $x_i \leq x \leq x_{i+1}$.

In the case of interests of smoothness, one can consider the coordinates of the data given by

$$y_i = f(x_i) + \epsilon_i, \qquad (6.33)$$

where ϵ_i, $i = 0, 1, ..., n$ represents the noise of the curve and a random variable with variance σ_i^2. Thus the spline is smoothed. The function $f(x)$ can be obtained by constructing a spline function, $S(x)$, which minimizes the function

$$L = \lambda \sum_{i=0}^{n} \left(\frac{y_i - S_i}{\sigma_i}\right)^2 + (1 - \lambda) \int_{x_0}^{x_n} \left(S''(x)\right)^2 dx, \qquad (6.34)$$

where $S_i = S(x_i)$ and λ is the smoothing parameter or penalty for the roughness of the function.

Here, the first term considers reducing the error between the spline and the data points. So the spline should come reasonably close to the data. The second term considers the low curvature of the spline. Thus the smoothing spline Eq. 6.34 produces a spline that balances these two opposing criteria.

Figure 6.7 shows a cubic interpolating spline and a smoothing spline for a given set of coordinates [24]. The dotted line represents the cubic interpolating spline and the solid line represents the cubic smoothing spline. One can see that the cubic interpolating spline is passing through the given set of spline whereas the smoothing spline does not.
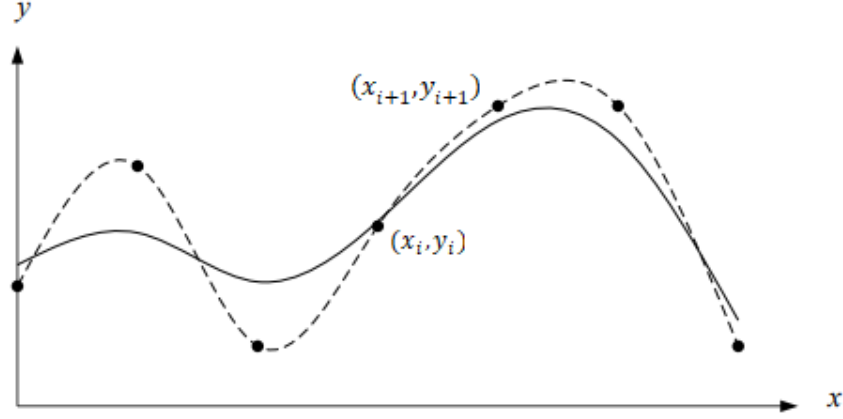
Figure 6.7: Example for a cubic interpolating spline and cubic smoothing spline. The dotted line represents the cubic interpolating spline and the solid line represents the cubic smoothing spline (photo credit: [24]).

We implement the above refinement procedure with the defined boundary conditions in Eqs. 5.35 - 5.37 and the initial condition in Eq. 5.53 together with the stability criterion 6.20.

6.2 Wave Propagation Results

In this section, we present the wave propagation results from the above method. A numerical study was conducted with 2-D domain of size 50 m × 50 m. Step sizes in the spatial directions in the regular grid are taken as $h_1 = h_3 = 0.5$. Thus a 100×100 regular mesh in the spatial domain is created. The time step τ is calculated with the stability criterion (Eq. 6.20) using the maximum P- wave velocity. The shear wave velocity V_s of the medium was considered as 200 m/s. The pressure wave velocity V_p was calculated using the defined shear wave velocity and the formula

$$V_p = V_s \sqrt{\left(\frac{2\left(1 - \nu\right)}{1 - 2\nu} \right)}, \tag{6.35}$$

146

where $\nu = 0.33$ is used in the numerical calculations. The density of the medium is considered to be 1800 m/s. A source was located at the grid point (1,50) in the spatial domain. 20 receivers were positioned in the domain with the 2.5 m spacing on the surface. Thus, the source was placed 24 m away from the first receiver.

The time refinement and spatial refinement ratios are as $K, L_1, L_3 = 3$. A refinement area in the grid was considered from 6m to 15m in the z direction. Accordingly, the coarse zone, transition zone, and fine grid zone are defined in Table 6.1 and Fig. 6.8.

Table 6.1: Grid cells breakdown in the grid zones

grid zone	grid cells
coarse	1-10
transition	10-12
fine	12-30
transition	30-32
coarse	32-100
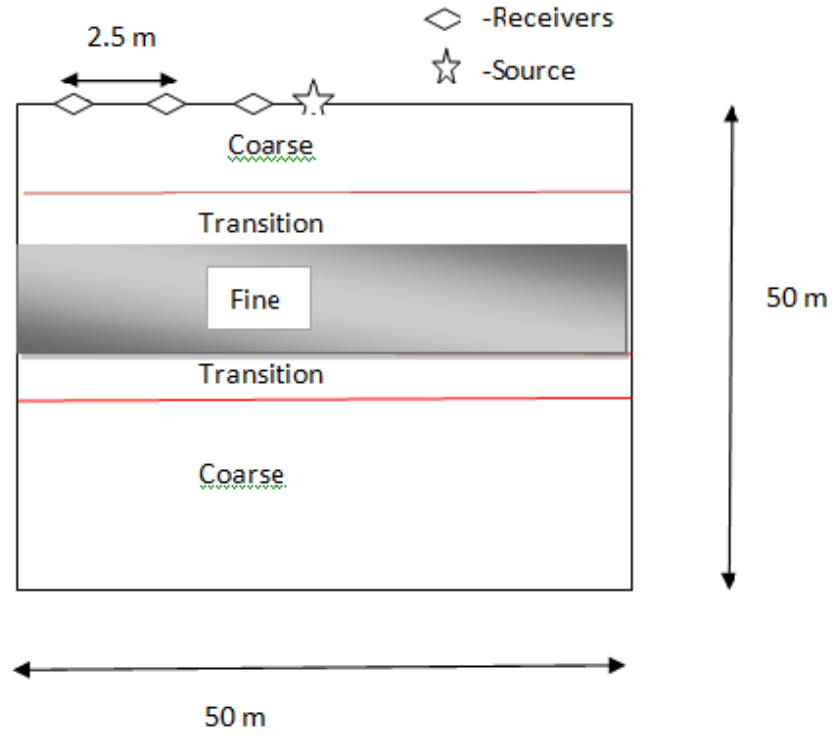
Figure 6.8: Grid cells breakdown

Here, we introduced two transition zones. The first transition zone appears when the wave propagates from coarse to fine and the second transition zone appears when the wave propagates from fine to coarse grid zone.

The wave fields were obtained from the classic finite difference approach using the uniform mesh and the mesh refinement approach (non uniform mesh) to see the accuracy of the presented method. Figure 6.9 shows the wave fields obtained at three depths, 0.5m, 6.5 m, and 16.5 m depths at the receivers. Note that these three depths are positions in the coarse grid (before the transition zone to the fine grid), fine grid, and coarse grid (after the transition zone to the fine grid), respectively.

148
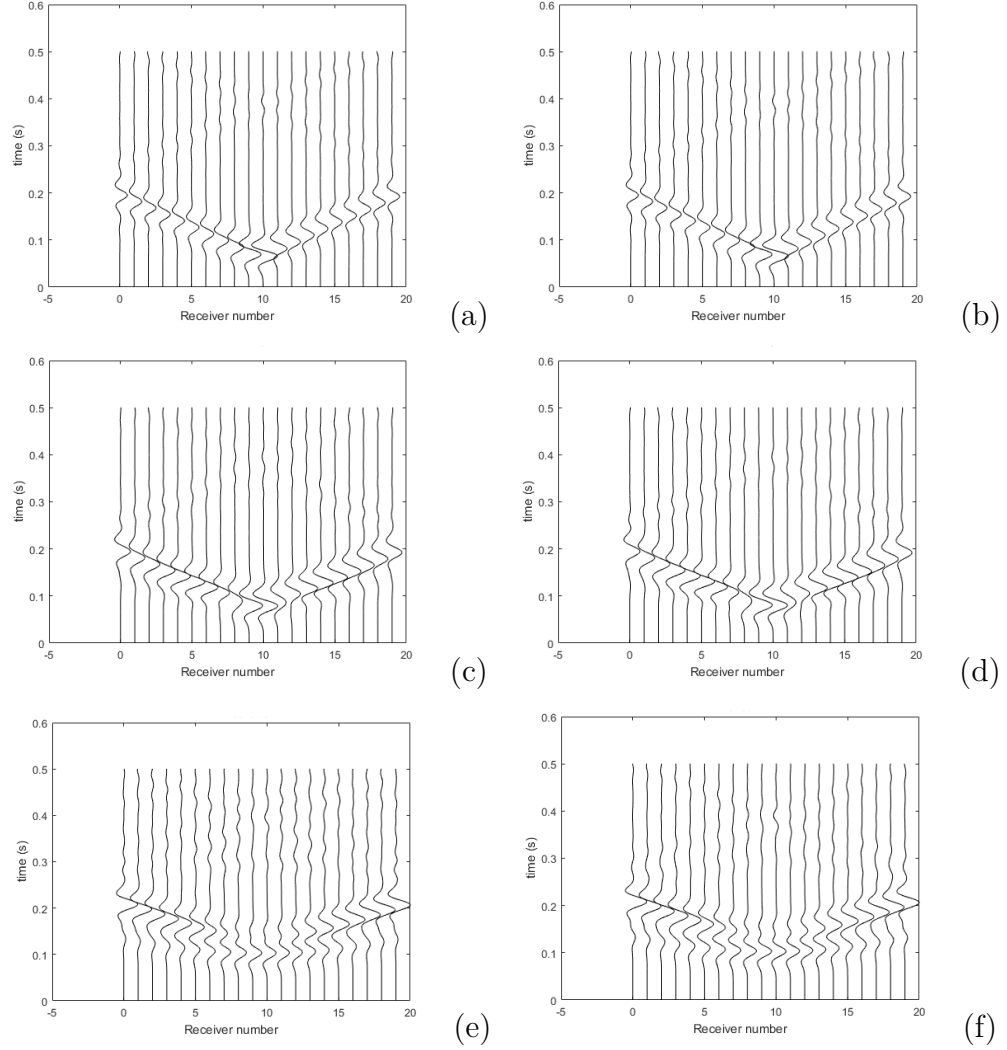
Figure 6.9: Wave fields from the mesh refinement method (non uniform mesh) at (a) 0.5 m depth, (c) 6.5 m depth, and (e) 16.5 m depth. Wave propagation from the uniform mesh at (b) 0.5 m depth, (d) 6.5 m depth, and (f) 16.5 m depth.

Figure 6.9 shows the estimated wave field at receivers. Figure 6.9 (a),(c), and (e) corresponding to the observed wavefield data from the mesh grid method and Fig. 6.9 (b),(d), and (f) correspond to the estimated field data from the classic finite difference method. One can see that results from both methods are the same at receivers at the same depth. However, an advantage of the mesh refinement method is the ability of simulation real models with small-scale heterogeneities. In this study, we only consider the ability to estimate wavefield data from the mesh refinement method.

149

Also, the mesh refinement method is able to be applied with different refinement ratios at different surfaces. In this case, the fine grid zone has the refinement ratios of $L_1 = L_3 = 3$ for x, z directions. The step sizes in the fine grid zone are $h_1/L_1 = 1/6$ and $h_3/L_3 = 1/6$. Thus the coarse grid zone and the fine grid zone behave as two layers and the mesh refinement is applied only to one layer, which contains small-scale heterogeneities.

Moreover, we compare the computational efficiency of the non-uniform mesh method with the uniform grid method at a smaller step size in spatial directions. The number of cells in the spatial domain for the two methods are shown in Table 6.2. For example, if the uniform mesh method is used with step size $1/6$ (refinement ratio $L_1 = L_3 = 3$) in the x and z directions, the number of grid points in the spatial domain is 90000. However, the spatial domain of the non-uniform mesh refinement method contains only 24400 grid points. Thus less memory storage is required with non-uniform mesh method than the uniform mesh method.

Figure 6.10 shows the number of grid points in the spatial domain as a function of refinement ratio. The blue color curve represents the number of cells required for the non-uniform mesh method and the red color curve represents the number of cells required for the uniform mesh method. One can see that there are eight orders of magnitude increment in the number of cells with uniform mesh method. However, only 1.5 orders of magnitude increment in the number of cells with the non-uniform mesh method. Therefore, Non-uniform mesh method required less storage even with higher refinement ratio.

Table 6.2: Domain size of the non uniform mesh method and the uniform grid method at the spatial directions

Refinement Ratio	Number of cells (uniform mesh method)	Number of cells (non-uniform mesh method)
$L_1 = L_3 = 3$ (step size $=1/6$)	90000	24400
$L_1 = L_3 = 5$ (step size $=1/10$)	250000	53200

On the other hand, the less computational time is required to generate the wave field using non-uniform mesh method on the same standard computer. In the uniform mesh method, when the refinement ratio increases, Matlab encounters memory problem. This time difference brings the possibility of being applied to the FWI method presented in Chapter 5 for 3-D large scale problems with small-scale heterogeneities.
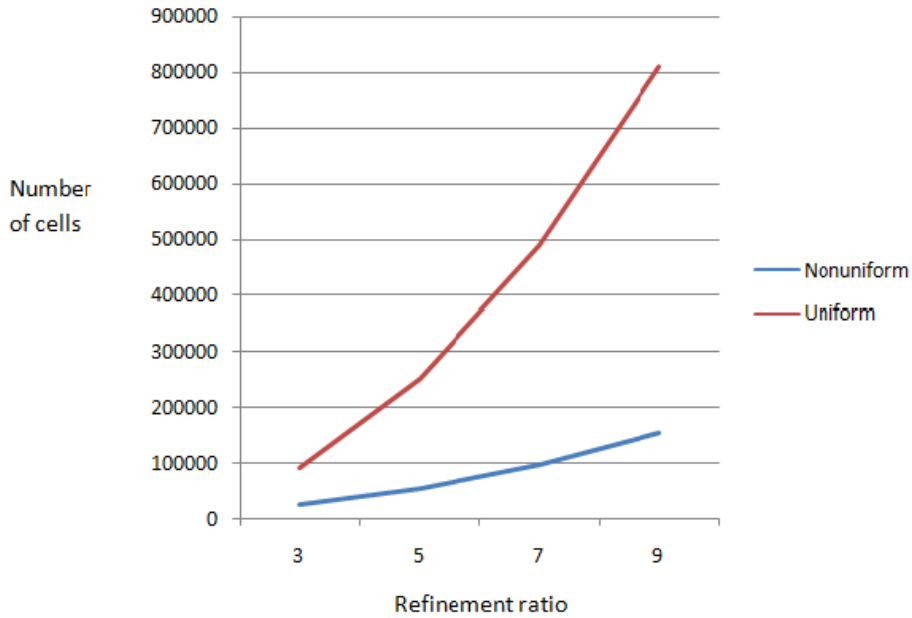
Figure 6.10: Number of cells as a function of refinement ratio.

Figure 6.11 shows the wave fields at four receivers at the 6.5m depth using the cubic smoothing spline interpolation method and the finite Fourier transformation method. At the 6.5m depth, the wave propagates in the fine grid area. Thus the

spatial mesh refinement is needed. The wave field results using two interpolation methods are compared with the results from the uniform mesh method. Note that we assume the uniform mesh method gives accurate wave field solutions. Figure 6.11 shows the estimated wave fields only at receiver 6, 9, 12, and 15. Blue, red, and black color curves represent the wave fields using FFT interpolation, cubic smoothing spline interpolation, and the uniform mesh method (without spatial mesh refinement). One can see that, a good agreement between the results from the cubic smoothing spline interpolation and uniform mesh method. However, the solutions with FFT interpolation overestimated the wavefield data.
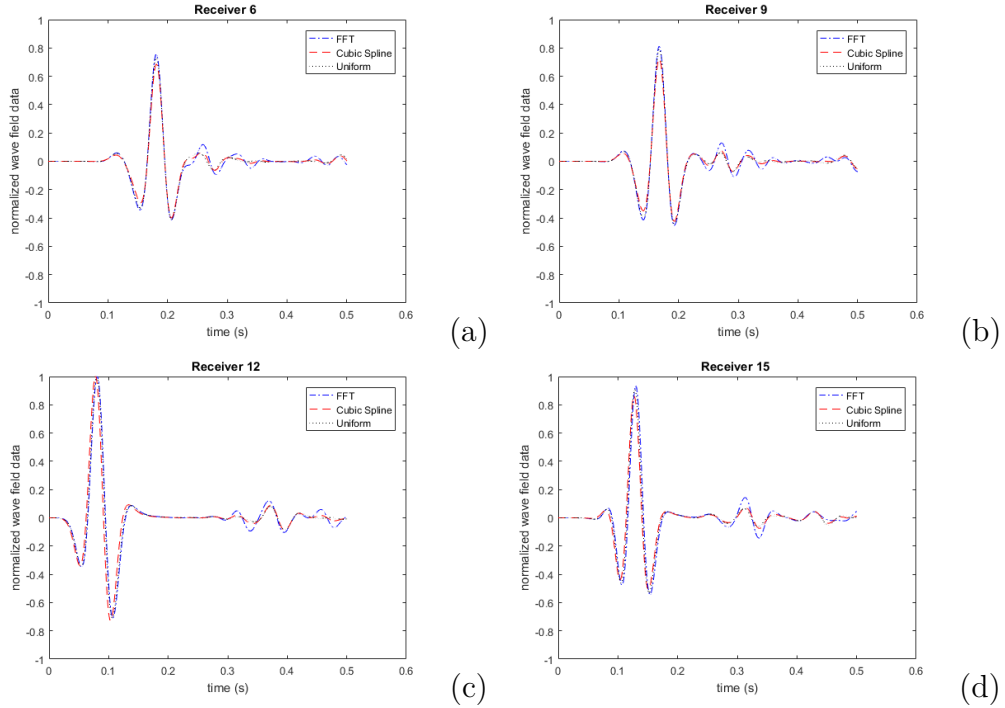
Figure 6.11: Comparison between wave fields generated by fast Fourier interpolation and cubic smoothing spline interpolation.

We calculated the l_2 norm error of the field data with cubic smoothing spline and FFT interpolation. Table 6.3 shows the l_2 norm error of the two interpolation methods relative to the uniform mesh method at four receivers 6, 9, 12, and 15. Cubic smoothing spline gives less error in the wave field estimation than FFT interpolation.

Table 6.3: l_2 norm error of the estimated wave field data using FFT interpolation and cubic smoothing interpolation for spatial mesh refinement

Receiver	Error (FFT interpolation)	Error (Cubic smoothing spline interpolation)
6	0.55	0.33
9	0.52	0.39
12	0.65	0.51
15	0.65	0.51

6.3   Conclusions

In this chapter, we adopted a method for numerical simulation of wave propagations in media with small scale heterogeneities such as cavities and fractures. This method is introduced by Ref. [138] and is based on local mesh refinement with respect to both time and space in different media. One of the main features of their method is the use of fast Fourier transform based interpolation for spatial mesh refinement. We modified this step by using cubic smoothing spline interpolation instead fast Fourier transform. The technique was developed using central finite difference approximation.

We presented numerical results for the simulation of seismic wave propagation. The results using the mesh refinement method are compared with a classic finite difference approximation scheme with a uniform mesh. The results of the mesh refinement approach show a good agreement with the results of the wave propagation with the classic finite difference scheme with uniform grid. The advantage of the mesh refinement method is the capability of the simulations of 3-D large scale problems in media with small scale heterogeneities.

Moreover, results for the wave propagation using the cubic smoothing spline interpolation and fast Fourier interpolation are compared. The mesh refinement method with cubic smoothing spline approach provides better results for wave propagation. Overall, the local time-space mesh refinement approach with the cubic smoothing spline interpolation will be a good candidate for 3-D FWI problem as the ability of

the simulation of small scale heterogeneities in different surfaces for large scale problems. In the future, we plan to perform numerical simulations of seismic waves in 3-D heterogeneous media.

Chapter 7

Future Work

One of the challenges of identifying and localizing damages in complex structures is developing non destructive damage detection techniques by considering computational efficiency. In this thesis, we developed two approaches. One approach is based on information theoretic methods for damage detection in complex dynamical structures, such as bridges. That approach is based on mutual information and is called Optimal Mutual Information Interaction (oMII). We discussed the efficiency of this approach using a benchmark problem in Chapter 3 and successfully applied the technique for damage detection in bridge structures in Chapter 4. We intend to use this technique together with machine learning techniques for predictions of earthquakes. This ongoing work is discussed in Section 7.1.

The other approach is based on Full Wave Inversion (FWI) of seismic wave propagation to detect anomalies in engineering structures and subsurfaces. We addressed some issues, such as the computational and memory requirements of a recently developed FWI approach, which uses the Gauss-Newton method. Efficiency of the technique was discussed Chapter 5. In chapter 6, we adapted a refinement mesh grid approach for simulation of 2D seismic wave propagation with small-scale heterogeneities. Section 7.2 discusses some possible extensions on these approaches.

7.1 Application for Earthquake Prediction

Prediction of earthquakes generally refers to identifying the location, size, and time of the event. Identifying the earthquakes early will result in minimizing the loss of life and property damages. Earthquakes, including aftershocks, can be predicable to some extent. However, earthquake prediction is a difficult problem due to unreachability of the Earth for observation. Therefore, earthquake predictions are an interesting and challenging problem among seismologists. [140–144].

7.1.1 Background

Earthquakes are usually caused when two plates collide or move in different directions. The underground rocks break along a fault and a sudden release of energy causes seismic waves, which make the ground shake [25]. The size of an earthquake depends on the size of the fault and the amount of the slip of the fault. Figure 7.1 shows the situation in which two blocks of the Earth slip past one another.
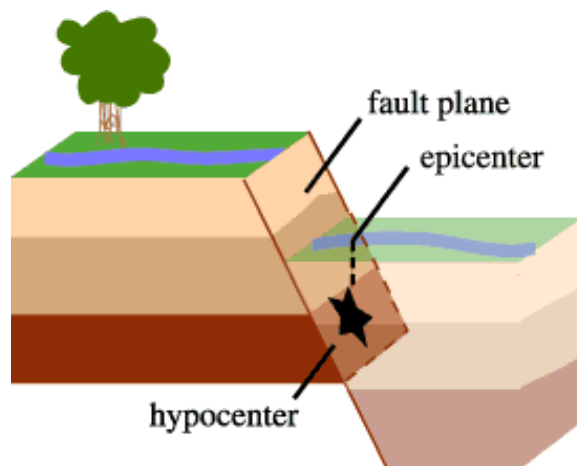
Figure 7.1: Two plates are moving in different directions (photo credit: Ref. [25]).

An earthquake may have foreshocks and aftershocks. The smaller earthquakes that happen in the same place before the main earthquake are called foreshocks. The aftershocks happens after the main shock. Aftershocks can continue for years after

the mainshock, depending on the size of the mainshock. Thus, predicting aftershocks is another goal among the seismologists[144].

Earthquakes are recorded by instruments called seismographs. The size of an earthquake can be detected using the seismogram recordings on seismographs. However, it is unlikely that scientist can predict earthquakes correctly. There are many researchers have been trying to predict the earthquakes with different approaches [140]. For example, Ref. [141] presents an earthquake prediction method based on variation of seismic velocities. They discovered that a large precursory change in seismic body-wave velocities occurred before the earthquake in San Fernando, California in February 1971. Based on further experiments, authors conclude that velocity variations show significant promise as earthquake precursors. Moreover, they show that P-wave velocity variation is greater than the S-wave velocity. This indicates important implication for the course of future investigation because the time of arrival of P-waves is easier to measure than that of S-waves.

Some discussions and reviews on statistical approaches to earthquake prediction have also done in the past [142]. Ref. [143] develops a quantitative analysis of earthquake prediction involving economics. The authors in Ref. [143] formulate the earthquake prediction problem as an optimal control problem and founded an optimal strategy by minimizing the total expected losses for maintaining alerts costs and for changing alerts costs.

Ref. [145] uses a statistical procedure to identify a foreshock sequence while it is in progress. This method is derived from a theoretical model of fracture growth. The authors show that, as a predictor, the procedure reduces the average uncertainty in the rate of occurrence for a future strong earthquake by a factor of more than 1000 when compared with the Poisson rate of occurrence. They conclude that using this statistical approach, about one-third of all main shocks with local magnitude greater than or equal to 4.0 in central California can be predicted.

Recently, aftershock patterns following large earthquakes are studied in Ref. [144]. They use a deep-learning approach to identify a static-stress-based criterion that forecast aftershock locations. Results show that this machine-learning-driven approach provides improved forecasts of aftershock locations.

7.1.2 Methods: Spatial Pairwise Mutual Information

Observations over the past years motivate the idea that earthquake events that happened around the world have a dynamic relation between the regions. The purpose of the analysis of earthquakes by information flow is to compare the effects for the events with smaller magnitude and the events with larger magnitudes region wise. Therefore, the events are categorized into three categories according to the size of earthquakes and information flow between three categories in regions are measured pairwise using MI. We discuss the categorization of regions separately later in this section.

MI information finding approach that we used in Chapter 3 uses known or assumed probability distribution of variables. However, for this particular application, we plan to estimate MI between categories using k-nearest neighbor statistics [146]. The idea of finding MI from k-nearest neighbor statistics was introduced by Alexander Kraskov, Harald Stobauer, and Peter Grassberger in 2004. We briefly summarized the idea introduced in Ref. [146] for finding MI between two random variables.

Let $Z = (X, Y)$ be a space where X and Y are two random variables. For some metrics given on the spaces spanned by X, Y, the neighbors for each point $z_i = (x_i, y_i)$ are defined by the maximum norm distance formula

$$d_{i,j} = ||z_i - z_j|| = \max\{||x_i - x_j||, ||y_i - y_j||\}.$$

In this formula any norms can be used for calculating $||x_i - x_j||$ and $||y_i - y_j||$.

However, in this application we use a "geographical distance measure" along the surface of the Earth, which uses geographical coordinates in terms of latitude and longitude. Also, the distance from z_i to its kth nearest neighbor is taken as $\epsilon(i)/2$ and defined by

$$\epsilon(i) = \max\{\epsilon_x(i), \epsilon_y(i)\}, \tag{7.1}$$

where $\epsilon_x(i)/2$ and $\epsilon_y(i)/2$ are the distance between the corresponding points projected into the X and Y subspaces. The MI estimate formula using the average distance to nearest neighbors is

$$I(X, Y) = \psi(k) - \langle\psi(n_x + 1) + \psi(n_y + 1)\rangle + \psi((N), \tag{7.2}$$

where ψ is the digamma function, $\psi = \Gamma(x)^{-1} \frac{d\Gamma(x)}{dx}$, which satisfies

$$\phi(x + 1) = \psi(x) + \frac{1}{x} \tag{7.3}$$

and $\psi(1) = -C$, where $C \approx 0.577$ is the Euler-Mascheroni constant. $n_x(i)$ are the number of points x_i whose distance from x_i is strictly less than $\epsilon(i)/2$. $n_y(i)$ can also be defined in the same manner. $\langle\cdot\rangle$ indicates the averaging both over i and over all realizations of the random samples.

Data Classification Method

It is interesting research goal to find whether earthquakes can trigger other earthquakes on the opposite side of the earth. We plan to analyze the earthquakes events between spatially distributed regions. This classification of the land geographically into regions should be done before analyzing the effects between earthquakes with different magnitudes. We plan to use k-means clustering, which is a machine learning algorithm, to classify the observation data into clusters.

7.1.3 Data Description

For this study, real time earthquakes data downloaded from the United States Geological Survey website was used. Parameters such as magnitude, longitude, latitude, depth, time, and location are recorded daily when the event occurs. The data was collected for the earthquakes that happened during 1970-2018 in the world. Magnitude is the most common measure of an earthquake's size. Typical values of magnitude are in the range -1, 10. However, for this study events with magnitude [2.5,10] are considered.
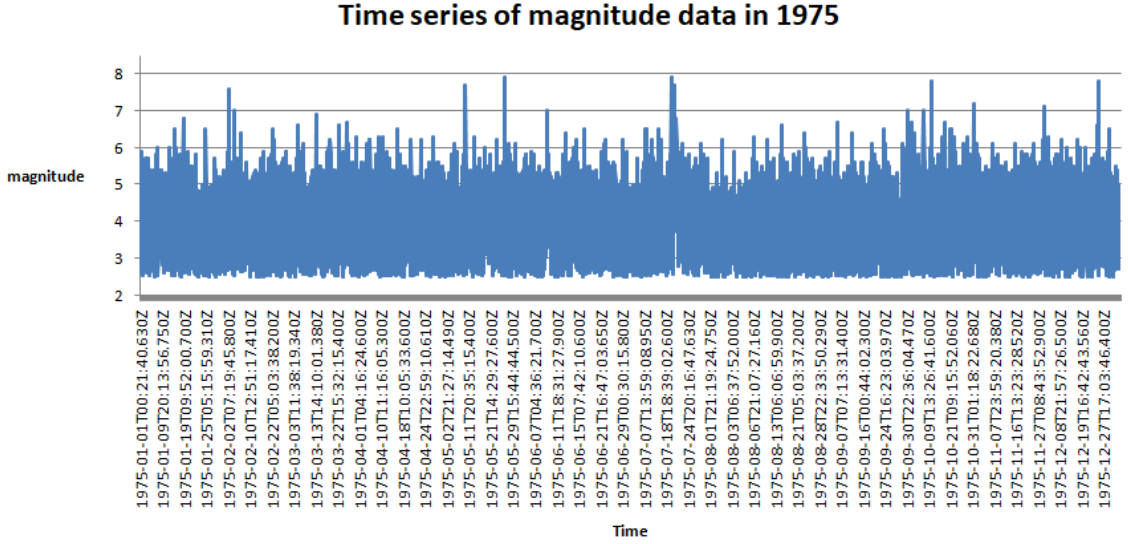
Figure 7.2: The magnitudes of the earthquakes that happened in 1975

For instance, Figure 7.2 shows the magnitudes of the events that happened in the world in 1975. During 1975, the event with the maximum magnitude happened in Azores-Cape St. Vincent Ridge in May 26 at 9.11 am and the size of the magnitude is 7.9 (Richter Scale). The latitude and longitude of this location are 35.997 and -17.649, respectively. The total number of earthquakes that happened in the world during 1975 was 7030.
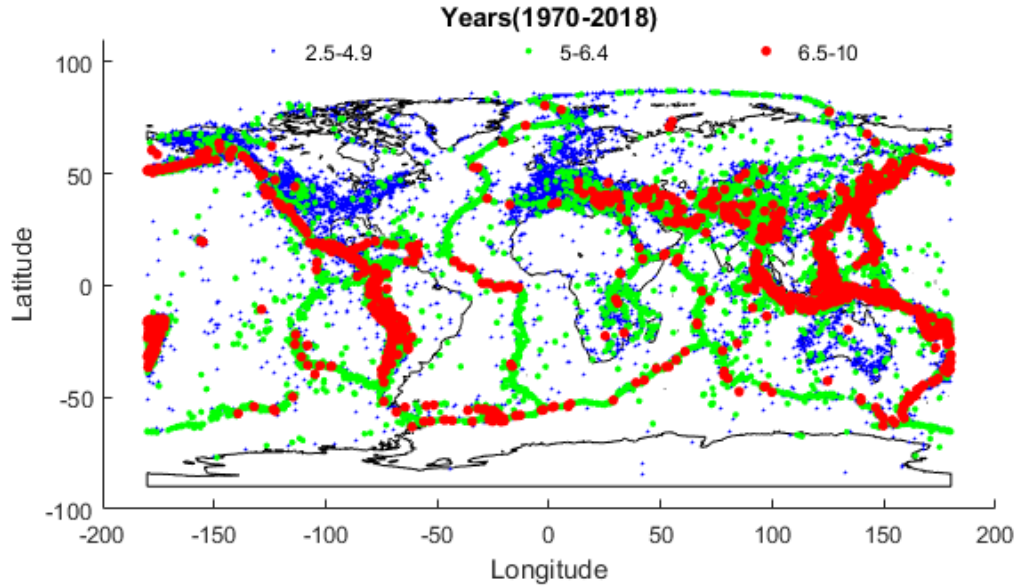
Figure 7.3: The locations of the earthquakes that happened during the period 1970-2018. The earthquakes only with the magnitude greater than 2.5 are shown and categorized into three according to the size of the magnitude.

The spatial distribution of magnitudes for the events that happened during the time period 1970-2018 are shown in Fig. 7.3. The events are divided into three categories according to their magnitudes. Blue, green, and red dots correspond to the earthquakes with magnitudes 2.5-4.9, 5-6.4, and 6.5-10, respectively.

7.1.4 Some Basic Results

The k-mean clustering algorithm is used to classify the geographical region. Figure 7.4 shows the 5 clusters of the world according to the locations of the earthquake events that happened between 1970-2018. Ongoing work considers selecting an optimal number of clusters that classify the geographical region according to the location of the earthquake events.
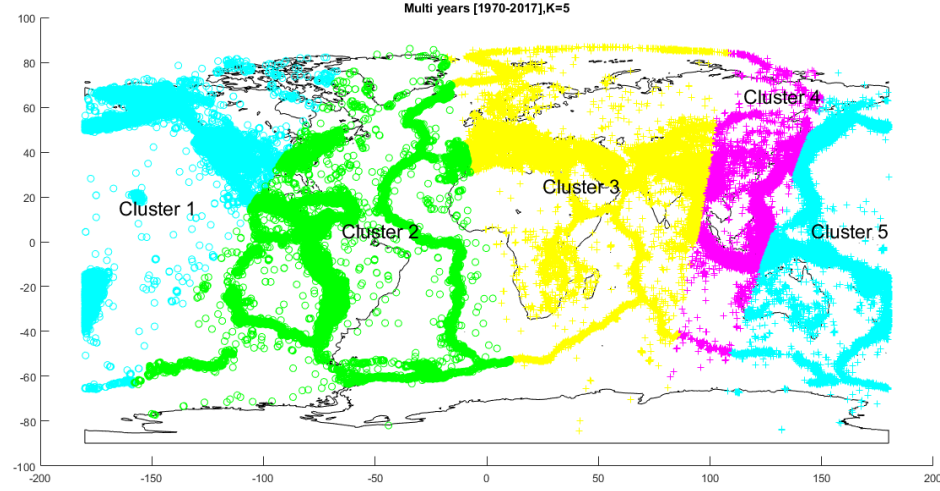
Figure 7.4: Spatial clustering of the earthquakes using k-mean clustering algorithm

The earthquake events that happened in each cluster again divided into three categories according to the size of the earthquakes. The earthquakes with magnitude 2.5-4.9, 5-6.4, and 6.5-10 are labeled as small, medium, and large. Then the number of earthquake that happened in a week are divided for small, medium, and large magnitude categories. In this way we identified 15 variables for 5 clusters. Pair-wise interactions between these variables are calculated using MI between variables.

For the basic analysis we calculated MI between variables using the most straightforward and widespread approach: discrete probability estimation using histograms [146]. The data of the variables are partitioned into bins of finite size and using the frequencies of each bins, entropy, joint entropy, and MI are approximated.

Figure 7.5 shows MI connections between variables. MI values are categorized into three ranges and the connections are presented using three colors. Blue lines, red lines, and black lines represents the MI values 0-0.5, 0.5-0.8, and greater than 0.8, respectively. We can see that there are some strong connections between large earthquake, medium, and small earthquakes categories in each clusters. For example, in cluster 3, there is a strong connection between the large earthquake group and the medium size earthquake group. Also, one can see a strong connection between the

earthquakes in cluster 1 and cluster 4.

Our ongoing work considers finding MI using the k-nearest neighbor algorithm with geographical distance. Then the oMII algorithm can be used to distinguish the indirect and the direct interactions. Thus, in the future, more analysis will be performed to see if events with large magnitude are associated with the occurrence of events with the smaller magnitude and to see whether earthquakes can trigger other earthquakes on the opposite side of the earth.
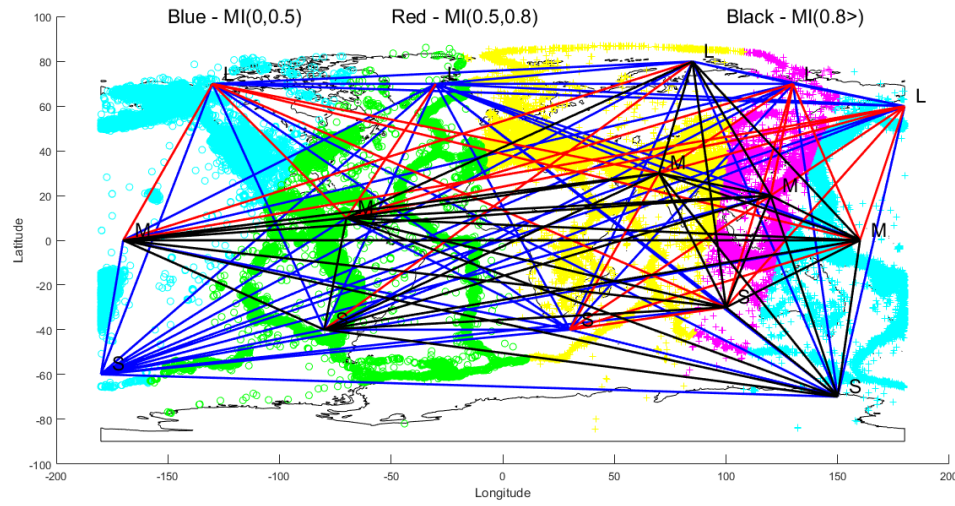
Figure 7.5: MI connections between 15 variables

7.2 Future Works on Full Waveform Analysis

There are many ways to extend the initial work of 2-D analysis of full seismic wavefields. The results of FWI with difference cell size method, which was introduced in Chapter 5, showed the capability of locating void and characterizing soil/ rock layers for a synthetic model of the earth. In future, we plan to test the method using real experimental data for several engineering applications such as soil and rock characterization, sinkhole detection, and unknown foundation elements.

Also, we plan to extend this work for analysis of 3-D full seismic wavefields for

sinkhole detection. The 2-D analysis of full seismic wavefields are able to identify sinkhole and characterize soil/rock layers. However, in real engineering applications it may require significant field testing effort in locating sinkholes. Thus we plan to use FWI with difference cell size approach and the mesh refinement approach discussed in Chapter 6 for the analysis of 3-D full seismic wavefields.

Bibliography

[1] A. Morassi, F. Vestroni, Dynamic methods for damage detection in structures, Springer Science & Business Media, 2008.

[2] https://windsorstar.com/news/local-news/wind-turbine-topples-in-chatham-kent.

[3] https://en.wikipedia.org/wiki.

[4] http://newsfeed.time.com/2013/04/18/watch-massive-sinkhole-in-chicago-swallows-three-cars.

[5] https://www.smithsonianmag.com/science-nature/science-behind-floridas-sinkhole-epidemic-180969158.

[6] Introduction to nondestructive testing, The american society for nonddestructive testing.

[7] R. Adams, P. Cawley, C. Pye, B. Stone, A vibration technique for non-destructively assessing the integrity of structures, Journal of Mechanical Engineering Science 20 (2) (1978) 93–100.

[8] J.-T. Kim, N. Stubbs, Crack detection in beam-type structures using frequency data, Journal of Sound and Vibration 259 (1) (2003) 145–160.

[9] Z. Shi, S. Law, L. Zhang, Damage localization by directly using incomplete mode shapes, Journal of engineering mechanics 126 (6) (2000) 656–660.

[10] L. Hadjileontiadis, E. Douka, Crack detection in plates using fractal dimension, Engineering Structures 29 (7) (2007) 1612–1625.

[11] J. Ko, C. Wong, H. Lam, Damage detection in steel framed structures by vibration measurement approach, in: Proceedings-SPIE the International Society for Optical Engineering, SPIE INTERNATIONAL SOCIETY FOR OPTICAL, 1994, pp. 280–280.

[12] A. Pandey, M. Biswas, M. Samman, Damage detection from changes in curvature mode shapes, Journal of sound and vibration 145 (2) (1991) 321–332.

[13] M. A. Wahab, G. De Roeck, Damage detection in bridges using modal curvatures: application to a real damage scenario, Journal of Sound and Vibration 226 (2) (1999) 217–235.

[14] E. Figueiredo, G. Park, C. R. Farrar, K. Worden, J. Figueiras, Machine learning algorithms for damage detection under operational and environmental variability, Structural Health Monitoring 10 (6) (2011) 559–572.

[15] I. Trendafilova, M. P. Cartmell, W. Ostachowicz, Vibration-based damage detection in an aircraft wing scaled model using principal component analysis and pattern recognition, Journal of Sound and Vibration 313 (3-5) (2008) 560–566.

[16] https://www.canadiangeographic.ca.

[17] https://www.cnn.com.

[18] N. O. Mariita, et al., The gravity method, 001045504.

[19] https://web.hku.hk.

[20] http://www.geometrics.com.

[21] K. T. Tran, M. McVay, Site characterization using gauss–newton inversion of 2-d full seismic waveform in the time domain, Soil Dynamics and Earthquake Engineering 43 (2012) 16–24.

[22] https://cmontalto.wordpress.com.

[23] G. Williams, Linear algebra with applications, Jones & Bartlett Learning, 2017.

[24] D. Pollock, et al., Smoothing with cubic splines (1993).

[25] https://earthquake.usgs.gov.

[26] S. W. Doebling, C. R. Farrar, M. B. Prime, et al., A summary review of vibration-based damage identification methods, Shock and vibration digest 30 (2) (1998) 91–105.

[27] J.-T. Kim, N. Stubbs, Improved damage identification method based on modal information, Journal of Sound and Vibration 252 (2) (2002) 223–238.

[28] C. R. Farrar, D. A. Jauregui, Comparative study of damage identification algorithms applied to a bridge: I. experiment, Smart materials and structures 7 (5) (1998) 704.

[29] W. Fan, P. Qiao, Vibration-based damage identification methods: a review and comparative study, Structural health monitoring 10 (1) (2011) 83–111.

[30] K. K. Tseng, L. Wang, Impedance-based method for nondestructive damage identification, Journal of engineering mechanics 131 (1) (2005) 58–64.

[31] O. Salawu, Detection of structural damage through changes in frequency: a review, Engineering structures 19 (9) (1997) 718–723.

[32] E. P. Carden, P. Fanning, Vibration based condition monitoring: a review, Structural health monitoring 3 (4) (2004) 355–377.

[33] P. Cawley, R. D. Adams, The location of defects in structures from measurements of natural frequencies, The Journal of Strain Analysis for Engineering Design 14 (2) (1979) 49–57.

[34] J. Penny, D. Wilson, M. Friswell, Damage location in structures using vibration data, in: PROCEEDINGS-SPIE THE INTERNATIONAL SOCIETY FOR OPTICAL ENGINEERING, SPIE INTERNATIONAL SOCIETY FOR OPTICAL, 1993, pp. 861–861.

[35] C. R. Farrar, S. W. Doebling, An overview of modal-based damage identification methods, in: Proceedings of DAMAS conference, Citeseer, 1997, pp. 269–278.

[36] L. Wenjin, X. Jiajian, S. Ward, Effectiveness of the high-precision gravity method in detecting sinkholes in taian railway station of shandong province, Geotechnical and environmental geophysics 3 (1990) 169–174.

[37] http://zonge.com.

[38] M. Van Schoor, Detection of sinkholes using 2d electrical resistivity imaging, Journal of Applied Geophysics 50 (4) (2002) 393–399.

[39] https://ground.geophysicsgpr.com.

[40] R.-E. Plessix, Introduction: Towards a full waveform inversion, Geophysical Prospecting 56 (6) (2008) 761–763.

[41] J. Virieux, S. Operto, An overview of full-waveform inversion in exploration geophysics, Geophysics 74 (6) (2009) WCC1–WCC26.

[42] K. T. Tran, M. McVay, M. Faraone, D. Horhota, Sinkhole detection using 2d full seismic waveform tomographysinkhole detection by fwi, Geophysics 78 (5) (2013) R175–R183.

[43] A. Sudu Ambegedara, J. Sun, K. Janoyan, E. Bollt, Information-theoretical noninvasive damage detection in bridge structures, Chaos: An Interdisciplinary Journal of Nonlinear Science 26 (11) (2016) 116312.

[44] M. D. Seale, B. T. Smith, W. Prosser, Lamb wave assessment of fatigue and thermal damage in composites, The Journal of the Acoustical Society of America 103 (5) (1998) 2416–2424.

[45] K.-Y. Jhang, Nonlinear ultrasonic techniques for nondestructive assessment of micro damage in material: a review, International journal of precision engineering and manufacturing 10 (1) (2009) 123–135.

[46] C. R. Farrar, S. W. Doebling, D. A. Nix, Vibration–based structural damage identification, Philosophical Transactions of the Royal Society of London A: Mathematical, Physical and Engineering Sciences 359 (1778) (2001) 131–149.

[47] https://www.electrical4u.com.

[48] A. Morassi, Identification of a crack in a rod based on changes in a pair of natural frequencies, Journal of Sound and Vibration 242 (4) (2001) 577–596.

[49] M. Friswell, J. Penny, D. Wilson, Using vibration data and statistical measures to locate damage in structures, Modal Analysis: The International Journal of Analytical and Experimental Modal Analysis 9 (4) (1994) 239–254.

[50] G. C. Pardoen, Effect of delamination on the natural frequencies of composite laminates, Journal of composite materials 23 (12) (1989) 1200–1215.

[51] A. Messina, E. Williams, T. Contursi, Structural damage detection by a sensitivity and statistical-based method, Journal of sound and vibration 216 (5) (1998) 791–808.

[52] N. Stubbs, R. Osegueda, Global non-destructive damage evaluation in solids, International Journal of Analytical and Experimental Modal Analysis 5 (1990) 67–79.

[53] W. Wang, A. Zhang, Sensitivity analysis in fault vibration diagnosis of structures, in: International Modal Analysis Conference, 5 th, London, England, 1987, pp. 496–501.

[54] N. Stubbs, T. H. Broome, R. Osegueda, Nondestructive construction error detection in large space structures, AIAA journal 28 (1) (1990) 146–152.

[55] D. Sanders, Y. Kim, N. Stubbs, Nondestructive evaluation of damage in composite structures using modal parameters, Experimental Mechanics 32 (3) (1992) 240–251.

[56] M. H. Richardson, M. Mannan, Remote detection and location of structural faults using modal parameters, in: 10th International Modal Analysis Conference, Vol. 1, 1992, pp. 502–507.

[57] R. Mayes, Error localization using mode shapes: An application to a two link robot arm, Tech. rep., Sandia National Labs., Albuquerque, NM (United States) (1991).

[58] L. Hadjileontiadis, E. Douka, A. Trochidis, Fractal dimension analysis for crack identification in beam structures, Mechanical Systems and Signal Processing 19 (3) (2005) 659–674.

[59] M. J. Katz, Fractals and the analysis of waveforms, Computers in biology and medicine 18 (3) (1988) 145–156.

[60] G.-Q. Li, K.-C. Hao, Y. Lu, S.-W. Chen, A flexibility approach for damage identification of cantilever-type structures with bending and shear deformation, Computers & structures 73 (6) (1999) 565–572.

[61] C.-P. Fritzen, D. Jennewein, T. Kiefer, Damage detection based on model updating methods, Mechanical systems and signal processing 12 (1) (1998) 163–186.

[62] C. Zang, M. Imregun, Structural damage detection using artificial neural networks and measured frf data reduced via principal component projection, Journal of sound and vibration 242 (5) (2001) 813–827.

[63] A. Aktan, K. Lee, C. Chuntavan, T. Aksel, Modal testing for structural identification and condition assessment of constructed facilities, in: Proceedings-spie the International Society for Optical Engineering, SPIE INTERNATIONAL SOCIETY FOR OPTICAL, 1994, pp. 462–462.

[64] A. Pandey, M. Biswas, Damage detection in structures using changes in flexibility, Journal of sound and vibration 169 (1) (1994) 3–17.

[65] K. Worden, A. Lane, Damage identification using support vector machines, Smart Materials and Structures 10 (3) (2001) 540.

[66] N. G. Hairston Jr, N. G. Hairston Sr, Cause-effect relationships in energy flow, trophic structure, and interspecific interactions, The American Naturalist 142 (3) (1993) 379–411.

[67] E. Bullmore, O. Sporns, Complex brain networks: graph theoretical analysis of structural and functional systems, Nature Reviews Neuroscience 10 (3) (2009) 186.

[68] N. Guelzim, S. Bottani, P. Bourgine, F. Képès, Topological and causal structure of the yeast transcriptional regulatory network, Nature genetics 31 (1) (2002) 60.

[69] M. Morjaria, F. Santosa, Monitoring complex systems with causal networks, IEEE Computational Science and Engineering 3 (4) (1996) 9–10.

[70] https://www.angelo.edu.

[71] C. A. Sims, Money, income, and causality, The American economic review 62 (4) (1972) 540–552.

[72] R. K. Kaufmann, D. I. Stern, Evidence for human influence on climate from hemispheric temperature relations, Nature 388 (6637) (1997) 39.

[73] P. Duan, F. Yang, T. Chen, S. L. Shah, Direct causality detection via the transfer entropy approach, IEEE transactions on control systems technology 21 (6) (2013) 2052–2066.

[74] C. W. Granger, Time series analysis, cointegration, and applications, American Economic Review 94 (3) (2004) 421–425.

[75] J. L. Melsa, A. P. Sage, An introduction to probability and stochastic processes, Courier Corporation, 2013.

[76] V. J. Easton, J. H. McColl, Statistics glossary v1. 1.

[77] K. Hlaváčková-Schindler, M. Paluš, M. Vejmelka, J. Bhattacharya, Causality detection based on information-theoretic approaches in time series analysis, Physics Reports 441 (1) (2007) 1–46.

[78] Y. Chen, G. Rangarajan, J. Feng, M. Ding, Analyzing multiple nonlinear time series with extended granger causality, Physics Letters A 324 (1) (2004) 26–35.

[79] G. Sugihara, R. May, H. Ye, C.-h. Hsieh, E. Deyle, M. Fogarty, S. Munch, Detecting causality in complex ecosystems, science (2012) 1227079.

[80] P.-O. Amblard, O. Michel, The relation between granger causality and directed information theory: A review, Entropy 15 (1) (2013) 113–143.

[81] M. Alencar, Information theory.

[82] C. E. Shannon, A mathematical theory of communication, ACM SIGMOBILE mobile computing and communications review 5 (1) (2001) 3–55.

[83] C. Blomberg, Physics of life: the physicist's road to biology, Elsevier, 2007.

[84] S. Goldman, Information theory.

[85] C. E. Shannon, A mathematical theory of communication, Bell System Tech. J. 27 (1948) 379–423, 623–656.

[86] T. M. Cover, J. A. Thomas, Elements of Information Theory, 2nd Edition, John Wiley & Sons, 2006.

[87] E. E. Schadt, J. Lamb, X. Yang, J. Zhu, S. Edwards, D. GuhaThakurta, S. K. Sieberts, S. Monks, M. Reitman, C. Zhang, et al., An integrative genomics approach to infer causal associations between gene expression and disease, Nature genetics 37 (7) (2005) 710.

[88] W. Liao, J. Ding, D. Marinazzo, Q. Xu, Z. Wang, C. Yuan, Z. Zhang, G. Lu, H. Chen, Small-world directed networks in the human brain: multivariate granger causality analysis of resting-state fmri, Neuroimage 54 (4) (2011) 2683–2694.

[89] B. Genge, I. Kiss, P. Haller, A system dynamics approach for assessing the impact of cyber attacks on critical infrastructures, International Journal of Critical Infrastructure Protection 10 (2015) 3–17.

[90] J. Sun, D. Taylor, E. M. Bollt, Causal network inference by optimal causation entropy, SIAM Journal on Applied Dynamical Systems 14 (1) (2015) 73–106.

[91] C. L. Farrow, M. Shaw, H. Kim, P. Juhás, S. J. Billinge, Nyquist-shannon sampling theorem applied to refinements of the atomic pair distribution function, Physical Review B 84 (13) (2011) 134105.

[92] E. Constantinos, http://www.chem.uoa.gr.

[93] J. Sun, E. M. Bollt, Causation entropy identifies indirect influences, dominance of neighbors and anticipatory couplings, Physica D: Nonlinear Phenomena 267 (2014) 49–57.

[94] J. L. Fleiss, B. Levin, M. C. Paik, Statistical methods for rates and proportions, John Wiley & Sons, 2013.

[95] C. R. Farrar, K. Worden, An introduction to structural health monitoring, Philosophical Transactions of the Royal Society of London A: Mathematical, Physical and Engineering Sciences 365 (1851) (2007) 303–315.

[96] J.-T. Kim, Y.-S. Ryu, H.-M. Cho, N. Stubbs, Damage identification in beam-type structures: frequency-based method vs mode-shape-based method, Engineering structures 25 (1) (2003) 57–67.

[97] A. Alvandi, C. Cremona, Assessment of vibration-based damage identification techniques, Journal of sound and vibration 292 (1) (2006) 179–202.

[98] P. J. Cruz, R. Salgado, Performance of vibration-based damage detection methods in bridges, Computer-Aided Civil and Infrastructure Engineering 24 (1) (2009) 62–79.

[99] R. Sampaio, N. Maia, J. Silva, Damage detection using the frequency-response-function curvature method, Journal of Sound and Vibration 226 (5) (1999) 1029–1042.

[100] A. Dutta, S. Talukdar, Damage detection in bridges using accurate modal parameters, Finite Elements in Analysis and Design 40 (3) (2004) 287–304.

[101] J. J. Lee, J. W. Lee, J. H. Yi, C. B. Yun, H. Y. Jung, Neural networks-based damage detection for bridges considering errors in baseline finite element models, Journal of Sound and Vibration 280 (3) (2005) 555–578.

[102] M. Mehrjoo, N. Khaji, H. Moharrami, A. Bahreininejad, Damage detection of truss bridge joints using artificial neural networks, Expert Systems with Applications 35 (3) (2008) 1122–1131.

[103] S. Barai, P. Pandey, Performance of the generalized delta rule in structural damage detection, Engineering Applications of Artificial Intelligence 8 (2) (1995) 211–221.

[104] S. Barai, P. Pandey, Time-delay neural networks in damage detection of railway bridges, Advances in Engineering Software 28 (1) (1997) 1–10.

[105] J. Sun, E. M. Bollt, Causation entropy identifies indirect influences, dominance of neighbors and anticipatory couplings, Physica D 267 (2014) 49.

[106] J. Sun, C. Cafaro, E. M. Bollt, Identifying coupling structure in complex systems through the optimal causation entropy principle, Entropy 16 (2014) 3416.

[107] A. M. Fraser, H. L. Swinney, Independent coordinates for strange attractors from mutual information, Physical review A 33 (2) (1986) 1134.

[108] W. M. Wells, P. Viola, H. Atsumi, S. Nakajima, R. Kikinis, Multi-modal volume registration by maximization of mutual information, Medical image analysis 1 (1) (1996) 35–51.

[109] R. Battiti, Using mutual information for selecting features in supervised neural net learning, IEEE Transactions on neural networks 5 (4) (1994) 537–550.

[110] J. P. Pluim, J. A. Maintz, M. A. Viergever, Mutual-information-based registration of medical images: a survey, IEEE transactions on medical imaging 22 (8) (2003) 986–1004.

[111] J. Jeong, J. C. Gore, B. S. Peterson, Mutual information analysis of the eeg in patients with alzheimer's disease, Clinical Neurophysiology 112 (5) (2001) 827–835.

[112] J. Martinerie, A. M. Albano, A. Mees, P. Rapp, Mutual information, strange attractors, and the optimal estimation of dimension, Physical Review A 45 (10) (1992) 7058.

[113] A. J. Butte, I. S. Kohane, Mutual information relevance networks: functional genomic clustering using pairwise entropy measurements, in: Pac Symp Biocomput, Vol. 5, 2000, pp. 418–429.

[114] P. Qiu, A. J. Gentles, S. K. Plevritis, Fast calculation of pairwise mutual information for gene regulatory network reconstruction, Computer methods and programs in biomedicine 94 (2) (2009) 177–180.

[115] M. J. Whelan, K. D. Janoyan, In-service diagnostics of a highway bridge from a progressive damage case study, Journal of Bridge Engineering 15 (5) (2009) 597–607.

[116] S. Kim, S. Pakzad, D. Culler, J. Demmel, G. Fenves, S. Glaser, M. Turon, Health monitoring of civil infrastructures using wireless sensor networks, in: Information processing in sensor networks, 2007. IPSN 2007. 6th international symposium on, IEEE, 2007, pp. 254–263.

172

[117] T. Harms, S. Sedigh, F. Bastianini, Structural health monitoring of bridges using wireless sensor networks, Instrumentation & Measurement Magazine, IEEE 13 (6) (2010) 14–18.

[118] S. Gao, G. Ver Steeg, A. Galstyan, Efficient estimation of mutual information for strongly dependent variables, in: Artificial Intelligence and Statistics, 2015, pp. 277–286.

[119] T. Eltoft, T. Kim, T.-W. Lee, On the multivariate laplace distribution, Signal Processing Letters, IEEE 13 (5) (2006) 300–303.

[120] https://www.lakecountyfl.gov.

[121] https://www.conserve-energy-future.com.

[122] C. Strobbia, Surface wave methods: acquisition, processing and inversion, 2003.

[123] V. Shtivelman, Using surface waves for studying the shallow subsurface, Bollettino di Geofisica Teorica ed Applicata 44 (3-4) (2003) 223–236.

[124] R. G. Pratt, C. Shin, G. Hick, Gauss–newton and full newton methods in frequency–space seismic waveform inversion, Geophysical Journal International 133 (2) (1998) 341–362.

[125] R. G. Pratt, Seismic waveform inversion in the frequency domain, part 1: Theory and verification in a physical scale model, Geophysics 64 (3) (1999) 888–901.

[126] R. M. Shipp, S. C. Singh, Two-dimensional full wavefield inversion of wide-aperture marine seismic streamer data, Geophysical Journal International 151 (2) (2002) 325–344.

[127] C. Ravaut, S. Operto, L. Improta, J. Virieux, A. Herrero, P. Dell'Aversana, Multiscale imaging of complex structures from multifold wide-aperture seismic data by frequency-domain full-waveform tomography: Application to a thrust belt, Geophysical Journal International 159 (3) (2004) 1032–1056.

[128] S. Cheong, S. Pyun, C. Shin, Two efficient steepest-descent algorithms for source signature-free waveform inversion: Synthetic examples, Journal of Seismic Exploration 14 (4) (2006) 335.

[129] D.-H. Sheen, K. Tuncay, C.-E. Baag, P. J. Ortoleva, Time domain gauss—newton seismic waveform inversion in elastic media, Geophysical Journal International 167 (3) (2006) 1373–1384.

[130] C. Gélis, J. Virieux, G. Grandjean, Two-dimensional elastic full waveform inversion using born and rytov formulations in the frequency domain, Geophysical Journal International 168 (2) (2007) 605–633.

[131] A. Romdhane, G. Grandjean, R. Brossier, F. Réjiba, S. Operto, J. Virieux, Shallow-structure characterization by 2d elastic full-waveform inversion, Geophysics 76 (3) (2011) R81–R93.

[132] W. Hu, A. Abubakar, T. Habashy, J. Liu, Preconditioned non-linear conjugate gradient method for frequency domain full-waveform seismic inversion, Geophysical Prospecting 59 (3) (2011) 477–491.

[133] V. Akcelik, G. Biros, O. Ghattas, Parallel multiscale gauss-newton-krylov methods for inverse wave propagation, in: SC'02: Proceedings of the 2002 ACM/IEEE Conference on Supercomputing, IEEE, 2002, pp. 41–41.

[134] M. Li, A. Abubakar, J. Liu, G. Pan, T. M. Habashy, A compressed implicit jacobian scheme for 3d electromagnetic data inversion, Geophysics 76 (3) (2011) F173–F183.

[135] S. Alnabulsi, http://people.ucalgary.ca.

[136] Y. Sasaki, Two-dimensional joint inversion of magnetotelluric and dipole-dipole resistivity data, Geophysics 54 (2) (1989) 254–262.

[137] J. Hadamard, On problems with partial defaults and their physical meaning, Princeton university bulletin.

[138] V. Kostin, V. Lisitsa, G. Reshetova, V. Tcheverda, Local time–space mesh refinement for simulation of elastic wave propagation in multi-scale media, Journal of computational physics 281 (2015) 669–689.

[139] C. H. Reinsch, Smoothing by spline functions, Numerische mathematik 10 (3) (1967) 177–183.

[140] F. Press, Earthquake prediction, Scientific American 232 (5) (1975) 14–23.

[141] J. H. Whitcomb, J. D. Garmany, D. L. Anderson, Earthquake prediction: Variation of seismic velocities before the san francisco earthquake, Science 180 (4086) (1973) 632–635.

[142] D. Vere-Jones, Earthquake prediction-a statistician's view, Journal of Physics of the Earth 26 (2) (1978) 129–146.

[143] G. M. Molchan, Earthquake prediction as a decision-making problem, Pure and Applied Geophysics 149 (1) (1997) 233–247.

[144] P. M. DeVries, F. Viégas, M. Wattenberg, B. J. Meade, Deep learning of aftershock patterns following large earthquakes, Nature 560 (7720) (2018) 632.

[145] Y. Y. Kagan, L. Knopoff, Statistical short-term earthquake prediction, Science 236 (4808) (1987) 1563–1567.

[146] A. Kraskov, H. Stögbauer, P. Grassberger, Estimating mutual information, Physical review E 69 (6) (2004) 066138.

Appendix A

Basics from Probability Theory

In this section, we present the basic definitions from probability theory. These definitions are taken from *Information Theory* by Marcelo S. Alencar [81].

A.1   Probability

The probability of an event S is a number $P(S)$ assigned to the event. If the experiment is performed n times and the event S occurs n_0 times, then the probability of the event $P(S)$ is the relative frequency n_0/n of the occurrence of S:

$$P(S) = \frac{n_0}{n}, \quad \text{where} \ \ 0 \leq P(S) \leq 1.$$

If there are N distinct possible events $(x_1, x_2, ..., x_n)$ with the events occurring frequencies $(n_1, n_2, ..., n_N)$, then the probability of event x_i is given by

$$P(x_i) = \frac{n_i}{\sum_{j=1}^{N} n_j}.$$

This satisfies the property $\sum_{i=1}^{N} P(x_i) = 1$.

A.1.1 The Axioms of Probability

The basic axioms of probability were established by Andrei Nikolaevich Kolmogorov $(1903 - 1987)$, and allowed the development of the complete theory.

- $P(\Omega) = 1$, in which Ω denotes the sample space or universal set and $P(\cdot)$ denotes the associated probability;

- $P(A) \geq 0$, in which A denotes an event belonging to the sample space;

- $P(A \cup B) = P(A) + P(B)$, in which A and B are mutually exclusive events and A union B denotes the union of events A and B.

A.1.2 More Properties

- Notice that

$$\emptyset \cup \Omega = \Omega$$

- The sets $\emptyset$ and Ω are disjoint and thus,

$$P(\emptyset \cup \Omega) = P(\Omega) = P(\emptyset) + P(\Omega) = 1 \Rightarrow P(\Omega) = 0.$$

- In the case of sets A and B which are not disjoint,

$$P(A \cup B) = P(A) + P(B) - P(A \cap B).$$

A.1.3 Bayes' Rule

Bayes' rule, which is essential for the development of Information Theory, concerns the computation of conditional probabilities and can be expressed by the following definition,

$$P(A|B) = \frac{P(A \cap B)}{P(B)},$$

where $P(B) \neq 0$. Here A and B denote events from a given sample space.

- If A is independent of B, then $P(A|B) = P(A)$. It then follows that $P(B|A) = P(B)$ and that B is independent of A.

- If $B \subset A$, then $P(A|B) = 1$.

A.1.4 Random Variables

A random variable denoted by X, is a stochastic function that defined on the sample space. There are two types of random variables, discrete and continuous. A discrete random variable is one which takes only a finite or countably infinite number of values [75, 76].

For example, the number of dogs in a village, number of defective bulbs in a box belong to discrete random variables.

Definition A.1.1. *The discrete probability distribution is a list of probabilities associated with its discrete random variable X. If the possible values that X can takes are $x_1, x_2, ...,$ then the discrete probability distribution of X can be defined*

$$P(X = x_i) = p_i,$$

where p_i satisfies

1. $0 \leq p_i \leq 1$ for each i.

2. $\sum_i p_i = 1$.

A random variable that takes non-discrete values is called continuous random variables[75, 76].

Examples: a person's weight, time required to complete a task

Definition A.1.2. *The continuous distribution function can be expressed as*

$$F(x) = P\left(X \leq x\right) = \int_{-\infty}^{x} f(u)du,$$

where $f(x)$ satisfies

1. $f(x) \geq 0$

2. $\int_{-\infty}^{\infty} f(x)dx = 1$

Definition A.1.3. *The joint probability distribution of two discrete random variables can be denoted by*

$$P\left(X = x, Y = y\right) = f\left(x, y\right),$$

where

1. $f\left(x, y\right) \geq 0$

2. $\sum_{x} \sum_{y} f\left(x, y\right) dx = 1.$

The joint probability distribution of two continuous random variable can be obtained easily by analogy with the discrete case on replacing the sums by integrals[].

A random variable is usually characterized by a cumulative probability function (CPF) $P_X(x)$, or by a probability density function (pdf) $p_X(x)$.

Example: a random variable with a uniform pdf, in the interval $[0, 1]$, is described by the formula

$$P_X(x) = u(x) - u(x - 1).$$

It follows, by Axiom 1, that

$$\int_{-\infty}^{\infty} P_X(x) \ dx = 1$$

178

In general, for a given probability distribution, the probability that X belongs to the interval $(a, b]$ is given by

$$P(a < x \le b) = \int_a^b P_X(x) \; dx.$$

The cumulative probability function $P_X(x)$, of a random variable X , is defined as the integral of $p_X(x)$,

$$P_X(x) = \int_{-\infty}^x p_X(t)dt$$

.

Appendix B

'Listening' to signals traveling through bridges for diagnosing damage

ScienceDaily®

Your source for the latest research news

'Listening' to signals traveling through bridges for diagnosing damage

Date:	November 30, 2016
Source:	American Institute of Physics (AIP)
Summary:	A passive and noninvasive approach has been developed to "listen" to a collection of relevant signals from bridges and other mechanical structures to diagnose changes or damage.

FULL STORY

A group of Clarkson University mathematicians and a civil engineer developed a passive and noninvasive approach to "listen" to a collection of relevant signals from bridges and other mechanical structures to diagnose changes or damage.

As the group reports in Chaos, from AIP Publishing, their approach involves installing accelerometer sensors at various locations along a bridge to measure how each small part of the bridge is disturbed in response to a truck driving across.

"Signals from sensors near the truck loading are relevant, but so are signals far away because they react as the bridge structure flexes under its load and the entire structure oscillates like a guitar string, but obviously more complicated," said Erik M. Bollt, a W. Jon Harrington professor in the Department of Mathematics at Clarkson University, located in Potsdam, NY.

Accelerations serve as "a listening media to forces and accelerations travelling through the structure," Bollt said. "Signals travelling through the structure are expected to change if the bridge undergoes a change, such as a crack within the structure or if some of the bolts holding it together are loosened deliberately."

A central part of the group's analysis is a data processing technique called "optimal mutual information interaction," which was developed to identify significant direct interactions between individual components within a system.

"Our technique adopts ideas from information and communication theory and uses state-of-the-art statistical estimation routines," said Jie Sun, an assistant professor in the Department of Mathematics at Clarkson University. "The key concept is to search for interactions that are most relevant to the increase of predictability of bridge oscillations. If the bridge's structure has been altered due to damage or deformation, the details are expected to change, enabling us to detect the health status of the bridge."

The group's work stands out because it brings together two unique aspects to detect damage within bridges or other mechanical structures.

"One is the noninvasive and automated nature of the data collection process," Sun said. "The other is the data analytics tool we developed, which can infer direct information flow and significant interactions. By combining them, we're able to detect from only the data the presence of structural changes within the bridge as controlled and varied in our experiment."

Along the way, the three mathematicians involved found some interesting structural defects revealed by data analysis of significant interactions, which puzzled them for a long time because it just didn't make sense.

"Our analysis suggested a 'boundary' in the middle of the covered area where there is no apparent structural defect or pattern," Sun said. "After long discussions with our civil engineer collaborator, Kerop Janoyan, a professor of civil engineering at Clarkson University, we finally realized that we'd been confused all along because the covered area isn't the entire bridge in the experiment, but rather a one-third portion and the 'boundary' we discovered is precisely where there is a structural boundary some supporting structure underneath."

Bridges are ubiquitous, so it's important to be able to detect structural damage as early as possible to avoid disastrous outcomes. But detection of structural damage, which is often done manually, can be costly and in many cases isn't effective.

Since the group's work combines modern sensing technology with state-of-the-art data analytics tools to automate this process, "it can be used for early detection of structural changes and damage before requiring inspection by a human," Bollt said.

This approach can be used along with inexpensive instrumentation for all sorts of structures -- from bridges to wind turbines, buildings to airplanes.

"Accelerometers are becoming so cheap that we find them even within cellphones, so this will become a data avalanche, serving as a marriage of modern big data analytics with structural health monitoring," Bollt said.

The group is now working to make their approach deployable.

"On the more theoretical side, we're building a database of bridge models that can be easily simulated and tested via computers to calibrate parameters in the method, and we're also developing improved statistical estimators to produce more accurate results faster," Bollt said with Sun's agreement. "On the experimental side, we're collaborating with labs to test our methods for other structures, including airplane wings under various conditions."

Story Source:

Materials provided by **American Institute of Physics (AIP)**. Note: Content may be edited for style and length.

Journal Reference:

1. Amila Sudu Ambegedara, Jie Sun, Kerop Janoyan, Erik Bollt. **Information-theoretical noninvasive damage detection in bridge structures**. Chaos: An Interdisciplinary Journal of Nonlinear Science, 2016; 26 (11): 116312 DOI: 10.1063/1.4967920

Cite This Page:

MLA	APA	Chicago

American Institute of Physics (AIP). "'Listening' to signals traveling through bridges for diagnosing damage." ScienceDaily. ScienceDaily, 30 November 2016. <www.sciencedaily.com/releases/2016/11/161130090220.htm>.

RELATED STORIES

Sensing Trouble: New Way to Detect Hidden Damage in Bridges, Roads

Appendix C

An Information Theory Based Thermometer to Uncover Bridge Defects

Research | January 17, 2017

An Information Theory-Based 'Thermometer' to Uncover Bridge Defects

By Lakshmi Chandrasekaran

Aging roadway infrastructure generates the threat of sudden bridge collapses, along with the possibility of catastrophic human mortality rates. Unlike with a faulty mobile phone, one cannot simply pick apart a bridge, identify the defect, repair it, and put everything back together.

"When an inspector detects a sign of distress—say, cracking—it is not always straightforward to figure out the cause of the problem without an in-depth analysis," Pinar Okumus, assistant professor of civil, structural, and environmental engineering at the University of Buffalo, New York, said. "This makes it hard, and sometimes subjective, to evaluate the seriousness of the condition. So, the decision-making to mark a bridge safe or not after detection of a problem is one of the hardest parts of the job." Okumus was not associated with this study.

Is it then possible to perform preemptive, hands-free checks on the mechanical 'health' of bridges? The answer is yes, according to a study by an interdisciplinary team of applied mathematicians—Amila Sudu Ambegedara, Jie Sun, and Erik Bollt—and civil engineer Kerop Janoyan, all of Clarkson University. The work was published in *Chaos*.

How does math help prevent bridge-collapse disasters? The research team, led by Bollt and Sun, uses techniques from 'information theory,' a branch at the intersection of mathematics and electrical engineering that can help monitor the structural health of bridges.

In 1948, a mathematician and electrical engineer named Claude Shannon developed this seminal field to study how information can be quantified, stored, and transmitted through abstract "wires" in terms of bits 0 and 1, igniting modern telecommunication. Incidentally, we celebrated Shannon's 100th birthday in 2016.

Information theory, is currently comprised of a combination of physics, mathematics, computer science, and engineering methods. This field has spawned the rise of the internet and the World Wide Web, cell phones, cryptography, and many cutting-edge applications.

However, information needs a medium for transmission. Imagine a communication channel via fiber optic cables – one of the fastest media. A nick or tear in the cable would impair communication, as it would be noisy and travel slower. Similarly, a mechanical or structural defect in the bridge would affect mechanical waves travelling through it.

184

"I have always been fascinated with the concept that the way a given disturbance, an acceleration, a distortion travels through media is clear, but the details of how tightly built that structure is will moderate the details of how the signal travels through the structure," Bollt said, explaining his motivation for this research. "So a good way of 'listening'" to the structure could do the job. This work is essentially about an information-theoretic way of listening to the signals travelling through the structure."

The scientists primarily used various forms of "Shannon entropy" to detect and analyze damages in bridges. "The entropy of a system measures how 'disordered' or 'unpredictable' the system is," Sun explained. "This quantity can be extended to study the flow of information among subcomponents of a complex system, and that is exactly what we did in this study; we used what we called 'causation entropy' and optimal mutual information interaction (oMII) to detect structural patterns and damages in bridges."

One attractive aspect of this method is its purely noninvasive nature; this is in contrast to conventional manual inspection, which is invasive and can be cost-prohibitive. Additionally, it may not be possible to detect problems with bridges by visual inspection alone. "For example, corrosion of steel bars on concrete cannot be detected by visual inspection. Special instrumentation might be required, but these instruments have varying levels of reliability," Okumus said.

In order to conduct their experiments, Janoyan led an engineering squad to place thirty accelerometers (wireless sensors) at various locations on the Waddington Bridge in Waddington, NY, which measured how each small part of the bridge was disturbed as a truck passed through. The team compared these results with the bridge's response under "damaged" conditions by removing a few bolts, thereby artificially inducing damage and collecting time series sensor data from various locations. They found that the sensor signals obtained from different sites were more likely to be coincidental under "healthy" conditions than damaged ones.
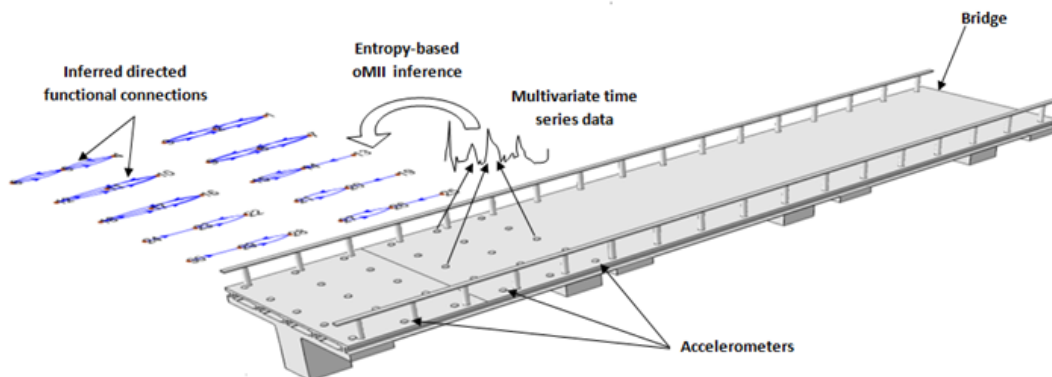

This figure shows a top view of the Waddington Bridge in NY. The research team placed a total of 30 dual-axis accelerometers (wireless sensors) near one end of the bridge, uniformly covering roughly one-third of the surface area.

185

They collected the accelerations measured at each accelerometer as a multivariate time series dataset and recorded them into a digital computer. Using the recorded data, the team then inferred directed functional influences as connections between the accelerometer sites using an entropy-based optimal mutual information interaction (oMII) algorithm. Figure credit: Amila Sudu Ambegedara, Jie Sun and Erik Bollt.

Ambegedara applied oMII, an entropy-based optimization algorithm developed by Sun and Bollt, which compared the structural monitoring of the bridge's health to the measurement of our body temperature, which detects abnormalities in our health. "I have always been amazed by how much information a tiny bit of change in body temperature can tell us about our health," Sun said. "Thus, I always liked the idea of having a simple thermometer-like device to monitor the internal status of very complex systems."

Bollt noted that the work merges two unique aspects to use real-time data when detecting the presence of structural change in the bridge. "One is the noninvasive and automated nature of the data collection process, which has become popular in structural health monitoring but is not yet common," he said. "The other is the specifics of the unique data analytics tool that we developed, which is able to infer direct information flow and significant interactions."

"On the analytical/computational side, we apply an entropy-optimization algorithm—which we recently developed—to the measured data to detect effective interactions among the sensor locations," Sun said, describing the use of techniques normally used in deciphering big data. "Without such 'big data analytics,' we will be left with just large volumes of data and no clue of what's actually going on with the bridge."
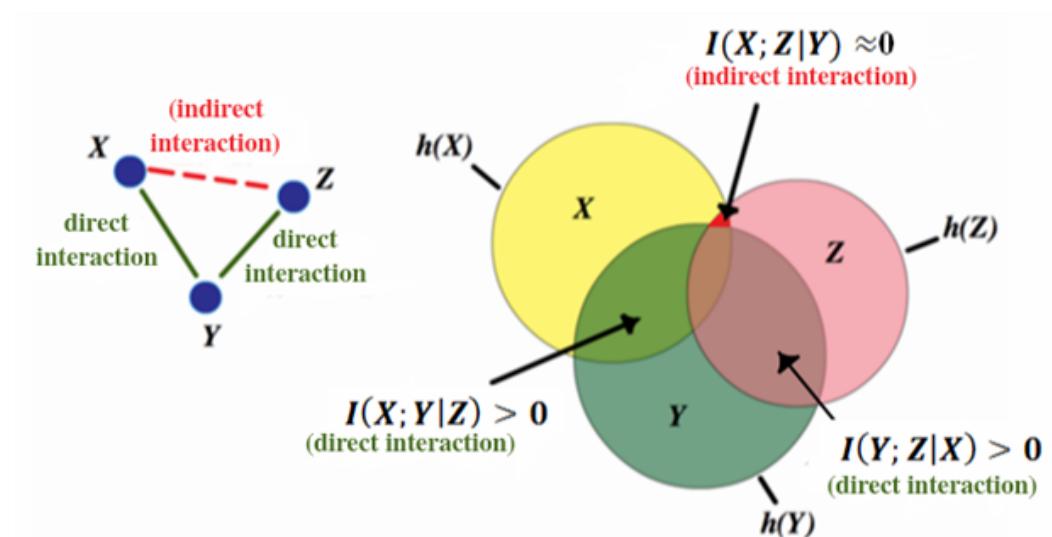
X, Y, and Z are three random variables whose interdependences are represented by a three-node directed network. Solid edges indicate direct dependence, whereas the dashed edge represents indirect dependence. The Venn diagram shows direct and indirect mutual information interactions of these variables. Direct interactions (dark green area) have significant mutual information, between X and Y, given Z, and between Y and Z, given X, for example; on

186

the other hand, proper conditioning enables one to "filter out" indirect interactions (small red area), which are those interactions characterized by having mutual information that disappears upon conditioning, between X and Z, given Y, for example. Figure credit: Amila Sudu Ambegedara, Jie Sun and Erik Bollt.

A key component of the analysis was the data processing technique oMII that can identify significant direct interactions between individual sensors in the system. According to Bollt and Sun, oMII is an excellent technique based on ideas from information and communication theory. It uses state-of-the-art statistical estimation routines. "The key idea is to search for interactions that are most relevant to the increase of predictability (reduction of uncertainty) of the bridge oscillations," Sun said. "If the bridge's structure has been altered either due to damage or deformation, the details of the sensor interaction network are expected to change, enabling one to detect the health status of the bridge," Bollt added. And such changes in interaction between sensors were indeed observed when the researchers removed key bolts and induced artificial "damages" to the Waddington Bridge.

In the future, the team would like to expand the current study to assess the health of more bridges and other mechanical structures. "Ultimately, we would like to integrate our data analytics tool with automated data collection to develop something that detects the health status of a bridge as simply as a thermometer detects body temperature," the team said.

Lakshmi Chandrasekaran received her Ph.D. in mathematical sciences at the New Jersey Institute of Technology. She is currently pursuing her masters in journalism with a health & science writing concentration at Northwestern's Medill School of Journalism. She is a freelance science writer whose work has appeared in *PLUS* math magazine, *HELIX - Science in Society* magazine at Northwestern University, and *The Munich Eye*, an online newspaper based in Munich, Germany.